Gold nanodot and nanowire fabrication by Atomic Force Microscopy

Manuel E. Pumarol-Crestar
Centre for the Physics of Materials
Department of Physics, McGill University
Montréal, CANADA
July 2008

A Thesis submitted to the
Faculty of Graduate Studies and Research
in partial fulfillment of the requirements for the degree of
Doctor of Philosophy

a posse ad esse

Contents

Statemnet of Originality **xvii**

Acknowledgments **xviii**

1 Introduction **1**
- 1.1 Nanofabrication with scanning probe methods . . . 3
- 1.2 Outline . . . 6

2 Background **9**
- 2.1 Review of Dynamic Force Microscopy . . . 9
  - 2.1.1 Forces, Sensors, and Probes . . . 9
  - 2.1.2 Operation modes, Instrumental aspects . . . 14
  - 2.1.3 Dynamics of a vibrating tip . . . 17
  - 2.1.4 Resolution . . . 22
- 2.2 Deposition Mechanism . . . 24
  - 2.2.1 Introduction . . . 24
  - 2.2.2 Field Evaporation Deposition . . . 25
  - 2.2.3 Point Contact . . . 30

3 Nanodots fabrication: setup & methods **32**
- 3.1 Tip-sample separation control . . . 32
  - 3.1.1 Introduction of an electrostatic force term . . . 32
  - 3.1.2 Tip shape & Capacitance . . . 35
  - 3.1.3 Construction of d vs. V_{bias} curves . . . 41
- 3.2 Instrumentation . . . 43
  - 3.2.1 The microscope . . . 43
  - 3.2.2 Cantilever tip preparation . . . 45
  - 3.2.3 Applied pulse and tip lifting bias . . . 47
  - 3.2.4 Data acquisition . . . 48
- 3.3 Deposition procedure . . . 49

4 From dots to wires **55**
- 4.1 Monitoring of the tip's oscillation amplitude . . . 55
- 4.2 Dot dimensions characterization . . . 56
  - 4.2.1 Size dependence on the pulse duration Δt . . . 58
  - 4.2.2 Size dependence on the pulse amplitude ΔV . . . 60
- 4.3 Deposition mechanism . . . 62
  - 4.3.1 There is a threshold . . . 62
  - 4.3.2 The rate equation . . . 64
  - 4.3.3 The tip polarity . . . 68

4.4 Tip shape & electric field 70
4.5 Connected lines & lithography 73

5 ELECTRICAL CHARACTERIZATION 76
5.1 Introduction: Electrical properties of small wires 76
5.1.1 Conduction properties 76
5.1.2 Failure mechanisms 81
5.2 Experimental setup & methods 83
5.2.1 Micro-electrodes fabrication procedure & sample preparation . 83
5.2.2 Measurement setup 88
5.2.3 Device fabrication & characterization 90
5.2.4 Overcoming edge problems 93
5.3 Model for the failure mechanism of μ-electrodes leads 97

6 CONCLUSIONS & OUTLOOK 104

Bibliography 108

List of Figures

1.1 Schematic of a Single Electron Tunneling device. In order for the device to work, the nanostructure must be coupled capacitively to all the electrodes and 'tunnel coupled' to the source and drain. 2

1.2 InAs SAQD patterned on a InP substrate [19]. 3

1.3 Relevant length scales [27]. 4

2.1 Relevant distances for the tip-sample geometry. d is the instantaneous tip-sample separation, D is average tip-sample separation, and z is the instantaneous tip position. Adapted from ref. [48]. 10

2.2 Microfabricated cantilever chip. a) Schematic: top and side view, usual dimensions for the cantilever ranges are: 25 to 50 μm, 1 to 3 μm, and 100 to 300 μm for w, t, and L respectively. The tip height h ranges from 5 to 20 μm. b) SEM scan of a NanoSensor PointProbe: a usually terminated 10 nm radius Si tip. Adapted from ref. [49]. 12

2.3 SEM images of high end silicon cantilever tips: a) Supersharp with a less than 10nm radius, and b) Very high aspect sharp tip. Images courtesy of NanoSensors GmbH. 13

2.4 Modes of operation in force microscopy. Adapted from ref. [50] . . . 14

2.5 Instrumentation diagram for AM-AFM. Adapted from ref. [50]. . . . 16

2.6 Experimental (dotted plots) and theoretical (solid line plots) resonance curves of amplitude (in black) and phase shift (in red). Experimental curves where obtained by sweeping the driving frequency and with the tip far from the surface. Theoretical values are calculated using equations 2.7 and 2.8, the natural frequency for this particular cantilever is $f_0 = 160\ kHz$, the quality factor is 470, and $\gamma \approx= 2140\ s^{-1}$. 19

2.7 Simplified atomic potential digram for the tip-sample system. (a) When the separation distance d is comparatively large, the tip-atom U_{at} and the sample-atom U_{as} interaction potential do not overlap. Λ_t and Λ_s are the binding energy to remove an atom from the surface of the tip or the sample, respectively. (b) When d is shortened the total potential energy curve U_a shows a potential barrier of height Q_0. This barrier is considerably smaller than Λ_t and Λ_s. 25

2.8 Simplified atomic potential digram for the tip-sample system with applied field E_a. (a) Ionic and atomic potential energy curves with applied field E_a. The activation energy Q_n is significantly smaller than Q_0 in Fig. 2.7(b). (b) When an insulator of permittivity ϵ and thickness t is in the junction the activation enrgy Q_n^{ins} is increased. 27

2.9 Field evaporation deposition. (a), (b) Positive field. In this case the field gradient is not as intense on the tip apex. Electrons from the sample will hit a large area close to the tip apex. Field evaporation for the cation Au^+ will happen when the threshold field is reached, field close to 23.8 V/nm. (c), (d) Negative field. Field gradient lines are very dense at the tip apex. Hydrodynamic flows of atoms and intense heating of the tip creates a protrusion at the apex, when the field exceeds 11 V/nm field evaporation of Au^{2-} will happen. The distance between tip and sample is reduced by the creation of this protrusion. 29

2.10 Point Contact. (a) Tip on very close proximity to the sample (4 to 6 Å). (b) When a high electric field is applied, atoms migrate by field enhanced diffusion to the tip apex and a point contact is formed. (c) Tip withdraw by feedback control. (d) Mound of deposited material left on surface. 30

3.1 Experimental force-distance curves: Reduced oscillation amplitude a vs. tip-sample distance. a) Intermittent contact operation mode, b) For $V_{bias} \approx 6\ V$ and higher biases, the tip is in a non-contact mode regime. The curves in black are taken while the tip is approaching the sample, and in the red curves the tip is being retracted by the Z-piezo. Experimental parameters are: the amplitude setpoint is $a = 0.95$, the free oscillation amplitude is $A_0 = 6\ nm$, and the reduced frequency is $u = 0.9988$. These values correspond to typical experimental conditions. The hysteresis in a) are owed to non-linearities of the force-distance equations. 34

3.2 Calculated second derivative of the capacitance vs. tip-sample separation. The tip radius is 80 nm, the average tip-sample separation is 10 nm, and $S_{eff} = 2513\ nm^2$. Cantilever dimensions: $w = 38\ \mu m$, $L = 225\ \mu m$, and $h = 20\ \mu m$. 37

3.3 Relevant dimensional scales and the tip configuration geometry model. The sample surface is always modeled as a one plane plate. Adapted from ref. [51]. 38

3.4 Calculated force-distance curves of the reduced amplitude a against the reduced tip-sample separation d with electrostatic coupling. The parameters used are: reduced frequency $u = 0.9988$, free amplitude $A_0 = 6\ nm$, $Q = 850$, $k = 40\ n/m$, $S_{eff} = 2513\ nm^2$, $k_{elec} = (1.287 \times 10^{-3}/V^2)V_{bias}^2$, and $k_{vdW} = 3.086 \times 10^{-4}$. These parameters correspond to typical experimental conditions. The horizontal dashed line corresponds to the experimental amplitude setpoint $a = 0.95$. . . 40

3.5 Theoretical plot of the lift height D vs. the applied bias V_{bias}. Amplitude setpoint is $a = 0.95$. 41

3.6 Lift vs. applied bias by keeping the interaction (force gradient) constant for three different models for the geometry of the tip-sample system. (a) For a sphere-plane: $D|_{F'=const} = \left(\frac{\pi\epsilon_0 R}{F'}\right)^{\frac{1}{2}} V_{bias}$, the shape is linear, (b) For a plane surface or disk: $D|_{F'=const} = \left(\frac{\pi\epsilon_0 R^2}{F'}\right)^{\frac{1}{3}} V_{bias}^{2/3}$, same shape as in Fig. 3.5, and (c) For a cone: $D|_{F'=const} = \left(\frac{\pi\epsilon_0 K^2}{F'}\right) V_{bias}^2$, the shape is parabolic. Adapted from Ref. [71]. 42
3.7 Schematic of the experimental setup. 44
3.8 FE-SEM images of silicon cantilever tips with a 100 nm/10 nm Au/Ti evaporated coating: a), b) MikroMasch cantilever-tips, two different view angles of the same tip, a) 22∘ side view, b) top view. c), d) NanoSensors cantilever-tips, two different tips coated in the same batch, both images 22∘ side view. In all images the cantilever is on the right of each tip. 46
3.9 Tip polarity. V_{bias} and V_{pulse} are always applied to the tip and sample respectively. 48
3.10 LabVIEW application interface for data acquisition. 49
3.11 Gold Deposition using an AFM. a) Imaging the area of interest. b) V_{bias} is applied, tip-sample average separation increased to d. A non contact image is taken. c) Deposition script is running: tip translated to position of interest, V_{pulse} is applied. d) Imaging the same area after deposition, four pulses applied on C), four nanodots deposited. . . . 50
3.12 Experimental lift height vs. applied bias. Only after $V_{bias} \approx 8\ V$ the tip is in the non-contact regime. The experimental parameters are: $Ao = 7.5\ nm$, $u = 1.000$, and $a = 0.95$. 51
3.13 FE-SEM micrographs of heavily damaged tips after an accidental contact. a) Mechanical deformation contact. b) Contact while applying V_{pulse}. Inset: AFM scans of the resulting structures on the surface. . 54

4.1 Time resolved tip's oscillation amplitude, average deflection and applied pulse in a single deposition event. 56
4.2 AFM images of a sequence of dots forming lines with corresponding section profiles of selected lines. (a) lines 1, 2, 3 are 20 dots deposited with fixed $\Delta V = 30\ V$, and with $\Delta t = 1\ ms$, 5 ms, and 10 ms respectively. (b) 27 dots lines deposited by keeping constant Δt at 10 ms, and $\Delta V = 32\ V$, 35 V, and 41 V, respectively. (c) 16 dots lines deposited with fixed $\Delta t = 1\ ms$, and $\Delta V = -26\ V$, $-27\ V$, and $-28\ V$. In (a), (b) with intermittent feedback, and in (c) the feedback is always engaged. Notice that the height scale is 16 nm on (b) 1, 2, and 3. For all the profiles the surface distance scale is 100 nm between major ticks of the horizontal axis which corresponds with the scale of 2D images. For all deposited lines $d = 6\ nm$, and $2A = 6\ nm$. 59
4.3 Time resolved feedback circuit response to the application of a pulse. Negative Z values corresponds to retraction of the sample. 60

4.4 Modification of the dot width and height by (a) changing Δt, with $\Delta V = 30\ V$ or (b),(c) changing ΔV with $\Delta t = 10\ ms$ in (b), and $\Delta t = 1\ ms$ in (c). (d) Calculated aspect ratio of the data in (b). Feedback loop in (a),(b) intermittent implementation, in (c) always enabled. Each datum correspond to 20 deposition trials in (a), 27 trials in (b), and 16 trials in (c). The width is measured at the FWHM. Lines are best fit to the data. 61

4.5 Probability of deposition while ramping the V_{pulse}, with a single pulse applied each time, and with fix d. (a) When a tip is first biased usually a big blob is deposited. Thereafter, the deposition threshold field is lowered. (b) Probability of deposition versus applied electric field for four different tips, after a sequence like in (a). Tip 2 & Tip 3 the polarity is positive, and in Tip 1 & Tip 4 the polarity is negative. All tips were Au-coated in the same evaporation batch. In both graphs each datum corresponds to 16 trials, and lines are a guide to the eye. 63

4.6 Graphs of the transfer rate vs. applied field for the ions Au^{2-} and Au^{+}. (a)Theoretical graphs calculated using equations 4.2 and 4.3. The blue lines correspond to $T = 300\ K$ and $d = 3\ nm$, in the red lines the temperature is changed to 700 K, and in the dotted lines the distance is changed to 1 nm. (b)Experimental graph for the cation Au^{2-}. (c)Experimental graph for the anion Au^{+}, the slope is smaller than in b). The experimental settings are those of the blue lines in a). The lines in b), and c) are a best fit to the data. 66

4.7 Transfer rate vs. inverted pulse length. We expected a horizontal line since the applied field is constant. Line is best fit to the data. 68

4.8 Dots deposition with identical parameters for positive and negative polarity applied to the tip. The pulse duration is fixed, $\Delta t = 2\ ms$. The maximum height for the $+25\ V$ line is 1.6 nm, or the $-25\ V$ is about 10 nm. 69

4.9 FE-SEM images of a selected tip. (a) The tip before deposition. (b) The same tip as in (a) after depositing the line shown in the inset. The tip have developed a sharp protrusion. The image in the inset is an AFM scan. 71

4.10 Geometric factor k_t vs. d/R for a hyperbolic tip, without a protrusion (solid line), and for hemispherical protrusions on the tip apex with ratios $R_b/R = 0.05$, and $R_b/R = 0.1$ (dotted lines). For all graphs the aperture angle $\theta = 10^{\circ}$ The inset shows the field enhancement E_b/E_t for each protrusion. 73

4.11 AFM images of direct lithographic patterning of Au lines. (a) 5×5 lines grid, each line have a width of 64 nm (about three grains) and a height of 2.5 nm. (b) Magnified image of the region of the black square shown in (a), suspected fracture zones are marked by circles. Several SEM spots are evident in (a). 74

4.12 First and last stages of a deposit over experiment. (a) First a 750 nm line, formed by 20 dots of approximate width of 22 nm FWHM, was deposited from left to right. It can be appreciated in the section profile the gaps between consecutive dots. (b) After two interdigitated depositions, with the same conditions for deposition as in (a), the line has double its height and no gaps are present. Settings for the deposition: $\Delta V = 30$ V, $\Delta t = 10$ ms, and the tip is positive polarized. 75

4.13 (a) Using the tip as a dot matrix printer, $1\mu m \times 1\mu m$ letters forming the word macgill. Initially an error was found on the letter g and then the deposition was repeated with the correct script. (b) 5 squares deposited in the same sequence from the inner to outer one. The imperfection seen at the right side of the square is due to hysteresis of the piezo scanner. Imperfect spell checking is also evident. 75

5.1 Schematic longitudinal section of the microstructure of fabricated wires. (a) Polygranular wire deposited using the 'fast mode'. Cross section area 3×64 nm^2, about 3 grains wide. (b) Bamboo-like wire deposited using the 'slow mode' and several overlapping depositions. Cross section area 10×22 nm^2, about one grain wide. Atomic diffusion modes: intergranular (blue arrow), along grain boundaries (green arrow), and transgranular (red arrow). 77

5.2 (a)Experimental resistivity for wires with different microstructures. The width of the grains are 60 nm, and 20 nm for the bamboo-like , and the polycrystalline wire respectively. (b) Modification of the MS theory by considering a log-normal distribution for the grain size. Adapted from [81]. 79

5.3 (a) Failure current density for gold nanowires. (b) Failure temperature for an electrically stressed nanowire. The nanowire fail at about 500 K. Adapted from [9]. 82

5.4 FE-SEM scans at different magnifications of patterned Au μ-electrodes with design II. In (a) both optical (bright features) and e-beam lithographic (dark features) steps are noticeable. (c) Device fabrication area. 84

5.5 (a), (b) Optical images of a patterned InP substrate mounted on a chip carrier with 12 pin connectors. (c) An AFM scan of the center of the pattern. The μ-electrodes terminal leads are 100 nm wide, 3500 nm long, and 25 nm tall. The circle inscribed by the μ-electrodes has a diameter of 2 μm. 85

5.6 (a) Measurement circuit for I-V characterization. (b) Typical I-V curves between contiguous μ-electrodes. Flat regions of the I-V curves are an instrumental saturation effect due to limited current output by the source-meter. 89

5.7 Bridging μ-electrodes 12 & 1, and I-V characterization. (a), (b) 3D representation of AFM scans. The insets are the corresponding surface images (a) A dotted line is deposited from μ-electrode 12. (b) After several depositions the line appears to be continuous and bridging the gap. A second not connected line is deposited at the terminals end. (c), (d) I-V curves before and after the nanowire bridge the μ-electrodes. The 20nm InP/10nm InGaAs /InP sample is used. 92

5.8 3D rendering of AFM scans of tip & μ-electrodes interactions. (a) Destruction of μ-electrode 1 by accidental contact with the pulsed tip. (b), (c) Moving the tip with positive polarity on the proximity of the edges of two μ-electrodes. (b) Before (no bias has been applied to the tip), (c) After, mass movement along the edge of the μ-electrodes. . 93

5.9 (a) Schematic diagram of the setup for the differential contrast enhancement technique. (b) Corresponding equivalent circuit diagram. R_1 and R_2 are the contact resistance at the μ-electrode and 2DEG, respectively. R_3 is the resistance of the buffer layer. 94

5.10 Rising and hiding a μ-electrode. (a)-(e) Section profiles while biasing the μ-electrode and the backelectrode. The μ-electrode is raised up to 43 nm at b), and hidden up to 12 nm at e). The topographical scan is shown at c). The arrow in a) shows the location at where all the section profiles were taken. Insets are the corresponding AFM scan. 96

5.11 FE-SEM scans of μ-electrodes patterns with design I at different magnification scales. (a) Photolithographic and e-beam lithography steps (b) The section at which μ-electrodes width change from 500 nm to 100 nm is marked with a circle. All 12 μ-electrodes have these sections. (c) Device fabrication area. The terminal leads are 100 nm wide. The very end of each μ-electrode has a shallow angle, for facilitating FE deposition. This design allows the possibility of four probe measurements. 97

5.12 (a) AFM image of an ESD blown wire. (b) Section profiles of the contact and μ-electrode interface on (a). 1- Far from the transversal interface the dimensions are as usual. 2- Just before the interface the height has increased considerably. 3- Severe damage of the interface. 4- Catastrophic failure of the μ-electrode, there is a 20nm deep trench. 98

5.13 Schematic of a one terminal electrode geometry. (a) Top view, (b) Boundary conditions used on the model. 100

5.14 Modeled temperature profile and distribution for $V_a = 1\ V$. (a) At the interface between the metallic electrode and the semiconductor. (b) At the interface between the semiconductor and the backelectrode. The color bars at the right of the graph are the temperature in K. The profiles are taken at the interface indicated by the white arrows. . . 101

5.15 Calculated temperature dependence on applied bias at the contact-wire interface. The black line: temperature at the metal and semiconductor interface. Red line: temperature at the interface between semiconductor and the backelectrode. The voltage is applied to the μ-electrode and the backelectrode is grounded. 102
5.16 AFM images of a controlled destruction of a μ-electrode. (a) Initial scan. The wire already have bee damaged by ESD, is thinner and taller than a regular one. (b) The wire has been considerably thinned and seems broken close to the contacting electrode. The semiconductor surface is very damaged. 103

6.1 Deposition of a nanowire over a InAs quantum dot. 107

List of Tables

3.1 Cantilever tip specifications 45

4.1 Average FMHW width and average height for hundreds of dots fabricated with identical conditions, and with the same tip in four different deposition trials. $\Delta t = 1\ ms$, $\Delta V = 30\ V$. 57
4.2 Rate of change of the transfer rate $\times 10^6\ atoms/s$ per $1\ V/nm$ 67

5.1 Transport regimes vs. Size 78
5.2 Calculated transport & failure properties of fabricated wires 83
5.3 Calculated transport & failure properties of μ-electrodes terminal leads 88
5.4 Thermal and electrical properties of relevant semiconductors & insulators 99

Abstract

In this dissertation work a technique that utilizes an atomic force microscope (AFM) in a non-contact configuration for direct patterning of nanoscale sized gold dots and wires and its characterizations is presented. For the fabrication of gold nanodots an oscillating gold-coated AFM probe is kept in close proximity to a sample surface and the application of a voltage pulse of either polarity leads to the deposition of the dot. Highly reproducible deposition is obtained by the precise control of the tip-sample separation. For controlling this separation, a feedback control enabled by the application of an external electrostatic servo force is implemented. The deposition process is well regulated and it allows for the study of dot formation and the obtaining of relevant statistics. Typical oscillation amplitude is 3 nm and tip sample average separation distance is 6 nm. Generated electric fields at the tip apex are usually larger than 1 V/nm. The parameters that control the dot dimensions are the amplitude and duration of the pulse, and the tip-sample separation. We found that the deposition process is Field Evaporation Deposition (FED) of gold ions. There is a field threshold that is distinctive of the involved ion species. Typical deposition evaporation rates are of the order of 10^7 $atoms/s$ and they are obtained for applied fields above the threshold for deposition. For patterning gold nanowires two methods were developed. A fast method where sequential dots are deposited with a pitch that is smaller than their diameter so that neighboring dots overlap, and a slow method in which the dots are deposited sequentially with a pitch that match their diameter and then the gaps between neighboring dots are filled with an interdigitated sequential deposition. Nanowires have an aspect ratio of about 10% and 40%, respectively. In situ electronic transport characterization measurements of a high aspect ratio nanowire revealed an electrical resistivity of 803 Ω-nm and a current density up to 0.74 $\mu A/nm^2$. A single setup is used for the patterning and the characterization measurements and is implemented at room temperature, and in ambient conditions.

Résumé

Cette recherche doctorale porte sur le dévelopment d'une technique utilisant un Microscope à Force Atomique (en anglais 'Atomic Force Microscope', AFM) dans une configuration dynamique pour la gravure direct de points et câbles d'or à l'échelle nanoscopique. Pour la fabrication de ces nanopoints, une sonde oscillatoire d'AFM métallisée d'or est maintenue à proximité d'une surface échantillon, et l'application de pulsations électriques de polarité positive ou négative conduit au dépôt du nanopoint. Un dépôt hautement prévisible est obtenu par le contrôle précis de la distance sonde-surface. Le contrôle de cette séparation est possible grâce á un mécanisme régulatoire ré-entrant activé par l'application d'une servoforce électrostatique externe. L'amplitude typique des oscillations est de 3 nm et la distance sonde-surface moyenne est de 6 nm. Les champs potentiels électriques générés à l'extrémité de la pointe dépassent habituellent 1 V/nm. Les paramètres contrôlant la dimension des nanopoints sont determins par l'amplitude et la durée de la pulsation ainsi que la distance sonde-surface. Le procédé de dépôt est bien contrôlé, ce qui permet l'étude de la formation du nanopoint et l'obtention de statistiques appropriées. Les résultats démontrent que le procédé de dépôt correspond à un Dépôt pour l'Evaporation de Champs (en anglais 'Field Evaporation Deposition', FED) d'ions d'or. Ce champs a un seuil distinct de celui des espèces ioniques impliquées. Les taux d'évaporation typiques du dépôt sont de l'ordre de 10^7 $atomes/s$ et ils sont obtenus par l'application de champs dépassant le seuil de dépôt. Deux méthodes ont été développées pour la gravure direct de nanocâbles d'or: (i) une méthode rapide impliquant le dépôt séquentiel de nanopoints à fréquence plus basses que leurs diamètres de façon à ce qu'il n'y ait pas d'empiètement avec les nanopoints voisins; et (ii) une méthode lente dans laquelle les nanopoints sont déposés séquentiellement avec une fréquence correspondant à leurs diamétres, puis les espaces entre les points voisins sont remplis par des dépots squentiels intimement liés . Les nanocâbles ont un rapport largeur/hauteur d'a peu pres 10% à 40%. Les mesures de caractérisation du transport électronique *in situ* d'un nanocâble à haut rapport largeur/hauteur révélent une résistivité électrique de 803 Ω-nm et une densité de courant atteignant jusqu'a 0.74 $\mu A/nm^2$. Un seul 'setup' est utilisé pour la fabrication des nanostructures et pour les mesures de caractérisation qui sont appliqué à température et conditions ambiantes.

Statement of Originality

The author claims the following aspects of the thesis constitute original scholarship and an advancement of knowledge. As yet, only one of these findings has been published.

- Deposition of gold nanodots by atomic force microscopy with precise control of the tip-sample separation distance using feedback control enabled by an electrostatical servo force. Allows for better understanding of the deposition mechanism for the fabrication of the dots. [M. E. Pumarol, Y. Miyahara, R. Gagnon, and P. Grütter, *Nanotechnology*, **16**, 1083 (2005)]

- Understanding of the behavior of the pulse duration Δt in the deposition process and its interaction with the feedback control which lead to the intermittent on/off implementation of the feedback. As a consequence the aspect ratio of deposited dots improved from about 10% to aproximatily 40% using the same deposition parameters.

- Developed a differential contrast enhancement technique for electrostatically screening electrode leads.

Acknowledgments

It has been a few years since I first embarked on this work, and an accurate account of all of those who have collaborated on this project is close to impossible. I hope I will be forgiven for leaving anyone out.

But first, always present with his guidance that made this work possible was Professor Peter Grütter. I feel extremely privileged to work with Peter, and moreover in a large research group which allowed me to be in contact with many different and interesting projects. I appreciate very much the opportunity Peter gives his students to go to international conferences as it really puts your work in context and broadens your ideas. I benefited greatly from my attendance at conferences in the USA and Japan. Above all I appreciate Peter for his guidance, both academically and personally. Peter constantly contributed an influx of ideas to the project, and I value his great organization of the lab in group and sub group meetings. I appreciate the invitations to enjoyable summer BBQs at Grütter's chalet and delicious Christmas raclette and fondue courtesy of his wife Rhea.

I would like to acknowledge the very special relationship with Dr. Yoichi Miyahara who on a daily basis had recommendations for improving the experiments. I really found our brainstorming sessions useful, and they were almost always after 6pm. Yoichi's technical expertise was definitely an asset to this project, and I am very grateful for his assistance.

I greatly appreciate the collaboration with colleagues at the Institute for Microstructural Sciences at the National Research Council in Ottawa, specifically Dr. Sergei Studenikin, Dr. Alicia Kam, Dr. Philip Poole, and Dr. Jean LaPointe for the fabrication of the semiconductor heterostructure that were used as samples for this work, and for fabrication of the microelectrode leads.

My great appreciation to our collaborators Dr. Eduardo Lugo and Prof. David Plant at the Department of Electrical and Computer Engineering for their support in the FEMLAB simulations project. Especially to Jean-Philippe Thiboeau for his invaluable help with the wire bonding machine.

I thank Prof. Michael Hilke for introducing me to the art of small wire soldering and for making me realize the importance of having hands that do not shake.

My gratitude is extended to all the Grütter-ites, Mike, Yan, Vincent, Alex, Roman, Henrik, Medhi, Till, Linda, Sean, the other ones at the Wong Building, Ben, Nela, Sarah (thank you for cleaving so many cantilevers!), Jeff, Shawn, Patricia, and Dr. Helen Bourke. It was an honor to share with you all this time, and I appreciated and enjoyed our exchange of ideas over the years. I am grateful to share the batcave with Jeff who always provided moments of unexpected entertainment (clumsiness is not a sin!).

To the three visiting students that collaborated on this project Philippe Dupuis, Eric Kramer , and Geche Nahrwold, who took some nice photos and collected some data that appears in this work. Thank you for your energy and interest in the well-being and advancement of this project. Philippe really got into the soldering and Eric's hands were too shaky to do it.

I would like to acknowledge Robert Gagnon for always making himself available, and for his help with FE-SEM measurements of cantilever tips. I appreciate very much all the useful tips about bike paths around the city.

I would like to acknowledge Professor Bruce Lennox from Chemistry for his sound advice and good discussions. Thanks also to his student Vicky.

I am thankful for the technical support and availability of Steve Godbout, Michelle Beauchamp, and Saverio Biunno. Michelle, I hope you got your power supply back! Thank you to Steve and Eddie for their vital help at the machine shop facilities of the department. Thanks Steve for amazing BBQs and stays at your farm. It was a really enjoyable time and it was great to go fishing for the first time.

I appreciate the aid of Paula, Diane, Sonia, Louise, and Elizabeth who were stellar navigators of the bureaucratic network of McGill apparatus. Thank you very much for being so friendly and for organizing wonderful Christmas parties and marvelous summer BBQs.

I would like to personally recognize the efforts of my friends Henrik, Darren, David, and Nela for the warm friendship they offered me in these hard years and their continuous encouragement. I especially want to thank my officemate Darren for all the shared times and for his judicious 'spotting' at the gym and continuous interest in my work. My pals David and Nela were always there, and I enjoyed our amazing hang-outs on different occasions. Nela, I will be always indebted, thanks for submitting my thesis! Thanks to Mark Roseman for his friendship, countless proofreading of my work, and many useful ideas including how to write by reading from a graph. This

proved a very precious tip!

To all of you that shared the 4th floor of the Centre for the Physics of Materials, thank you for providing first-rate discussion and valuable ideas about different topics. I also learned many things about other fields of physics from these conversations.

I would like to mention that two of the things I enjoyed the most was being TA for Professors John Crawford and David Hanna teaching the signal processing and electronic labs for at least 5 years. It was a great experience to share time with them, and a wonderful opportunity to get to know most of McGill Physics undergrads during those years. It was always inspirational to be in contact with really brilliant young people.

Part of my candidature was supported by a McGill Major Fellowship, and I am tremendously thankful to McGill for this financial assistance.

At last, I will like to thank my mom and dad for their love and unconditional support, and to the greatest cheerleader ever, always a sunshine, my wife Karen. Thank you for you continuous encouragement and support. Thank you for proofreading this work, los quiero mucho....

1

Introduction

An important goal in the research community and the microelectronic industry is the production of active devices at the nanoscale. As the scales shrink, the devices operate faster and consume less power. Ultimately the greatest interest is the fabrication of Single Electron Tunneling (SET) devices. The challenge remains the elaboration of small, low capacitance (few aF) islands separated from each other by tunneling junctions. In order to work at room temperature, the island dimensions must not exceed a few nanometers. In Fig. 1.1 we show a schematic of such a device: a nanostructure in the proximity of three electrodes. In order for the device to work the nanostructure must be capacitively coupled to all the electrodes and connected by a tunnel barrier, 'tunnel coupled', to the source and drain electrodes. Some of the nanostructures that have been used successfully for fabricating working devices are: metallic nanoparticles [1], semiconductor heterostructures [2], carbon nanotubes [3], and single molecules [4]. Two major issues to be addressed are that viable nanodevices need to be electrically connected to one another and once they are integrated, the need to electrically interface them the macroscopic world. Present technologies for the fabrication of these connectors with the appropriate dimensions are hardly obtainable by conventional lithography techniques. Very ingenious ways of solving these particular issues have been proposed over the past few years. Conceptually they may be grouped as the narrow-gap electrodes approach: mechanical break junctions [5], shadow evaporation [6], [7], electrochemical plating [8], and electromigration-induced breaking of thin nanowires [9, 10, 11]. With more or less success these methods

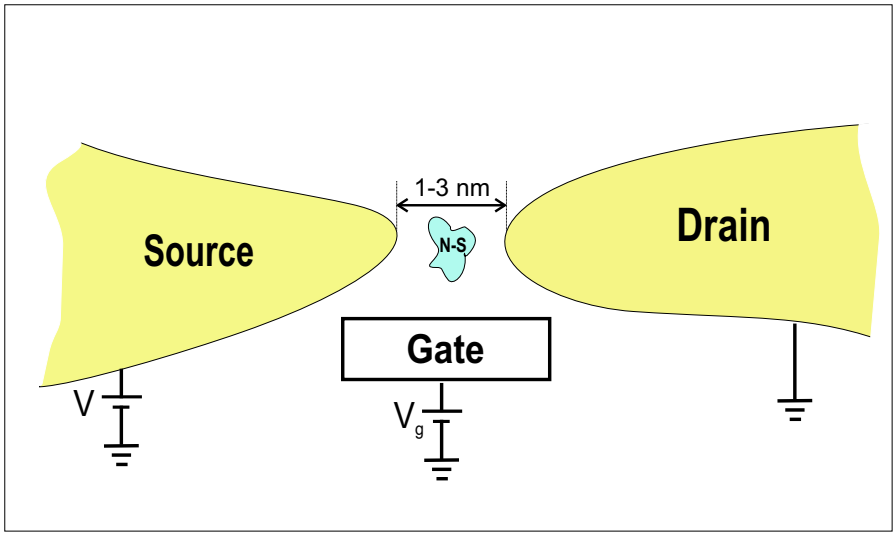

Figure 1.1: Schematic of a Single Electron Tunneling device. In order for the device to work, the nanostructure must be coupled capacitively to all the electrodes and 'tunnel coupled' to the source and drain.

presented new ways for the fabrication of gaps sized in the few nanometers range[1] (nanogaps). They allow too for integration with electrostatic gates, with techniques involving using Electron Beam Lithography (EBL) patterning being the most successful. Another way of accomplishing this goal is by implementing the tip of a scanning tunneling microscope (STM) or an atomic force microscope (AFM) as an electrode gate by individually and directly contacting a nanostructure [12], [13].

One of the most promising approaches are bottom-up self-assembly fabrication methods of nanostructures and integrated devices [14, 15, 16, 17, 18]. The realization of self-assembled integrated devices has yet to come. On the other hand, a plethora of self-assembled nanostructures have been realized. One interesting system is the self-assembled semiconductor quantum dots (SAQD) shown in Fig. 1.2 [19], [20]. These dots have shown quite exciting single electron charging phenomena [21]. Coupled quantum dots have been proposed as quantum gates by DiVincenzo and co-workers [22]. Realization of such a device by drawing electrode leads to integrate SAQDs into functional units and interfacing them to the macroscopic world may prove a cumbersome task with some of the lithographic techniques aforementioned. These

[1] Atomic in the case of break junctions.

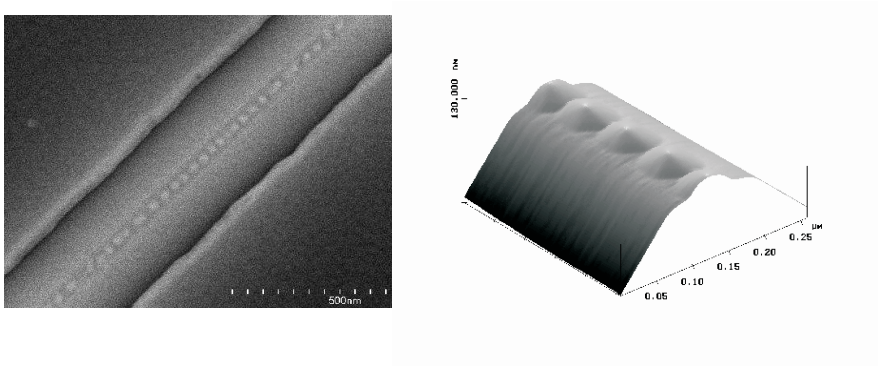

Figure 1.2: InAs SAQD patterned on a InP substrate [19].

techniques are being implemented at their fundamental size limit.

1.1 Nanofabrication with scanning probe methods

Most of the challenges posed by the limitations of conventional techniques are overcome by the implementation of Scanning Probe Microscopy (SPM)-based surface modifications techniques. Since it inception in the 1980's SPM has become an essential tool in nanoscience and nanotechnology [23], [24]. It reliably operates in a wide-range of length scales, and is inherently simple and flexible. In Fig. 1.3 we have grouped a map, with the relevant length scales involved, a group of some of the concepts and presently most used surface techniques with SPM methods.

SPM nanofabrication techniques possess attractive features as sub-nano resolution, accurate alignment and repositioning and offer a unique combination of *real-time* imaging and *direct* modification of electrical properties of a surface (*in situ* fabrication). These modifications are accomplished by manipulation (from atoms to nanostructures), local oxidation of surfaces, and deposition of material from the tip among others. Local melting by STM was one of the earliest ways of modifying a surface, but did not allow for conductive or non conductive regions to be made [25]. Also, massive parallel operation of AFM probes has been demonstrated with an increase of the throughput by over two orders of magnitude [26].

Scanning probes lithography use as exposure mechanism the very intense elec-

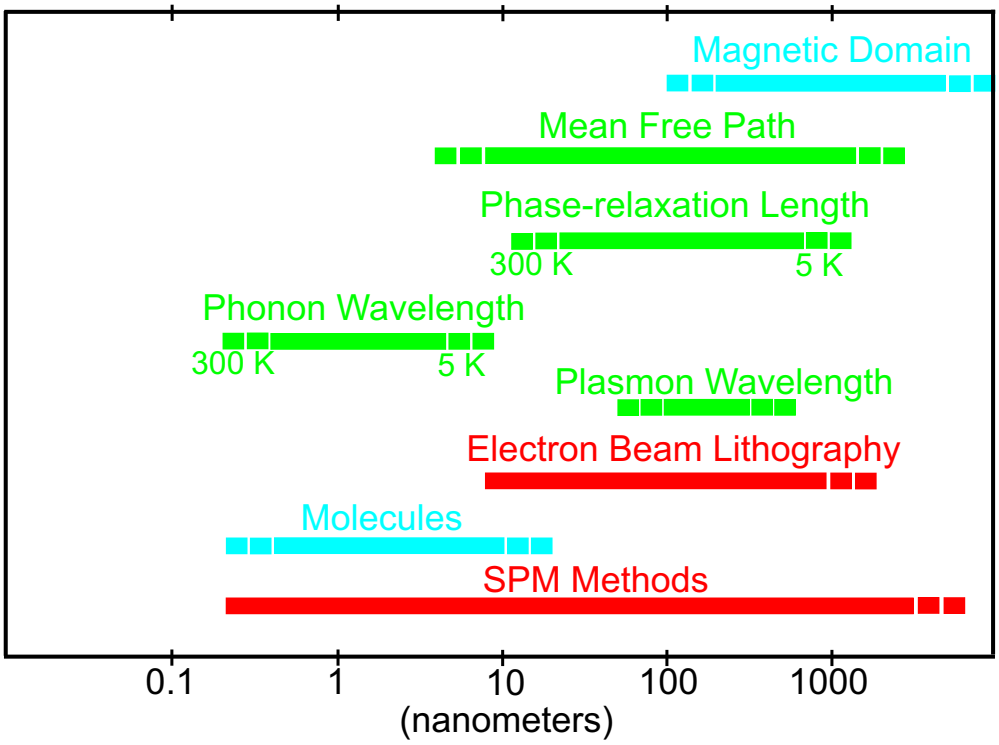

Figure 1.3: Relevant length scales [27].

tric field, usually larger than 10^9 V/m, that is established when STM tips or AFM cantilever-tips are in close proximity to a surface and a bias is applied at the tip-surface junction. This way a well-confined low energy electron beam is produced, and it has an intensity in a 1 nm spot that is a thousand times higher than focused EBL [28]. Most of the early work to create conductive regions was performed by using a STM for selective local oxidation, or material deposition [29], [30]. Oxidation is achieved by forming a water bridge between tip and sample and creating a sort of electrochemical nanocell with the tip acting as cathode [31], [32], and for field desorbing tip material, two main mechanism have been identified, atom transfer due to field evaporation [30, 33, 34], and point contact [35]. Studies were done mostly in an atmospheric environment but deposition of gold in ultra high vacuum (UHV) [36], and in liquid [37] has been demonstrated. SPM lithography has been successfully demonstrated for sub-10 nm fabrication of metal-oxide devices [38], [39].

An important disadvantage of the STM configuration is that since tip-sample

distance is controlled by maintaining a constant current it is not possible then to independently apply biases for lithographic operation. AFM methods, where feedback maintains a constant force, were soon adopted since they allow for decoupling the tip biases from the feedback control [40, 41, 42]. There is the benefit too that AFM can be operated in insulating as well as in conductive surfaces. Severe wear/contamination of the tip may be avoided if dynamic non-contact AFM methods are employed [43]. State of the art SPM lithographic techniques utilize a vibrating cantilever tip and a pulsed voltage for local oxidation or deposition of material on surfaces.

The progress of the technique and applications for the deposition of material from the tip has not been as steady as for the local oxidation case, where a more coherent view prevails and the technique has matured enough to be used regularly for the fabrication of devices like single electron and field effect transistors: SPM local oxidation technique has become a standard for the nanofabrication of tunneling barriers [39, 44, 45]. In contrast much less work has been reported on nanostructures fabricated by direct material transfer process. One the most expected applications using this method is the fabrication of conducting nanowires to be used as connectors for nanodevices. Successful deposition of gold nanowires on a Si substrate have been reported by Ramsperger and co-workers in a contact AFM scheme in UHV conditions, and by Calleja and co-workers in a non-contact AFM configuration in ambient conditions [46], [47]. Deposited nanowires were used to bridge contact leads and *in situ* electronic transport measurements characterization were performed at liquid helium temperature and room temperature, respectively. The wires grown showed ohmic behavior but in the case of Ramsperger they resulted in being extremely resistive[2]. Calleja's wires presented better electrical resistivities values, and the fact that fabrication and measurements were done in ambient conditions in a non-contact configuration and with less restrictions on the substrate's surface make it a more attractive method for the fabrication of nanowires. Despite this great achievement

[2]With an electrical resistivity of $1.5 \times 10^{-4}\ \Omega\ m$ as compared to the bulk value of gold at $1\ K$, $2.2 \times 10^{-10}\ \Omega\ m$.

details of the experimental procedure for growing the wires, particularly how to keep control of the tip-sample distance, and a characterization assessing the reliability and reproducibility of the deposition process, were not addressed.

The aim of this work is twofold. First, to develop a reliable NC-AFM deposition technique to grow nanoscale sized gold dots and wires on substrates relevant to the fabrication of self-assembled nanostructures like the one shown in Fig. 1.2. Second, through detailed characterization of the deposited structures to demonstrate that the deposition process is field evaporation.

1.2 Outline

The work is structured in 6 chapters. Chapters 3 to 5 provide the main body of this work.

Chapter 2 presents the theoretical background and the central principles on which this work is based. The chapter is divided into two sections, the first gives an introduction to and overview of Dynamic Force Microscopy. We explore and describe important concepts and distinctive features that characterize the operation of a microscope in an amplitude modulation (AM) mode, and afford extensive description of the dynamics of a vibrating cantilever. A discussion of the relevant physical parameters that allow for the construction of force-distance curves that account for the tip-sample interaction and its dependence with distance is given. Here we establish how dynamical changes on the tip oscillation are associated with the tip-sample interaction gradient. In the second section, we discuss the most important considerations of using a very sharp tip in close proximity to a surface for deposition. Historical perspectives are given and early experimental work in the field is presented, along with a thorough explanation of Field Evaporation Deposition (FED) and its implications for the deposition of gold, the influence of the tip polarity, and the role of the electric field in the deposition process. The transfer rate equation which links these theoretical considerations with the experimental results later, is presented herein.

The focus of Chapter 3 is the introduction of an electrostatic interaction force

to the tip-sample system by applying an external electric field. An immediate consequence is the transition from an intermittent contact (IC) to a non-contact (NC) operation of the AM-AFM, and here we show the technique to reliably control the tip-sample separation. Furthermore, to calculate the electrostatic force, the configuration capacitance of the tip-sample system is modeled using different geometries for the tip shape. The calculation of an 'effective area' for a parallel plates capacitor geometry suffices to reproduce, with excellent agreement, our experimental observations. This chapter further provides detailed description of the experimental setup and techniques, together with the deposition procedure for growing nanodots on the sample surface.

In chapter 4 characterization of deposited dots and the deposition process is demonstrated. Discussion of how the nanodots dimensions are affected by the amplitude and duration of the applied voltage pulse used for defining the electric field between tip and sample is given. By monitoring the dynamics of the oscillating tip we determine the system response to the application of such pulse. The characterization of the deposition process is done in terms of the existence of a threshold for deposition, measured and calculated evaporation rates, and the influence of the tip polarity. Discussion of how the tip shape affects the electric field at the tip apex is also provided. The chapter concludes with an introduction to lithographic modes for the growing of nanowires.

Electrical characterization of nanowires is presented in chapter 5, alongside current leading ideas about how transport properties are affected by the shrinking dimensions of the wire -new conduction properties and failure mechanisms- are discussed. The internal morphology (polygranular or 'bamboo' like structures) of the wire and how it affects transport & failure properties is evaluated. Furthermore we present the experimental setup for measuring electrical properties complete with detailed methodology on the device fabrication, and a discussion on overcoming 'edge problems'. A technique for electrostatically screening electrode leads and its limitations is presented. In the final section we present a detailed study of the failure mechanism for one-

terminal electrode leads. A Finite Element model is used to simulate heat dissipation of a biased one-terminal wire, and comparison to experimental observations is given.

Finally, chapter 6 presents concluding remarks and offers directions for future work.

2

Background

In this chapter we review integral elements for the fabrication of gold structures using a non-contact AFM technique. This chapter is divided in two sections. The first part covers the basics for the operation and the analytical background of a dynamically operated Atomic Force microscope. We review the most relevant aspects of Dynamic Force Microscopy that serves as a background for the rest of the experimental work to be laid down in the rest of the chapters. We will mention different operation modes but it will be emphasized that the AM-AFM technique is the one used for performing the deposition experiments. A discussion about the relevant measurable dynamic observables (like the oscillation amplitude, the resonance frequency, and the phase shift) and their behavior under experimental conditions and how they are linked to the tip-surface interactions is presented. Good reviews papers and books about these topics are available in the literature [48], [49], [50], [51], and this section is quite influenced by ideas presented in these works.

In the second part we explore the physical principles for the deposition of a material from a sharp tip to a flat sample, and specially considering it for gold, this section explores different techniques for depositing, their description and the physical aspects under which each of them are possible.

2.1 Review of Dynamic Force Microscopy

2.1.1 Forces, Sensors, and Probes

Interaction forces in play

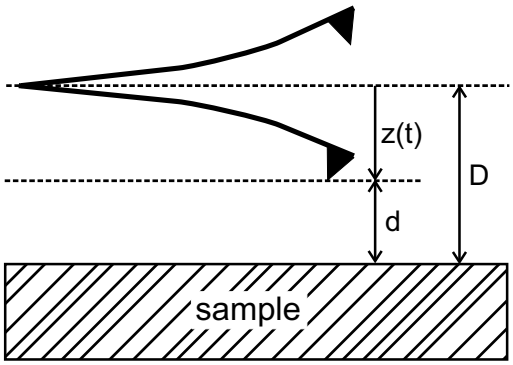

Figure 2.1: Relevant distances for the tip-sample geometry. d is the instantaneous tip-sample separation, D is average tip-sample separation, and z is the instantaneous tip position. Adapted from ref. [48].

Essentially an Atomic Force Microscope utilizes a sharp tip in close proximity to a sample surface to measure forces at the nanometric scale. Generally, the tip is mounted on a cantilever beam which gets bent by the action of the interaction forces that exist between tip and sample. In return these forces are used to map the sample surface and allow for the characterization of its properties. The potential energy between the tip and sample U_{ts} defines the z-component of the tip-sample force $F_{ts} = -\partial U_{ts}/\partial z$. The relevant forces that are present between the tip and the sample are of electromagnetic origin and they can be classified by their strength and range. F_{ts} has short- and long-range contributions according to the different parts of the tip that contribute to the total interaction force. If external fields are not present[1], the dominant interactions are:

- Attractive long-range van der Waals forces: Mostly a mesoscopic contribution. The van der Waals interaction is caused by fluctuations in the electric dipole moment of atoms and their mutual polarization. These type of forces are called dispersion forces. Their range is limited and for two atoms at distance d, the energy varies as $1/d^6$. Using the Hamaker approach, which does not take into consideration retardation effects, is possible to calculate the van der Waals interaction between macroscopic bodies. Approximating the tip-sample geometry

[1] In the next chapter we will add an external field in the form of an electrostatic force.

by a spherical tip of radius R next to a flat surface the van der Waals interaction potential is given by [49]:

$$U_{vdW}(D,z) = -\frac{A_H R}{6d}, \tag{2.1}$$

where A_H is the Hamaker constant, which is of the order of 10^{-19} J, z is the instantaneous tip position, and d the instantaneous tip-sample separation, with $d = D - z(t)$ (See Fig. 2.1). Then the van der Waals force F_{vdW} has a dependence of $1/d^2$ for this configuration. In the next chapter other configuration geometries and when they are relevant is going to be discussed.

- Repulsive short-range and contact forces: tip apex and vicinity. The Pauli exclusion principle leads to strong repulsion forces due to the electron wave overlap. Nevertheless, Pauli principle is not necessary to explain the elastic deformation suffered when two bodies, e.g. tip and sample, are brought into contact, given that the contact area involves tens or more atoms. Different continuum elasticity models that establish the relationship between the stress σ and strain ϵ and calculate contact and adhesion forces have been developed. Hertz, Johnson-Kendall-Roberts (JKR), and Derjaguin-Muller-Toporov (DMT) models provide suitable descriptions of deformation and expressions for adhesion and contact forces for different conditions, like contact stiffness, tip radii dimensions, and the strength of the adhesion forces [48].

Cantilevers

Cantilevers constitute the defining component of a force microscope, a dedicated sensor for detecting forces at the atomic level. Most AFM cantilevers are fabricated by silicon micromachining technology: they are made of single crystalline Si by microlithographic and directional etching techniques. Parallel production and well-defined mechanical properties are readily obtainable. In most cases highly doped Si is used to avoid charging. It is common too, to coat the back of the cantilever with gold or aluminum for improving reflectivity, which is necessary if a light beam deflection

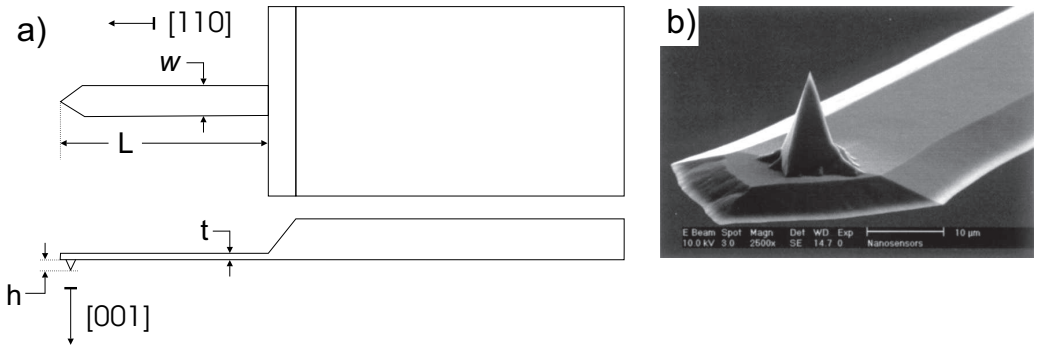

Figure 2.2: Microfabricated cantilever chip. a) Schematic: top and side view, usual dimensions for the cantilever ranges are: 25 to 50 μm, 1 to 3 μm, and 100 to 300 μm for w, t, and L respectively. The tip height h ranges from 5 to 20 μm. b) SEM scan of a NanoSensor PointProbe: a usually terminated 10 nm radius Si tip. Adapted from ref. [49].

sensor is used. A rectangular shaped cantilever is appropriate for force sensing since the rigidity on two of its axes allows for sensing normal tip-sample forces along the soft third axis. In Fig. 2.2 we show a rectangular cantilever with dimensions w, t, and L. The spring constant or stiffness k for normal bending of a cantilever with this geometry is calculated by using [52]:

$$k = \frac{Ewt^3}{4L^3}, \tag{2.2}$$

and the natural frequency f_0 is given by [52]:

$$f_0 = 0.162\frac{t}{L^2}\sqrt{\frac{E}{\rho}}, \tag{2.3}$$

where E is the Young's modulus and ρ is the mass density of the cantilever material. Eq. 2.3 is calculated from the more familiar expression for the natural resonance frequency $f_0 = \frac{1}{2\pi}\sqrt{\frac{k}{m_e}}$, where m_e is the effective mass of the cantilever[2], with $m_e = 0.24m$ [52], and by replacing k from Eq. 2.2. In these calculations the mass of the tip is not included since is negligible when compared to the mass of the cantilever. Typically for a silicon microfabricated cantilever, $E = 1.79\times10^{11}\ N/m^2$ and $\rho = 2330\ kg/m^3$, with dimensions $100\mu m \times 30\mu m \times 1\mu m$ one get for the stiffness a value of $k = 1.3\ N/m$ and a natural frequency of $f_0 = 142\ kHz$. Important considerations

[2]We have to consider that the mass m of the cantilever is distributed along its length.

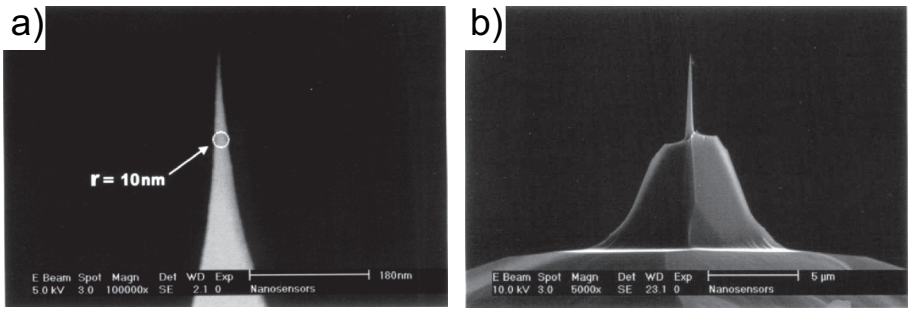

Figure 2.3: SEM images of high end silicon cantilever tips: a) Supersharp with a less than 10nm radius, and b) Very high aspect sharp tip. Images courtesy of NanoSensors GmbH.

regarding the relative values for k and f_0, together with the quality factor Q are among the important properties to be considered when designing an experiment.

The probing tip

Micromachined cantilevers can be fabricated with an integrated tip, as can be see on the schematic side view shown in Fig. 2.2 a). The tip points in the [001] direction. The tip can be tetrahedrical or of conical shape with half-cone angles usually in the 20 degrees. The tip height h is usually in the range of 5 to 20 μm. The study of atomic arrangement of non flat surfaces, like facets on islands or on vecinal surfaces, and nanotechnology applications demand the use of tips with very sharp apexes, high aspect ratios, and well-known, reproducible geometry. The radii of these tips need to be in the order of few nanometers to 10 nm. Development of sharper tips is currently still a major concern. Complicated etching process and techniques are in used to produce the utmost sharp tip. In Fig. 2.3 we show some of such tips which are fabricated and commercialized by NanoSensors.

In order to perform metal deposition from a tip or use it as an electrostatic force sensor some modification of the tip is necessary. This is usually accomplish by thin film deposition of selected metals by physical evaporation methods. Further functionalization of the tip can be realized by a variety of methods depending on the forces or chemical affinities to be sensed by the tip.

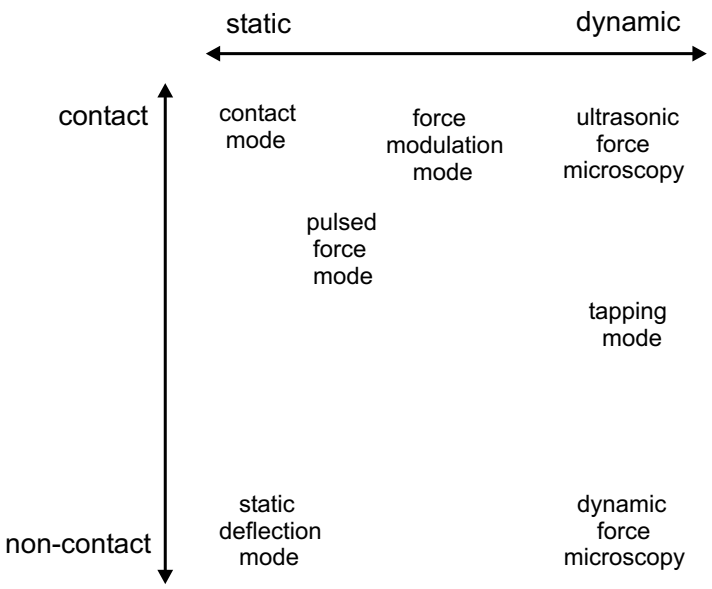

Figure 2.4: Modes of operation in force microscopy. Adapted from ref. [50]

2.1.2 Operation modes, Instrumental aspects

Figure 2.4 gives an idea of some of the most used operation modes in Force Microscopy. Static modes relies in the force F_{ts} that produces a static deflection (F_{ts}/k) of the cantilever. Historically, contact mode was the first method used to measure the surface topography of a sample using an AFM. In this mode the tip is always in contact with the surface of the sample. The value of the spring constant k is limited by the interatomic force constants for the materials of the tip and sample since the deflection has to be larger than the tip-sample deformation. Typical values range from 0.01 to 5 N/m. Tip-sample distance is controlled with a feedback loop in order to maintain a constant force, a topographical image is obtained under this condition. The image is map $Z(X, Y, F_{ts} = const)$ In contrast, in dynamic operation a piezo-actuator is used to vibrate the cantilever. Changes in the oscillations properties of the vibrating cantilever due to tip-sample interactions are measured. Basically, there are two dynamic methods which differentiate from each other by which feedback parameters are used for distance control:

- Amplitude-Modulation (AM)-AFM: the cantilever is driven near to its reso-

nance frequency and when the probe is close to the sample, changes in the oscillation amplitude or phase (as compared to the free oscillation values) are used as feedback parameters to measure the surface topography. Since the changes in oscillation amplitude occur in a time scale that is related to the quality factor Q, as we will see in section 2.1.3, this technique is too slow to be practically used in a high vacuum environment where the Q-values usually reach 10^4. This technique is suitable to be operated in air or in liquids, where Q's are typically a few hundred due to the increased damping.

- Frequency-Modulation (FM)-AFM: the cantilever is driven at its natural resonance frequency with a fixed oscillation amplitude. When tip and the sample surface are at interacting distance the resonance frequency of the cantilever is changed. This shift in the resonance frequency is used as a source of contrast to map the surface. In this operation mode the measurement bandwidth does not depend on the Q-value since the changes in resonance frequency occur within a single oscillation cycle. To reduce the viscous damping and thus increase Q this technique is implemented in high vacuum environments. At the moment this is the only operation mode capable of routinely producing true atomic resolution. This mode of operation is rather more complicated to implement than AM-AFM since it requires two feedback loops and high vacuum equipment.

In both methods cantilevers are quite stiff as compared to the ones used in contact mode, the k values are in the order of tens of N/m. Dynamic operating modes were initially thought to be non-contact (NC) methods, meaning that the tip and sample will be interacting exclusively in the attractive regime, but actually AM-AFM is mostly used in a mixed mode in which the tip and sample interact briefly in the repulsive regime. The tip 'gives a tap' to the surface once every cycle, while the tip vibrates with rather large oscillations of about 20 to 100 nm. This mode is called intermittent-contact (IC) or tapping mode[3], and is widely used for routine surface topographic imaging and other characterization studies.

[3]TappingMode^{TM} is a registered tradename by Digital Instruments.

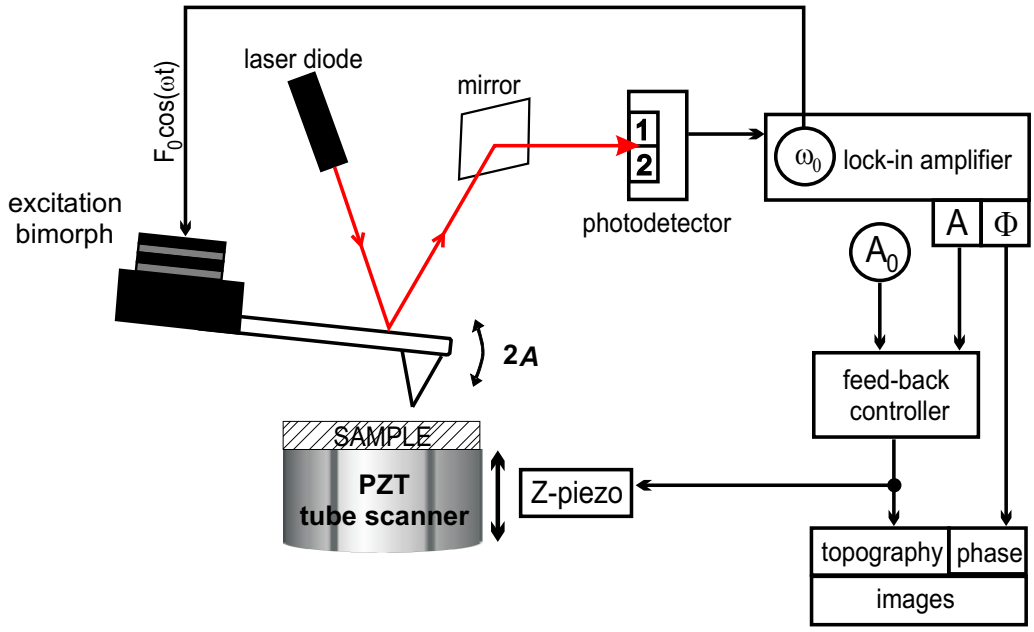

Figure 2.5: Instrumentation diagram for AM-AFM. Adapted from ref. [50].

AM-AFM Setup

A very basic concept diagram of a dynamically operated microscope can be observed in Fig. 2.5. In this technique the cantilever is mechanically excited by a bimorph located on the cantilever mounting base. The bimorph is formed by two plates of piezoelectric material joined together so that one expands on the application of a potential difference and the other contracts. The response of the cantilever to the drive depends on the drive frequency and the natural resonance frequency f_0 of the cantilever. At f_0 the probe is in resonance with the drive frequency and whips up and down at a higher amplitude for a given driven voltage. The cantilever probe also lags the driving signal. This lag is referred as the phase shift ϕ. Above f_0 the phase shift can reach 180° and the amplitude of oscillation will be greatly reduced. Later on we will describe how tip-sample interactions control the behavior of the oscillating probe: the proximity of the probe to the sample surface produce changes, with respect to the drive, in the phase $\Delta\phi$ or in the amplitude ΔA that are detected by measuring the deflection of the oscillating cantilever. For this experiment the deflection sensor employed uses the beam-deflection technique, which is one of

the most commonly used [50] In this technique a laser diode light is reflected from the back of the cantilever, and then detected in a multiple-stage position-sensitive photodetector as seen in Fig. 2.5. The cantilever-photodetector distance is generally thousands of times the length of the cantilever. As a consequence, the optical lever greatly magnifies the motion of the tip, $\approx$ 2000-fold magnification, and theoretically a noise level of 0.01 $pm/\sqrt{Hz}$ can be obtained [53]. Only techniques like tunneling detection and interferometry have approached this value.

Z-positioning and (X, Y)-scanning of the sample is accomplished by the use of a piezoelectric ceramic tube made of lead zirconium titanate (PZT). Elongation of the tube scanner by applying an actuating voltage to the single electrode contacting the inner wall, is used for vertical movement. Horizontal scanning movement is obtained by the bending of the tube scanner: applying equal but opposite voltage to two pairs of opposing electrodes contacting the exterior wall.

A closed-loop feedback system is used to control the Z-position (the tip-sample separation): the oscillating photodetector output is compared with the input oscillation of the drive through lock-in amplifier. The output is proportional to either the change in oscillation amplitude or to the change in phase, which is used to control the feedback to the Z-piezoelectric ceramic and to generate the $Z(X, Y)$-data point. The collection of $Z(X, Y)$ points, line by line, are then used to form a topographical image of the surface on a rectangular frame. The resolution of these lines is usually 128, 256 or 512 data points.

2.1.3 Dynamics of a vibrating tip

A complete solution of the equation of motion of a three-dimensional vibrating cantilever-tip system in close proximity to a surface and considering tip-surface interactions is a quite challenging task. A first good approach is to consider the oscillating cantilever-tip system as a point-mass spring, with an effective mass m. If the tip and surface are not interacting ($F_{ts} = 0$) i.e. the oscillating cantilever-tip system is far from the sample surface, then the system can be described by the motion of a forced harmonic

oscillator with damping:

$$m\ddot{z} + \frac{m\omega_0}{Q}\dot{z} + kz = F_0\cos(\omega t), \tag{2.4}$$

where Q is the quality factor, $\omega_0 = 2\pi f_0$ is the angular resonance frequency, k is the spring constant of the free cantilever, and the amplitude and angular frequency of the driving force are F_0 and ω, respectively. This equation can be rewritten as:

$$\ddot{z} + \gamma\dot{z} + \omega_0^2 z = \frac{F_0}{m}\cos(\omega t), \tag{2.5}$$

with $\gamma = \omega_0/Q$ is the damping coefficient or drag of the cantilever-tip motion. The solution of this equation is [54]:

$$z = B\exp(-\alpha t)\cos(\omega_r t - \phi) + A\cos(\omega t - \phi). \tag{2.6}$$

The transient term, first term at the right of the equation, is reduced by a factor $1/e$ after a time $\tau = 2/\gamma = 2Q/\omega_0$. After that time the the steady term, second term at the right of the equation, is the dominant term of the solution. Typically the system reaches equilibrium after a time 3τ. For typical experimental values of $Q = 850$, and $f_0 = 175\ kHz$, the steady state time is about 5 ms. Now, to form an image with a resolution of 512×512 points it will be needed $5 \times (512)^2\ ms$ or about 20 min. In the steady term in Eq. 2.6, A is the amplitude of the vibration, and ϕ is the phase lag with respect the excitation force. If we solve Eq. 2.5 with this term only, the expresions for amplitude and phase shift as a function of the excitation amplitude are given by:

$$A(\omega) = \frac{F_0/m}{[(\omega_0^2 - \omega^2)^{2+\gamma^2\omega^2}]^{1/2}}, \tag{2.7}$$

$$\phi(\omega) = \arctan\left(\frac{\gamma\omega}{\omega_0^2 - \omega^2}\right). \tag{2.8}$$

The expression for the amplitude is that of a Lorentzian centered at the resonance frequency. In Fig. 2.6 we show a typical response of a driven cantilever on our AFM system. In it we can appreciate the predicted behavior, for the amplitude and the phase shift in overall agreement with the above expressions. Some of the irregularities

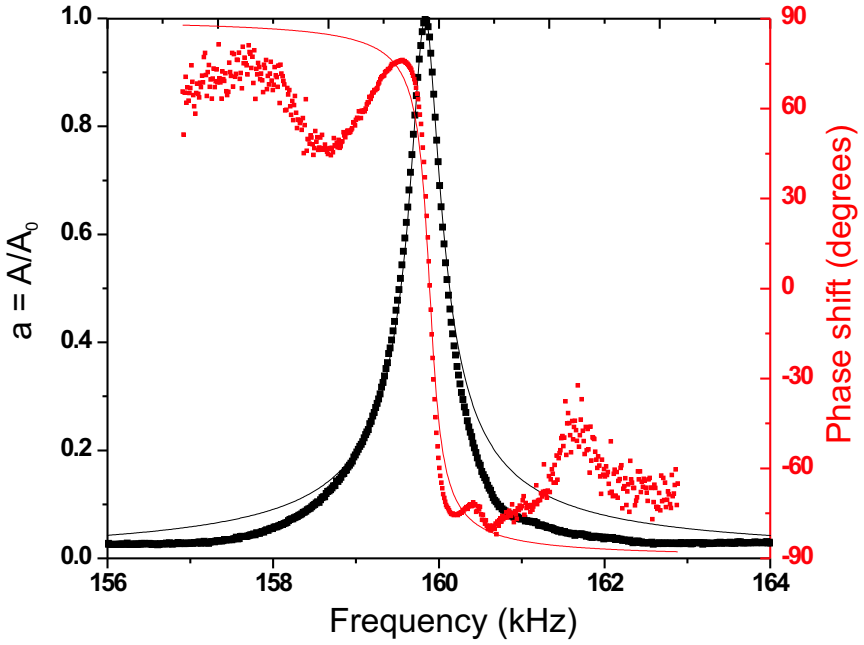

Figure 2.6: Experimental (dotted plots) and theoretical (solid line plots) resonance curves of amplitude (in black) and phase shift (in red). Experimental curves where obtained by sweeping the driving frequency and with the tip far from the surface. Theoretical values are calculated using equations 2.7 and 2.8, the natural frequency for this particular cantilever is $f_0 = 160\ kHz$, the quality factor is 470, and $\gamma \approx= 2140\ s^{-1}$.

that are present are owned to the fact that there are parasitic resonances that originate in the mechanical coupling of the cantilever with the excitation bimorph.

Once the tip approaches the surface tip-sample interactions are present and an extra force term has to be added at the right side of Eq. 2.4. For the sake of simplicity and first hand understanding of how the oscillation amplitude $A(\omega)$ is affected, lets assume that the tip is under an influence of a parabolic interaction potential. In this case, for small oscillations, the total force $F(z)$ can be represented as a Taylor series around the equilibrium position z_0:

$$F = F_0 + \left(\frac{dF}{dz}\right)_{z_0}(z - z_0), \tag{2.9}$$

The total force includes the elastic response kz and the interaction force F_{ts}. The effective spring constant k_e is given by:

$$k_e = -\frac{dF}{dz} = \left(k - \frac{dF_{ts}}{dz}\right)_{z_0}, \tag{2.10}$$

and the new resonance frequency becomes:

$$\omega_e = \left(\frac{k - \frac{dF_{ts}}{dz}}{m}\right)^{\frac{1}{2}}. \tag{2.11}$$

As a consequence of the interaction the system is taken off-resonance by $\Delta\omega = \omega_e - \omega_0$ which results in the reduction of the amplitude oscillation. Eq. 2.11 shows that in the dynamic mode the system reacts to the *gradient of the interaction* rather than the interaction itself as occurs in contact mode. A 20% amplitude reduction is typical for stable microspe operation. Under this circumstances one must find at what excitation frequency ω_s the amplitude is the highest or when $\frac{d^2A}{d\omega^2} = 0$. For high Q values the solution can be written as [55]:

$$\omega_{s\pm} = \omega_0\left(1 \pm \frac{1}{\sqrt{8}Q}\right), \tag{2.12}$$

and

$$\frac{dA}{d\omega}(\omega_{s\pm}) = \pm A_m \frac{4Q}{3\sqrt{3}\omega_0}, \tag{2.13}$$

where A_m is the maximum amplitude of the oscillator. Using Eq. 2.11 is possible to find an expression that relates small amplitude variations to the force gradient:

$$\Delta A = \frac{dA}{d\omega}(\omega_s)\Delta\omega = A_m \frac{2Q}{3\sqrt{3}k}\frac{\partial F}{\partial z}(z_0). \tag{2.14}$$

The dependence of the oscillation amplitude A on the excitation and effective resonance frequencies, equations 2.7 and 2.11, offers a way to relate the amplitude and phase shift to the tip-sample separation by considering the interaction strength. To further develop this idea, a non-perturbative approach has been developed by Aimé and co-workers [56], [57]. In this case a variational method based on the principle of least action is used to study the non-linear behavior of a damped, driven harmonic oscillator in an external potential. The principle of least action specifies that a variation of the action $S[z(t)]$ is an extremum:

$$\delta\left\{S[z(t)]\right\} = \delta\left\{\int_0^{2\pi/\omega} L(z,\dot{z},t)dt\right\} = 0, \tag{2.15}$$

where L, the Lagrangian of the system, which is given by:

$$L(z,\dot{z},t) = T - U + W = \frac{1}{2}m\dot{z}^2(t) - (\frac{1}{2}kz^2(t) - z(t)F_0\cos(\omega t) + U_{ts}) - \gamma z(t)\underline{\dot{z}(t)}, \tag{2.16}$$

a dissipation term W of the type $z(t)\underline{F_d}$ is introduced, with $\underline{F_d} = -\gamma\underline{\dot{z}(t)}$. Underlined quantities are calculated along the physical path, thus are not a varied parameter. The term U_{ts} represents the interaction potential between tip and sample. In a non-contact configuration with small oscillation amplitudes only the purely attractive part of the interaction potential is of interest[4]. In this case U_{ts} is given by the non-retarded van der Waals interaction potential U_{dvW}, Eq. 2.1. Since we are interested in studying the behavior of the harmonic solution, a trial function of the type $z(t) = A\cos(\omega t - \phi)$ is chosen, which is the steady part of solution 2.6. The parameters of the path are A and ϕ, the two observables in which we are interested. In this case Eq. 2.15 becomes a set of two partial differential equations:

$$\frac{\partial S}{\partial A} = 0, \tag{2.17}$$

[4]In contrast, for large oscillation amplitudes the repulsion during contact dominates.

$$\frac{\partial S}{\partial \phi} = 0. \tag{2.18}$$

The solution of this system is two coupled non-linear equations. After some long calculations, the expressions for the oscillation amplitude as a function of the tip-sample separation $A = f(d)$, and for the phase shift as a function of the tip-sample separation $\phi = f(d)$, are given by [57], [56]:

$$d_{A\pm} = \sqrt{a^2 + \left(\frac{k_{vdW}}{(1-u^2) \mp \frac{1}{Q}\sqrt{\frac{1}{a^2} - u^2}} \right)^{\frac{2}{3}}}, \tag{2.19}$$

and

$$\phi_{A\pm} = arctan\left(\frac{u}{Q(u^2-1) + Q\frac{k_{vdW}}{(d_{A\pm}^2 - a^2)^{\frac{3}{2}}}} \right). \tag{2.20}$$

where $a = A/A_0$ is the reduced amplitude, $d_{A\pm} = D/A_0$ is the reduced tip-sample separation distance, $u = \omega/\omega_0$ is the reduced frequency, A_0 and ω_0 are the amplitude of free oscillation and the natural resonance frequency, respectively, and $k_{vdW} = \frac{A_H R}{3kA_0^3}$ is a dimensionless coupling strength parameter, related to the van der Waals force strength. The plots of $A = f(d)$, and $\phi = f(d)$ are commonly referred to as the force-distance curves[5]. They reflect the contribution of the different interactions gradients with tip-sample separation. These curves allows identification of the operation mode at which the AM-AFM is working. By modifying experimental parameters one can choose a working regime. Later, in the next chapter, an extra coupling strength term will be introduced which will allow for the operation of our AM-AFM in a non-contact mode. We will provide there experimental and theoretical force-distance curves.

2.1.4 Resolution

Microscopes are characterized by their resolution capabilities. In AM-AFM resolution is determined by the tip size, tip-surface separation, tip-surface force and sample compliance. An AFM renders a 3-D image of a surface and consequently there is a

[5]Highlighting the fact that $A(\omega)$, Eq. 2.7, and $\phi(\omega)$, Eq. 2.8, have a dependence on the force gradient through Eq. 2.11.

lateral resolution and vertical resolution. For an AFM microscope it is common to consider that is the resolution with respect to the object real dimensional values that is important and not only the ratio between the size and the number of pixels of the rendered image.

The shape of the AFM-tip is responsible for the overestimation of lateral dimensions, which is usually the case when AFM's are used for the measurement of surfaces and surface details. The AFM rendered image is then a convolution between the tip geometry and the structure's real shape. Tip selection[6] and application of deconvolution algorithms contribute to reduce this broadening effect.

Thermal fluctuations of the cantilever cause unwanted bending of the cantilever and change on f_0 which ultimately limit the vertical resolution. Considering the equipartition theorem, the mean thermal motion of the cantilever can be calculated by [48]:

$$\sqrt{\langle z^2 \rangle} = \sqrt{\frac{4k_B T}{3k}}, \tag{2.21}$$

where $\langle z^2 \rangle$ is the mean square deflection, $k_B T$ is the thermal energy, and k is the spring constant of the cantilever. To calculate the minimal detectable force in dynamic modes we consider a periodic force F_ω acting on the cantilever, then the amplitude is given by [50]:

$$z_{\omega=\omega_0} = Q\frac{F_\omega}{k}. \tag{2.22}$$

Now the minimal periodic force F_{min}^{dyn} that causes a detectable deflection of the cantilever happens when $z_{\omega=\omega_0} = \sqrt{\langle z^2 \rangle_{\omega=\omega_0}}$, which in light of two previous equations gives us an expression for the minimal detectable force:

$$F_{min}^{dyn} = \sqrt{\frac{2k_B T k B}{\pi\omega_0}}Q, \tag{2.23}$$

where B is the measurement bandwidth. A silicon cantilever with a stiffness of 45 N/m and $T = 300\ K$ will have thermal fluctuations below 0.011 nm. Noise from the detection system contributes to a limited vertical resolution. Nevertheless thermal

[6] Considering sharpness, aspect ratio, and tilt angle of the tip and the stiffness of the cantilever.

noise of the cantilever is the largest source of noise in AFM [48]. This can be reduced by using other materials instead of silicon for the fabrication of the cantilever.

2.2 Deposition Mechanism

2.2.1 Introduction

Since the first STM systems came into operation it has been observed that some kind of manipulation of the surface of the samples is possible while the probe is scanning [58], [59]. It was soon discovered that when low voltage pulses of either polarity are applied to the tip or the sample there is mass transfer between tip and sample and it can be directly observed on the scanned image as shown by the pioneering work of Mamin and co-workers [30]. This process of mass transfer was immediately related to the physical process associated with the Field Ion Microscopy (FIM). In this case a very intense positive (tip positive) electric field on the order of tens volts per nanometer is established. This field has enough strength to desorb atoms in the form of positive ions from the surface of the tip and is referred to as Field Evaporation [60]. Even though Mamin and co-workers explained the creation of Au mounds on the surface by field evaporation deposition (FED) of gold ions, with either polarity of the tip, other researchers found that nanodeposits can be created too by mechanical contact between tip and sample [35]. At this time it was thought that these processes were exclusive of each other and prompted Pascual and co-workers, with their experimental results, and Tsong [33], from theoretical calculations, to dismiss field emission as an 'unlikely' explanation for the deposition process. At this point it was not even clear that negative field emission was possible, since it has not been observed on FIM systems. Later Miskovsky and Tsong showed that negative field evaporation for single- and double-electrode systems (as in FIM or STM respectively) is possible but not likely for the FIM configuration. For the STM system using a gold tip and a gold substrate sample, negative field evaporation is most probable, specifically in the form of the Au^{2-} ions (which have lower threshold field) [34].

Mamin and Rugar in a published comment pointed out that the point contact,

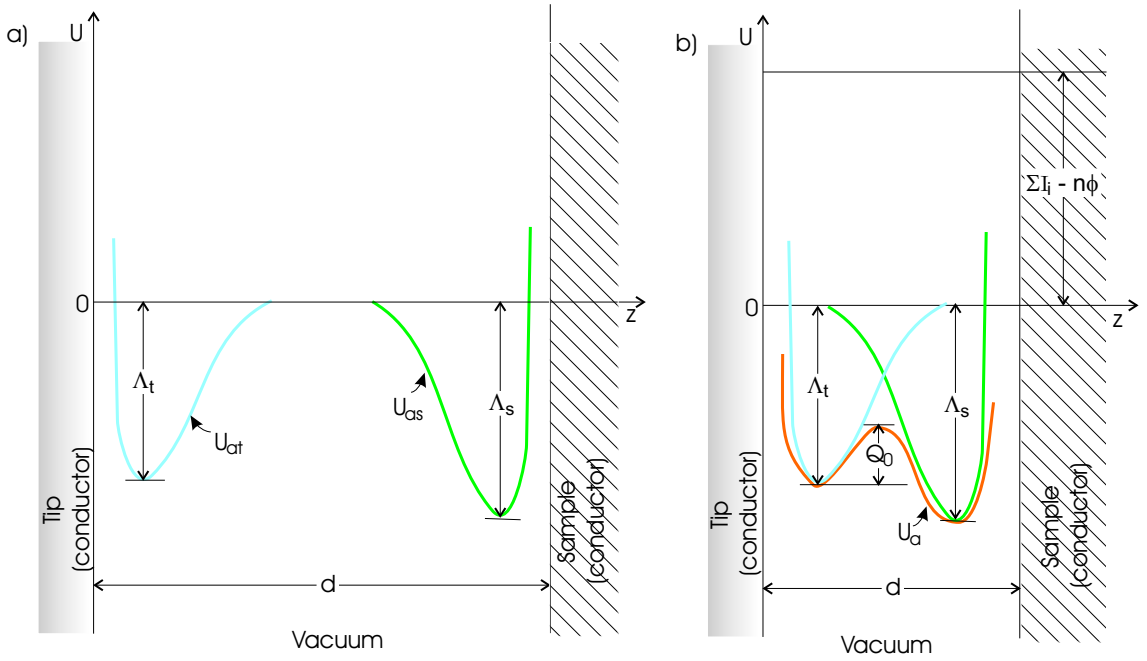

Figure 2.7: Simplified atomic potential digram for the tip-sample system. (a) When the separation distance d is comparatively large, the tip-atom U_{at} and the sample-atom U_{as} interaction potential do not overlap. Λ_t and Λ_s are the binding energy to remove an atom from the surface of the tip or the sample, respectively. (b) When d is shortened the total potential energy curve U_a shows a potential barrier of height Q_0. This barrier is considerably smaller than Λ_t and Λ_s.

deposition by contacting the tip and surface, may be seen as a consequence of a growing mound that eventually fills the gap between tip and sample and thus forming a bridge [61]. Is now better understood that both process are possible, and that they are quite distinguishable, being dependence on the polarity of the field the most important difference. In both cases, except for the case of FED with positive field, the high electric field will produce a 'field-gradient-induced surface diffusion: atoms at the tip shank will diffuse to the tip apex' [33], [62]. In the next subsections we will discuss briefly the mechanism for these deposition processes.

2.2.2 Field Evaporation Deposition

Deposition of tip material to the sample surface by ionization and field evaporation of atoms of the tip can be explained as follows, keeping in mind that the explanation of this mechanism is by no means complete. This explanation is an extension of the Charge Exchange (CE) model of FIM to the STM (or AFM) configura-

tion [30], [33], [34]. Figures 2.7 and 2.8 shows how the increased proximity between tip and sample and the subsequent application of an electric field make it energetically favorable for an atom to be emitted. Near room temperature the binding energy of an atom on the tip Λ_t or on the sample Λ_s, Fig. 2.7(a), is big enough that thermally activated transfer can not be initiated. In Fig. 2.7(b) as tip and sample are approached the total potential-energy curve $U_a(z)$ of an atom interacting with tip and sample exhibits a hump of height Q_0 from the tip side. This is the energy needed to remove an atom from the tip with no applied field. In a similar way is possible to remove an atom from the sample and the energy needed is $Q_0 + (\Lambda_s - \Lambda_t)$. The direction of the atom transfer depends on the relative magnitudes of Λ_t and Λ_s. One can get an idea of the value of Q_0 by using the Arrhenius equation:

$$\kappa = \nu \exp(-\frac{Q_0}{kT}), \tag{2.24}$$

where κ is the transfer rate of atoms from the tip, ν is the vibration frequency in the degree of freedom leading to atoms transfer, assumed to be 10^{13} s^{-1}, k is the Boltzmann constant, and T is the tip temperature [63]. For transferring at a rate of 1 s^{-1} at 300 K we need a Q_0 of 0.772 eV, compare this value to typical Λ_t values of some metals: 2.96 eV for Ag, 3.78 eV for Au, 4.63 eV for Si, 5.85 eV for Pt, and 8.66 eV for W. How close the tip and sample should be so Q_0 is 0.772 eV? For answering this we need an expression for the total ionic potential of positive ions at zero applied field [33]:

$$U_i^{n^+}(0,z) = U_{im}(z) + U_{rep} + \sum_{i=1}^{n} I_i - n\varphi, \tag{2.25}$$

where the first term is the image potential for a double-electrode system, the second term is the repulsive potential of the ion-surface interaction, the third term is the total ionization energy of the atom to the n^+ charge state, and the last term is the energy regained by n electrons when returned to the tip surface at the Fermi level, where φ is the work function of the tip surface material, see Fig. 2.7(b). Here it has been assumed that both surfaces are metallic. A calculation using equation 2.25 shows that when the tip-sample separation is close to 5.5 Å then $Q_0 = 0.772$ eV [34].

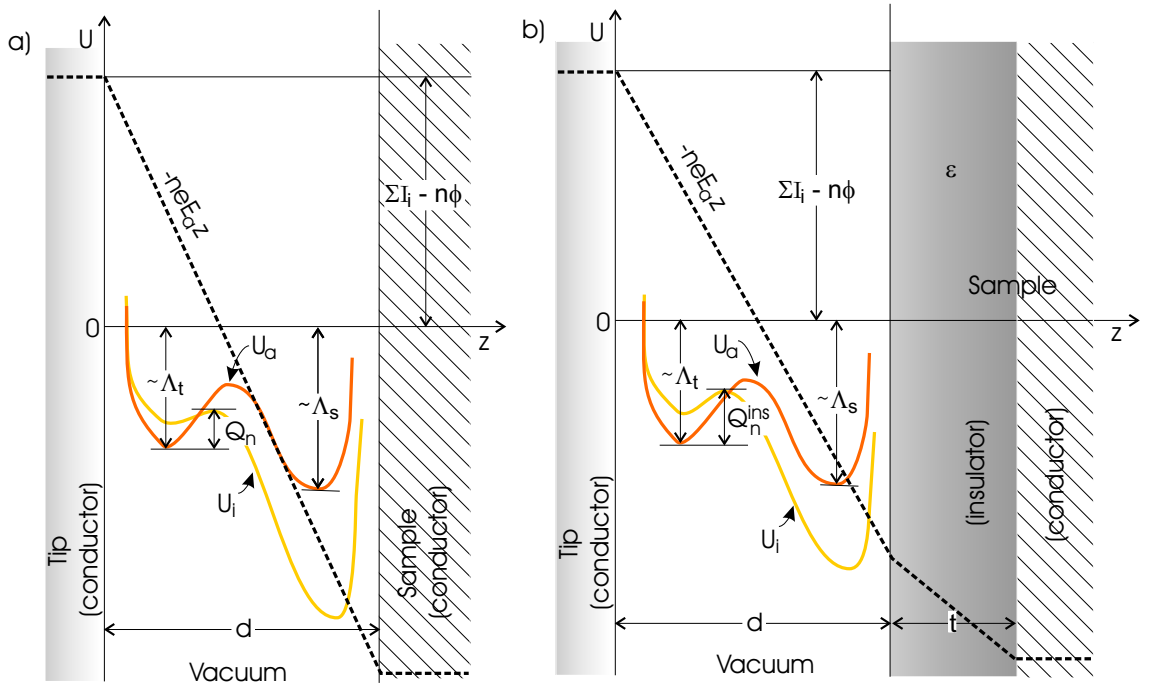

Figure 2.8: Simplified atomic potential digram for the tip-sample system with applied field E_a. (a) Ionic and atomic potential energy curves with applied field E_a. The activation energy Q_n is significantly smaller than Q_0 in Fig. 2.7(b). (b) When an insulator of permittivity ϵ and thickness t is in the junction the activation enrgy Q_n^{ins} is increased.

Is important to notice that continuous transfer of atoms is not possible because it is very difficult to create ad atoms repeatedly at the tip or sample surface. Atoms can be transfered either way at the same rate too. Sustainability and directionality of the transfer, and further reduction of Q_0 can be achieved by applying an electric field E_a. The new expression for the total ionic potential of positive ions with applied positive field E_a is:

$$U_i^{n^+}(E_a, z) = U_i^{n^+}(0, z) - neE_a z. \tag{2.26}$$

Because of the intense gradient of the field at the surface of the tip, an induced migration of atoms from the shank to the tip apex will be created. At the same time the temperature of the tip apex is increased considerably and is enough to cause the field evaporation of an ion species with the lowest evaporation field (in magnitude). The activation energy for field evaporation of positive ions with charge state n, Q_n,

see Fig. 2.8(a), is given by [33]:

$$Q_n = \Lambda_t + \sum_{i=1}^{n} I_i - n\varphi - \frac{n^2e^2}{4r_0} - \frac{n^2e^2}{4(d-r_0)} - nE_a r_0, \tag{2.27}$$

here d is the tip-sample separation, r_0 is the atomic radius of ions in the tip metal, and terms fourth and fifth are the image potentials of the field-evaporated ions for the metallic tip, and the conductive substrate. Until now we have only discussed field evaporation of positive ions, for negative ions in the n^- charge state the term $(\sum_{i=1}^{n} I_i - n\varphi)$ in equations 2.25 and 2.27 need to be changed to $(n\varphi - \sum_{i=1}^{n} A_i)$, where $\sum_{i=1}^{n} A_i$ is the total electron affinity of the tip atom. In other words, in zero field the energy needed for producing a negative ion, in the n^- charge state, from a particular surface is $(\Lambda_t + n\varphi - \sum_{i=1}^{n} A_i)$.

It has been estimated that for evaporating gold, with $Q = 0.772$ eV, field thresholds are 23.8 V/nm, 12.5 V/nm, and 11.3 V/nm for Au^+, Au^-, and Au^{2-} respectively. This calculation was made using the CE model, summarized in the equations previously given, and an embedded-atom method (EAM) to calculate the potential energy curves of the atom-surface interaction [34]. In this way if a positive field is applied and both surfaces are gold, evaporation of the Au^{2-} from the sample will occur, now if the tip polarity is reversed deposition of the same ion will happen from the tip. Notice that if the sample material is different from the one of the tip then it may be possible to deposit with any tip polarity (different ion species) if the threshold for field evaporation of both ion species are lower to the ones on the sample.

The previous discussion explains field evaporation between tip and sample both with conductive surfaces but what about when field evaporating to an insulating surface? Modifications to Eq. 2.27 will be needed. Fig. 2.8(b) shows the new energy diagram for the metal-probe/vacuum/insulator/conductor configuration when an insulator of permittivity ϵ and thickness t is introduced. In this case Q_n will be [41]:

$$Q_n^{ins} = \Lambda_t + \sum_{i=1}^{n} I_i - n\varphi - \frac{n^2e^2}{4r_0} - \frac{n^2e^2}{4(d-r_0)}\left(\frac{\epsilon-1}{\epsilon+1}\right) - \frac{n^2e^2}{t\epsilon} - n\left(\frac{V}{d+t/\epsilon}\right)r_0, \tag{2.28}$$

where the second to last term corresponds to the image potential for the insulator, on the last term we have made the substitution $E_a = V/d$, and we have assume that

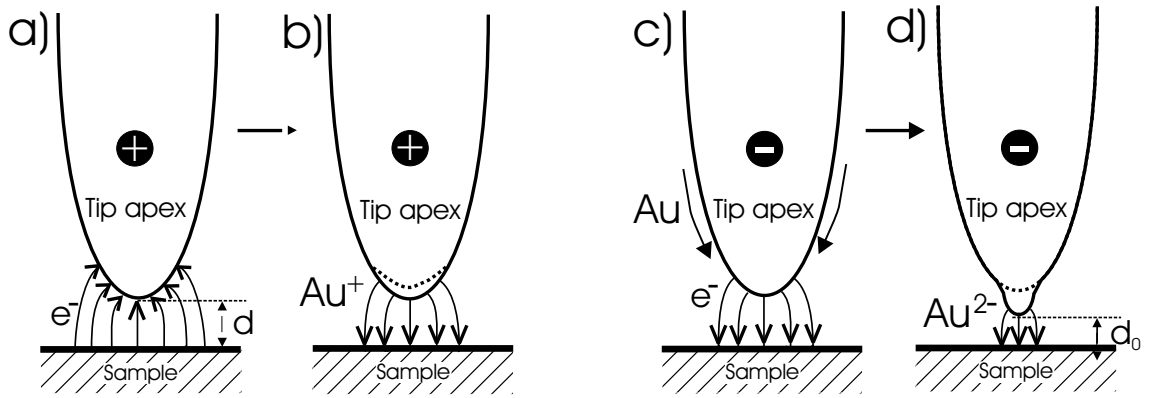

Figure 2.9: Field evaporation deposition. (a), (b) Positive field. In this case the field gradient is not as intense on the tip apex. Electrons from the sample will hit a large area close to the tip apex. Field evaporation for the cation Au^+ will happen when the threshold field is reached, field close to 23.8 V/nm. (c), (d) Negative field. Field gradient lines are very dense at the tip apex. Hydrodynamic flows of atoms and intense heating of the tip creates a protrusion at the apex, when the field exceeds 11 V/nm field evaporation of Au^{2-} will happen. The distance between tip and sample is reduced by the creation of this protrusion.

$(d - r_0) << t$ for this expression to be valid. Now the change in the activation energy ΔQ, the difference between Q_n^{ins} and Q_n, when an insulator is introduced can be expressed as:

$$\Delta Q = \frac{3.6n^2}{r_0}\left(\frac{2t\epsilon - (d - r_o)(\epsilon + 1)}{t\epsilon(d - r_0)(\epsilon + 1)}\right) + \frac{nr_0V(t/\epsilon)}{d(d + t/\epsilon)}\ [eV], \tag{2.29}$$

in this equation distances and thickness are expressed in [Å]. When an insulator is introduced the image force is weakened and as a result the threshold field for deposition is larger, an extreme case of a very thick insulator will reproduce fields as large as the ones needed for deposition using FIM systems. It worth mentioning that because larger fields are needed in this system, field evaporation of negative ions, negative field deposition, it is not possible for the FIM configuration [60]. As an example for field evaporation of gold in the FIM system, on the form of Au^+, a field strength of 35 V/nm is required. Using arguments based on the previous theoretical discussion a schematic explanation for FED follows. Figure 2.9 shows diagrams for FED of gold atoms in a positive and in a negative field, as referred to the tip, for a double-electrode system, like the STM. When tip and sample are close enough and the field strength is approximately 3 V/nm electron emission will start,

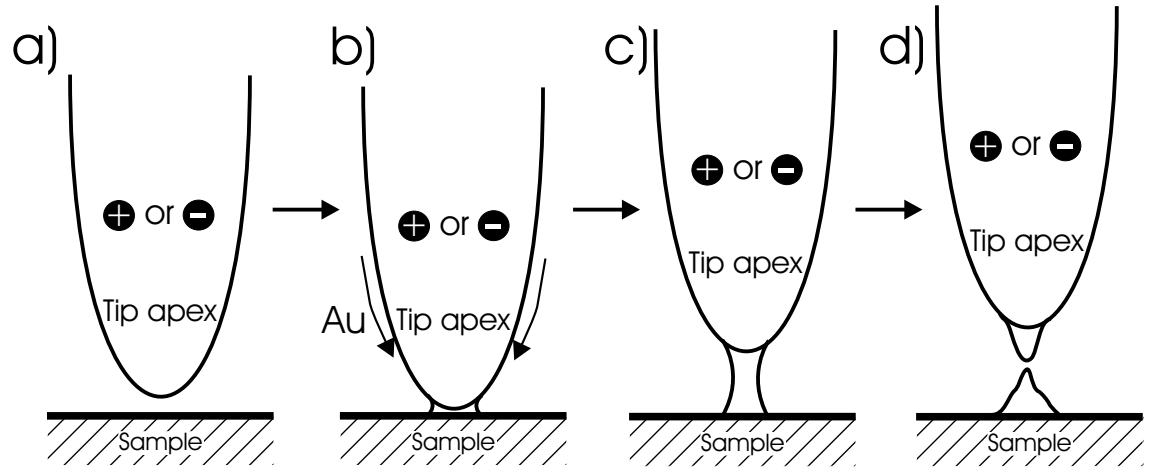

Figure 2.10: Point Contact. (a) Tip on very close proximity to the sample (4 to 6 Å). (b) When a high electric field is applied, atoms migrate by field enhanced diffusion to the tip apex and a point contact is formed. (c) Tip withdraw by feedback control. (d) Mound of deposited material left on surface.

Fig. 2.9(a),(c). For positive field electron bombardment of the tip occurs, because of momentum conservation, in a fairly large area. It is reasonable to describe the tip as having multiple small cusps close to the tip apex, as a consequence several local hot spots will be created on those cusps. This will cause the temperature of the tip apex to increase and when the applied field exceeds 23.8 V/nm the cation Au^+ will be field evaporated, Fig. 2.9(b). In this case there is important heating of the sample, since the electron current when the field exceeds 6 V/nm is significant. When negative field is applied intense heating of the tip apex is expected since the field gradient lines are very dense on the tip apex. Field-gradient-induced surface diffusion of negative ions is very efficient in this case. This will produce a flow of atoms from the tip shank to the apex creating a protrusion as seen in Fig. 2.9(d). When the field is close to 11 V/nm field evaporation of the anion Au^{2-} will occur.

2.2.3 Point Contact

Figure 2.10 depicts the deposition process in the Point Contact case. First the tip is positioned very close to the surface (distance of 0.6 nm or less) Fig. 2.10(a), then a rather large voltage pulse is applied and a point contact is established as seen in

Fig. 2.10(b), once the contact is made a field induced migration of atoms from the shank toward the tip apex, following the field gradient, takes place forming a liquid-metal-neck between tip apex and sample surface. As the feedback control retracts the tip this neck is elongated, as seen in Fig. 2.10(c), forming a nanobridge which is subsequently broken and a relatively big mound is left deposited on the surface, Fig. 2.10(d). How the point contact is established may differ within the available literature. Two common explanations are: mechanical contact after voltage pulse application, an electron current heats up or even melts the tip which forms liquid-metal neck as argued in early investigations [35], [64], or by the creation of a cone or protrusion on the tip apex, produced by the hydrodynamic flow of atoms, while in very close proximity, that then make contact with the surface [33], [36], [65], [66], [67]. Hoel and co-workers coined the term Field Induced Deposition FID for this later explanation of the process. Is important to mention that owed to the proximity of tip and sample the field gradient lines for positive or negative field are essentially the same. So this FID process is independent of tip polarity.

Later in Chapter 4 we will show arguments to discard this mechanism of deposition for our system. In section 4.3 we will use equations 2.24 and 2.27 to fit experimental data obtained during depositions events. It will allow us to to have a physical understanding of the role that the tip geometry plays in defining the electric field at tip apex.

3

Nanodots fabrication: setup & methods

3.1 Tip-sample separation control

3.1.1 Introduction of an electrostatic force term

For depositing a nanodot using the process developed in this work, a potential difference needs to be established between tip and sample to define and control the tip-sample distance. This method is implemented by exploiting some observations made by Dianoux and co-workers [55], [68]. As described in in these references, Dianoux *et al.* used an AFM for measuring electrostatic forces caused by buried charges on a surface, at a constant tip-sample distance, and while a V_{bias} is applied to the tip, the phase data is recorded. Measured electrostatic forces where studied by its effects on the evolution of the tip motion (oscillation amplitude and phase shift) by studying changes on the force-distance curves (amplitude vs. tip-sample separation and phase vs. tip-sample separation). For interpreting the obtained data, they used and modified the analytical formalism developed by Aimé *et al.* [56], [57], by adding an electrostatic term to the van der Waals force coupling strength k_{vdW}. This electrostatic force is essentially the force between the plates of a capacitor (the tip and the sample) in the presence of an applied bias V_{bias}. Now, the interaction potential between tip and sample U_{ts} on the Lagrangian defined on Eq. 2.16 needs to be modified to account for the new long-range monotonic interaction force. At this stage, modeling of the electrostatic interaction of our cantilever-tip and sample system is necessary. A practical way to do this, is to consider the tip-sample system as an axially symmetric capacitor, then the electrostatic interaction can be described by

the relation :

$$F_{elec} = -\frac{1}{2}\frac{\partial C}{\partial z}V_{bias}^2, \tag{3.1}$$

in which $C(z)$ is the distance dependent capacitance of the tip-sample configuration. For analytical convenience we will assume a parallel plates capacitor model. As a first approximation a plane-plane capacitor model for our tip-sample system may be seen as too inaccurate. Later on, we will discuss under which conditions this rough approximation works. For a plane-plane capacitor the electrostatic interaction potential between tip and sample is expressed by:

$$U_{elec} = \frac{1}{2}C_{p-p}V_{bias}^2 = \frac{1}{2}\frac{\epsilon_0 S_{eff}}{z}V_{bias}^2, \tag{3.2}$$

where S_{eff} is the *'effective area'* of the tip and ϵ_0 is the dielectric constant. The new total tip-sample interaction potential is given by:

$$U_{ts} = U_{vdW} + U_{elec} = \frac{A_H R}{6d} + \frac{1}{2}\frac{\epsilon_0 S_{eff}}{d}V_{bias}^2 = \left(\frac{A_H R}{6} + \frac{1}{2}\epsilon_0 S_{eff}V_{bias}^2\right)\frac{1}{d}. \tag{3.3}$$

Notice that this modified total interaction potential retains the same dependence on the vertical direction and then it can be used to solve the nonperturbative analytical treatment as developed by Aimé *et al.*, the new modified expressions for the force-distance curves, equations 2.19 and 2.20 are given by:

$$d_{A\pm} = \sqrt{a^2 + \left(2\frac{k_{vdW} + k_{elec}V_{bias}^2}{(1-u^2) \mp \frac{1}{Q}\sqrt{\frac{1}{a^2} - u^2}}\right)^{\frac{2}{3}}}, \tag{3.4}$$

and

$$\phi_{A\pm} = arctan\left(\frac{u}{Q(u^2-1) + 2Q\frac{k_{vdW}+k_{elec}V_{bias}^2}{(d_{A\pm}^2 - a^2)^{\frac{3}{2}}}}\right), \tag{3.5}$$

where we use the same notation as before for the reduced variables, and d, as usual is the tip-sample separation, and the dimensionless electrical coupling strength is given by:

$$k_{elec}V_{bias}^2 = \frac{\epsilon_0 S_{eff}}{2kA_0^3}V_{bias}^2. \tag{3.6}$$

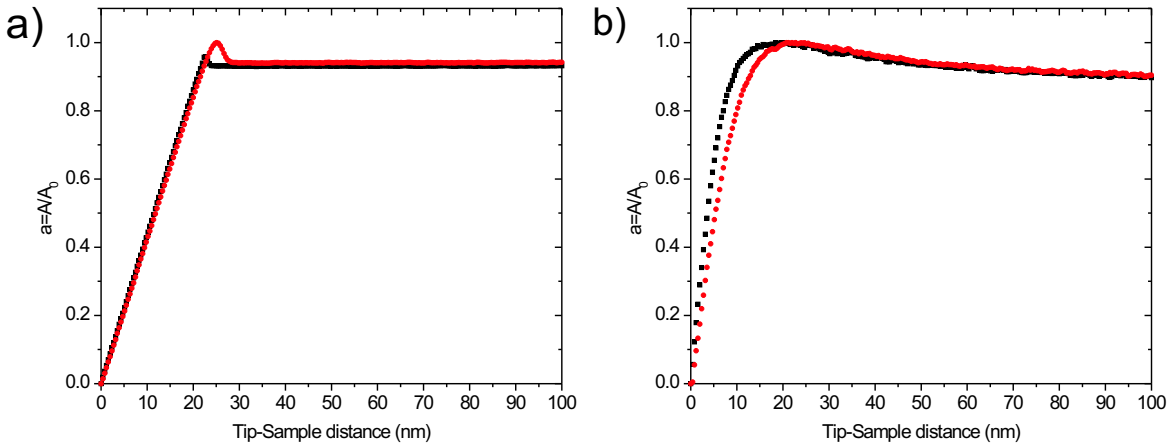

Figure 3.1: Experimental force-distance curves: Reduced oscillation amplitude a vs. tip-sample distance. a) Intermittent contact operation mode, b) For $V_{bias} \approx 6\ V$ and higher biases, the tip is in a non-contact mode regime. The curves in black are taken while the tip is approaching the sample, and in the red curves the tip is being retracted by the Z-piezo. Experimental parameters are: the amplitude setpoint is $a = 0.95$, the free oscillation amplitude is $A_0 = 6\ nm$, and the reduced frequency is $u = 0.9988$. These values correspond to typical experimental conditions. The hysteresis in a) are owed to non-linearities of the force-distance equations.

Either the oscillation amplitude A or the phase shift ϕ may be used to monitor the changes in the force-distance curves. From now on we will only concentrate in the oscillation amplitude as the parameter to monitor and control. In the lab, this curves are measured by turning off the feedback loop and stopping the scan while up and down voltage ramps are applied to the Z-piezo. By doing this the cantilever-tip, which is excited close to its resonance frequency, is being approached and retracted from the sample and changes in the dynamics of the oscillation are recorded. By monitoring the oscillation amplitude we construct the experimental force-distance curves that are shown in Fig. 3.1, where the reduced oscillation amplitude $a = A/A_0$ is plotted against the tip-sample separation.

The hysteretic behavior of the curves in Fig. 3.1 a) corresponds to non-linearities that are present in Eq. 3.4 and is evidence of a repulsion interactions regime between tip and sample which is characteristic of an intermittent (IC) contact operation mode [57]. On the other hand, in Fig. 3.1 b) when an electrostatic force is introduced

by applying V_{bias}, Eq. 3.1, the hysteresis is not present anymore, which means that the attractive regime dominates the tip-sample interaction and that we are operating in a non-contact (NC) mode. The process in completely reversible, and can be repeated as many times as needed. The oscillation amplitude setpoint can be appreciated in the flat regions of the curves, when the tip is far from the sample.

3.1.2 Tip shape & Capacitance

Our ability to construct theoretical force-distance curves using Eq. 3.4, and being able to develop a reliable tip-sample separation control method will depend on the modeling of the tip-sample configuration capacitance $C(z)$. As we will see, this mean as well to be able to calculate an appropriate plate effective area S_{eff}. Actually, as mentioned in section 2.1.3, the tip oscillation is sensitive to the gradient of force $\frac{\partial F}{\partial z}$, which means that we need to look for expressions for the second derivative of $C(z)$.

To obtain an expression for the capacitance of the system tip-sample, and its second derivative, we must first model the tip shape and the geometry of the system configuration. Here we use some common simplifications: the models assume that all the surfaces are metallic and border effects are neglected, the sample surface is replaced by an infinite plane, is one of the capacitor plate's, and the tip is approximated by

- A plane plate or disk with surface S, the gradient is given by the expression:

$$\frac{\partial C_{p-p}(z)}{\partial z} = -\epsilon_0 \frac{S}{z^2}, \tag{3.7}$$

- A sphere of radius R, an expression for the first derivative from ref. [69]:

$$\frac{\partial C_{s-p}(z)}{\partial z} = 4\pi\epsilon_0 \sum_{n=1}^{\infty} \frac{coth\ \alpha - n\ coth\ n\alpha}{sinh\ n\alpha}, \tag{3.8}$$

$$\text{where } cosh\ \alpha = 1 + \tfrac{z}{R},$$

- A cone which has a half cone angle of θ_0, and height h. An expression for the capacitive gradient is given by [69]:

$$\frac{\partial C_{c-p}(z)}{\partial z} = 2\pi\epsilon_0 K^2 ln\left(\frac{h}{z}\right), \tag{3.9}$$

where $K^2 = \frac{1}{[ln\ cot(\theta_0/2)]^2}$.

Calculating the second derivative of $C(z)$ is straightforward for equations 3.7 and 3.9, their expressions is given by:

$$\frac{\partial^2 C_{p-p}(z)}{\partial z^2} = 2\epsilon_0 \frac{S}{z^3}, \tag{3.10}$$

and

$$\frac{\partial^2 C_{c-p}(z)}{\partial z^2} = 2\pi\epsilon_0 \frac{K^2}{z}. \tag{3.11}$$

In the case of $C_{s-p}(z)$, Eq. 3.8, we need to make approximations for two cases:

- For $z << R$, at this limit Eq. 3.8 becomes:

$$\frac{\partial C_{s-p}(z)}{\partial z} = -2\pi\epsilon_0 \frac{R}{z}, \tag{3.12}$$

  and consequently

$$\frac{\partial^2 C_{s-p}(z)}{\partial z^2} = 2\pi\epsilon_0 \frac{R}{z^2}. \tag{3.13}$$

- When $z >> R$, at this limit, a series expansion of Eq. 3.8 is given by:

$$\frac{\partial C_{s-p}(z)}{\partial z} = -2\pi\epsilon_0 \left\{ \left(\frac{R}{z}\right)^2 + \left(\frac{R}{z}\right)^3 + ... \right\}, \tag{3.14}$$

  and the second derivative for the capacitance is:

$$\frac{\partial^2 C_{s-p}(z)}{\partial z^2} = \frac{2\pi\epsilon_0}{z} \left\{ 2\left(\frac{R}{z}\right)^2 + 3\left(\frac{R}{z}\right)^3 + ... \right\}. \tag{3.15}$$

In Fig. 3.2 we plot the second derivative of $C(z)$ vs. the tip-sample separation for C_{p-p}, C_{s-p}, and C_{c-p}. We have used typical experimental values for the tip geometry parameters R, h, θ_0, and average tip-sample separation D, refer to Fig. 3.2 caption for details. For $D = 10\ nm$, which is representative of our working separation distance, we adjusted S_{eff} so the C_{p-p} and C_{s-p} models give the same values for the second derivative of the capacitance:

$$\frac{\partial^2 C_{p-p}(z)}{\partial z^2}|_{z=D} = \frac{\partial^2 C_{s-p}(z)}{\partial z^2}|_{z=D}, \tag{3.16}$$

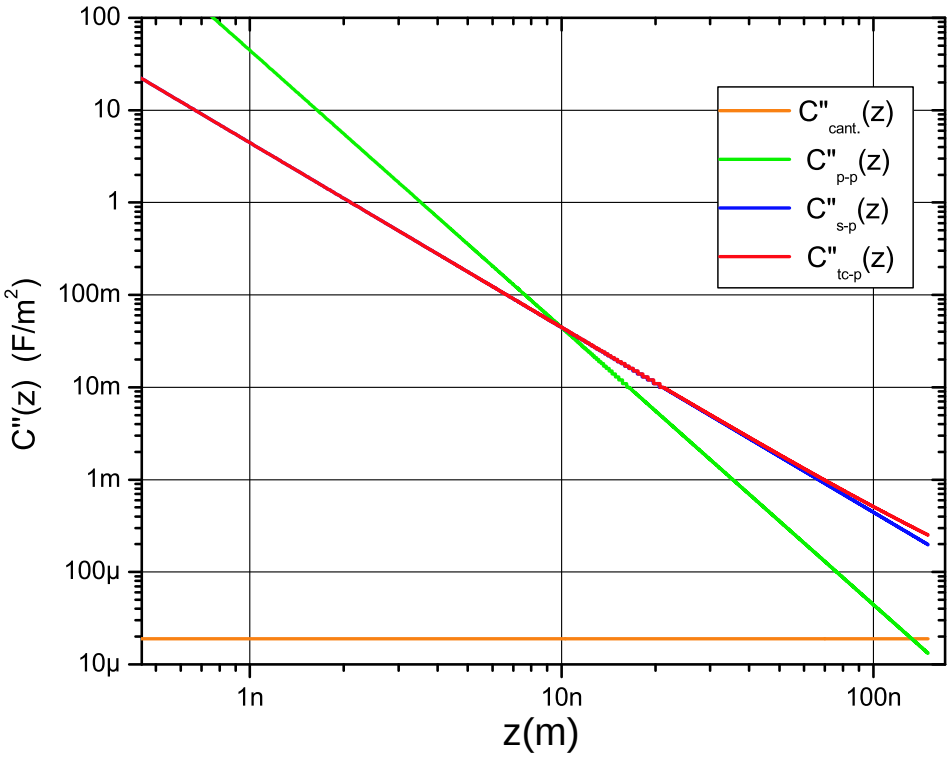

Figure 3.2: Calculated second derivative of the capacitance vs. tip-sample separation. The tip radius is 80 nm, the average tip-sample separation is 10 nm, and $S_{eff} = 2513\ nm^2$. Cantilever dimensions: $w = 38\ \mu m$, $L = 225\ \mu m$, and $h = 20\ \mu m$.

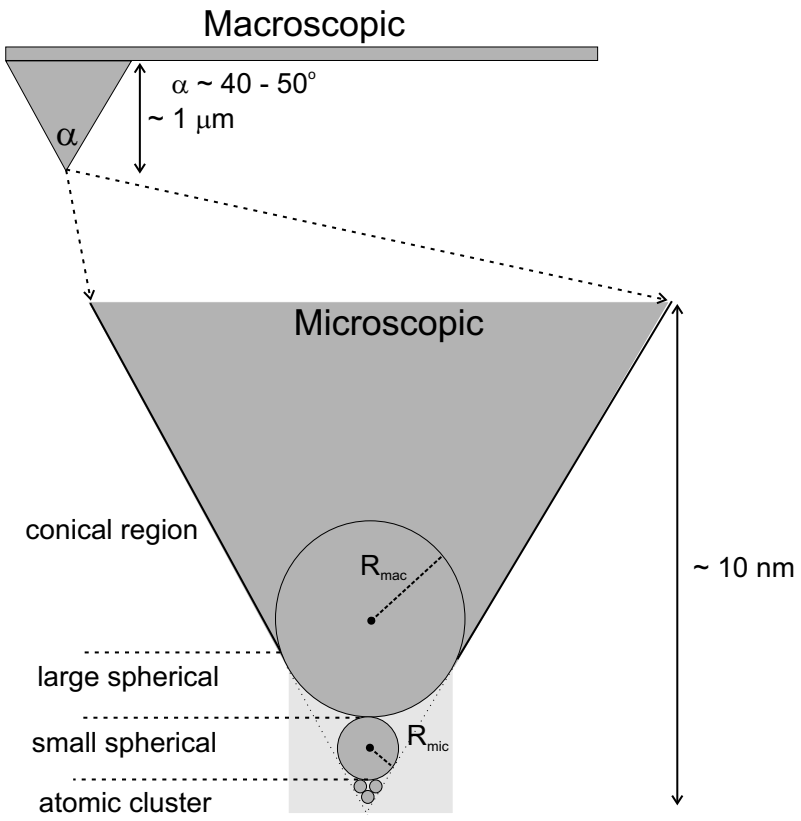

Figure 3.3: Relevant dimensional scales and the tip configuration geometry model. The sample surface is always modeled as a one plane plate. Adapted from ref. [51].

as can be seen in Fig. 3.2 the curves intersect at $z = D$. Using equations 3.10 and 3.13, we obtain an expression for effective surface given by:

$$S_{eff} = \pi RD. \tag{3.17}$$

Notice that this equation is only valid when $z << R$. At this tip-sample separation and with a tip radius of 80 nm, $S_{eff} \approx 2513\ nm^2$ which corresponds to a disc of 56 nm diameter or a plate with dimensions $50 \times 50\ nm^2$, which is reasonable for the dimensions of our tip, and indicates that there is some contribution from other parts of the tip more than the apex. We have also plotted in figure 3.2 the contribution of the cantilever, C_{cant}, modeled as a plane-plane capacitor with a plate area of $w \times L$ separated $h + D \approx h$ from the surface. As can be appreciated, this contribution is negligible.

How valid is the use of a plane-plane capacitor for the tip-sample system? It

depends on how we choose the capacitor plate area S_{eff}. We need to calculate the capacitance with a more realistic model so it does reflect the actual geometry of the tip-sample system. The value of this capacitance is calculated at a tip-sample separation of d and then is equated to the capacitance of a plane-plane capacitor, in which the plates are separated a distance d, by adjusting the effective area S_{eff}. This method is used by Hudlet *et al.* [70]; in this reference they evaluate the capacitance of a tip modeled as a sphere truncated cone by dividing the tip into infinitesimal facets and calculating the capacitance of each of the facets and the sample surface, both modeled infinite planes with the same relative orientation, and a superposition of all the individual contributions. They also showed how the tip-sample separation d determines what part of the tip contributes mainly with the total capacitive gradient. For short distances, tip close to the surface, at this limit the model reproduce the sphere-plane geometry, the apex radius controls the contribution; at larger distances, the tip dimensions, θ_0 and h, the shank of the tip, becomes the most important contributor. This height dependent contribution to the capacitance of different parts of the tip, apex and shank, is reflected in the total value of the effective surface area S_{eff} that interacts electrostatically with the sample surface. In Fig. 3.3 we summarize this observations. The matter of fact is that all of the tip, macro-micro, can interact with the sample. In the case of our experiment, given that when depositions are performed we use approximately the same conditions: small oscillation amplitudes (from 7 to 10 nm), tip-sample separations d between 3 to 5 nm and tip radii that average 60 nm our tip-sample configuration geometry is practically fixed. Also, since we are are relaying on a long range monotonic electrostatic force during depositions, as we will soon see, the operation of the microscope is very stable while in non-contact mode. So for the settings at which we operate, the sphere-plane model is just a good approximation. Later, in section 4.4 of the next chapter we will see that an extra modification is needed to explain high evaporation rates and that a protrusion with R_{mic} will be needed to further understand the electric field at the tip apex.

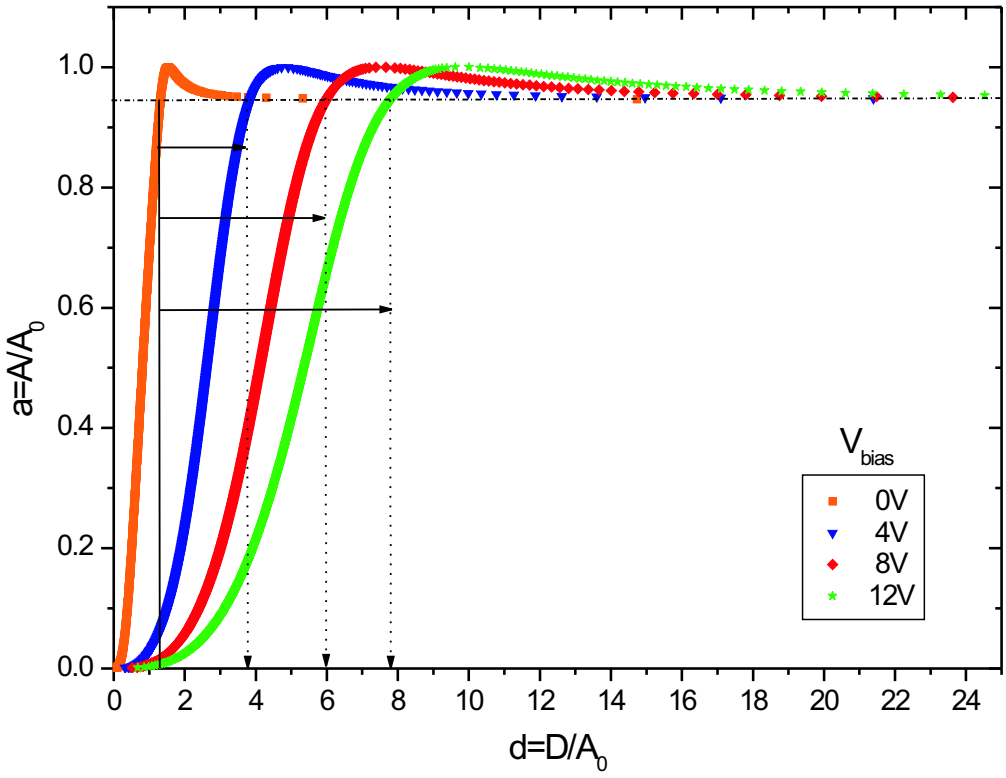

Figure 3.4: Calculated force-distance curves of the reduced amplitude a against the reduced tip-sample separation d with electrostatic coupling. The parameters used are: reduced frequency $u = 0.9988$, free amplitude $A_0 = 6\ nm$, $Q = 850$, $k = 40\ n/m$, $S_{eff} = 2513\ nm^2$, $k_{elec} = (1.287 \times 10^{-3}/V^2)V_{bias}^2$, and $k_{vdW} = 3.086 \times 10^{-4}$. These parameters correspond to typical experimental conditions. The horizontal dashed line corresponds to the experimental amplitude setpoint $a = 0.95$.

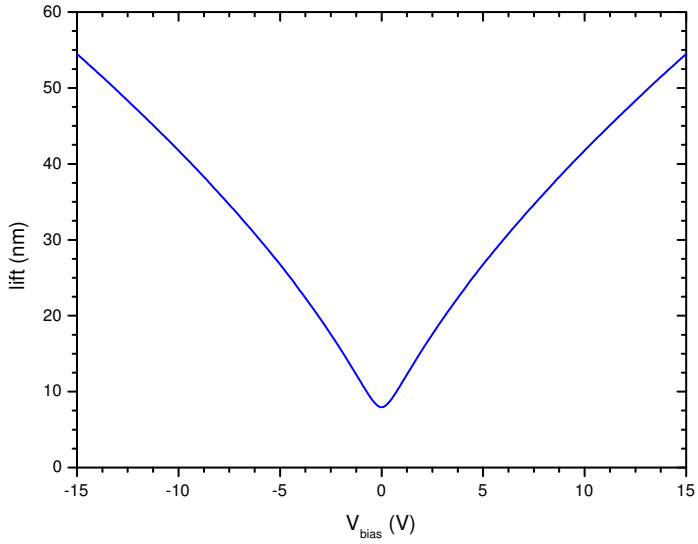

Figure 3.5: Theoretical plot of the lift height D vs. the applied bias V_{bias}. Amplitude setpoint is $a = 0.95$.

3.1.3 Construction of d vs. V_{bias} curves

With the obtained value for the effective surface area S_{eff}, we can calculate the value of the electrical coupling strength k_{elec} from Eq. 3.6 and plot the reduced oscillation amplitude a vs. the reduced tip-sample separation d for different biases V_{bias} using Eq. 3.4. In Fig. 3.4 a) we show this plot with V_{bias}= 0 V, 4 V, 8 V, and 12 V. An immediate effect of applying the bias is that the curves shift right from the one with no bias applied. Bigger applied biases produces a bigger shift. Since the servo of the microscope is keeping the interaction constant the addition of an electrostatic force will cause an increment of the tip-sample separation. This way for a bias of V_{bias}= 8 V the piezo retracts the sample by 6 nm. If we compare the calculated force-distance curves with the experimental ones shown in Fig. 3.1, our assumptions for the modeling of the tip-sample interaction works quite well despite the use of a simple parallel plates capacitor on Eq. 3.2.

The lift height dependence on V_{bias} can be better noted by graphing again Eq. 3.4 but this time we plot d vs. V_{bias} as can be seen in Fig. 3.5. Here we use the same

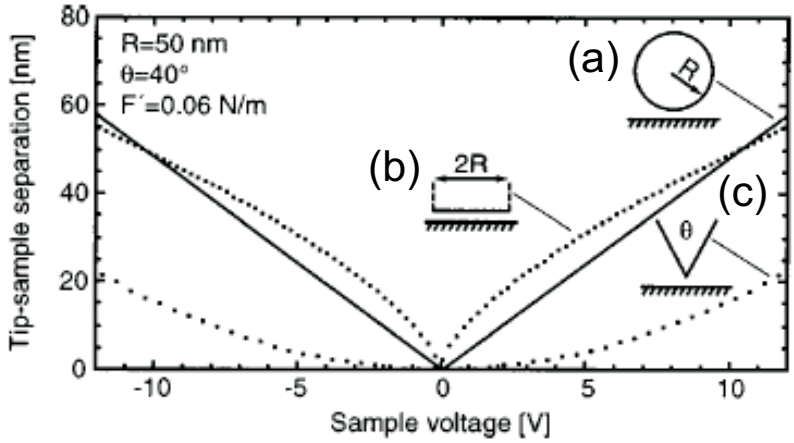

Figure 3.6: Lift vs. applied bias by keeping the interaction (force gradient) constant for three different models for the geometry of the tip-sample system. (a) For a sphere-plane: $D|_{F'=const} = \left(\frac{\pi\epsilon_0 R}{F'}\right)^{\frac{1}{2}} V_{bias}$, the shape is linear, (b) For a plane surface or disk: $D|_{F'=const} = \left(\frac{\pi\epsilon_0 R^2}{F'}\right)^{\frac{1}{3}} V_{bias}^{2/3}$, same shape as in Fig. 3.5, and (c) For a cone: $D|_{F'=const} = \left(\frac{\pi\epsilon_0 K^2}{F'}\right) V_{bias}^2$, the shape is parabolic. Adapted from Ref. [71].

operational amplitude setpoint of $a = 0.95$; this value corresponds to experimental conditions and all other parameters are the same as the ones specified in the caption of Fig. 3.4. So by applying a V_{bias} we can precisely dynamically control the separation between tip and sample. This plot visualizes quantitatively how we can define the lift height by selecting a suitable V_{bias}.

In the lab we construct a d vs. V_{bias} calibration curve similar to one of the branches in Fig. 3.5 (only for positive biases) and from it we 'dial' the desired value for tip-sample separation[1]. Nevertheless, we routinely obtain a straight line (as best fit to our data) which differ with the shape of the curve on Fig. 3.5. Actually, the shape of the curve on that figure corresponds to a tip modeled as a parallel plates capacitor, which is expected given our approximation. A linear relationship between D and V_{bias} implies that the sphere-plane model is contributing the most to the total capacitance, at this tip-sample separation and $D << R$ [72]. This is revealed too by Fig. 3.6 which is adapted from Olsson's *et al.* [71]. As we will see in the next chapter for our typical distance to radius ratio d/R the particular details of the geometrical

[1]In section 3.3 we give a detailed explanation on how this graph is constructed in the lab.

model becomes irrelevant for the calculation of the electric field at the tip apex. All models, the ones discussed in previous sections, behave approximately linear.

3.2 Instrumentation

In Fig. 3.7 we show the schematic for the nanodot fabrication process, including the microscope, data acquisition, and the circuitry for pulse application and tip lifting. We will go through these components one by one.

3.2.1 The microscope

Experiments implemented for this work were performed with a scanning probe microscope by Digital Instruments[2], a MultiMode^{TM} with the NanoScope^{TM} IIIa controller, and an Extender^{TM} electronics module, which provides phase and frequency detection. The microscope is equipped with a tube scanner AS-12(E) which has a lateral (X-Y) maximum range of $10\mu m \times 10\mu m$ and a maximum vertical range of 2.5 μm. It sits on an optical table over a vibration isolating pad.[3] This microscope is configured so that the sample-substrate sits on the top of the piezo tube scanner on a metallic, and magnetic, piezo cap. This piezo cap is also electrically isolated and can be used for biasing the sample. The cantilever-tip chip is placed onto a clip holder: it sits over the bimorph and is firmly held in place by a copper-beryllium spring which contacts the tip side of the cantilever and is used to electrically contact it. This holder is provided with electrical connectors for the piezos on the bimorph and an electrical contact to the tip side of the cantilever. When properly placed in position the inclination angle of the cantilever-tip is close to 11°. The clip sits on the head of the microscope where all the optical components (laser diode, quad-photodetector, and mirror) for the beam-deflection sensor are located. The head is fixed onto the microscope base with a couple of springs which hold it against three micrometric screws, one of them motorized, and are used for the engagement of the tip and sample.

[2]Now part of Veeco Metrology Group.

[3]The quoted specification for noise is less than 0.3Å RMS in the vertical dimension when using the vibration isolation silicone pad and acoustic cover hood.

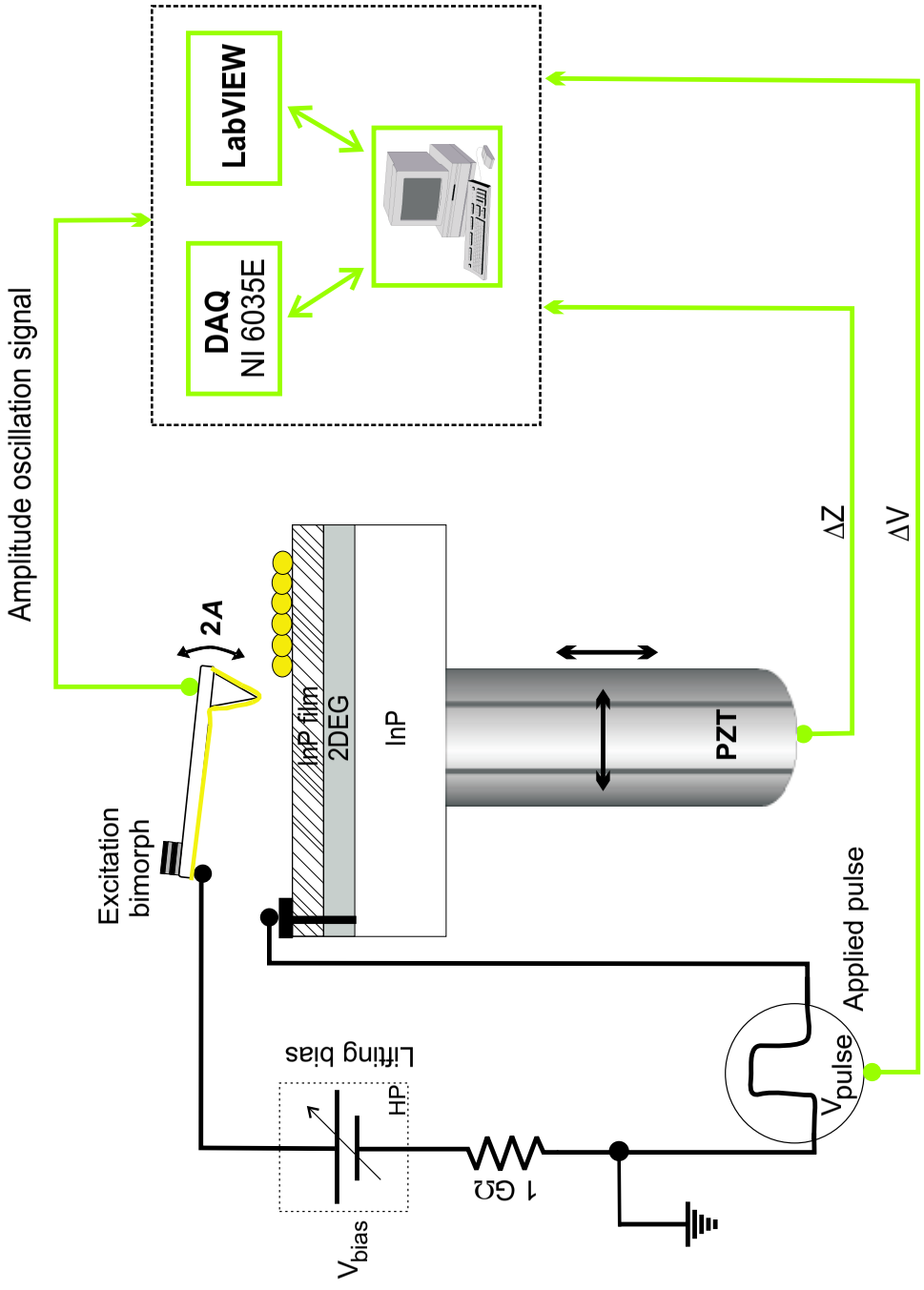

Figure 3.7: Schematic of the experimental setup.

3.2.2 Cantilever tip preparation

We already discussed some important considerations regarding the relative values for the spring constant k and resonant frequency f_0; together with the quality factor Q these are the more important properties to consider when choosing cantilever-tips for designing an experiment.

In table 3.1 we list the specifications for cantilevers-tips used for the implementation of this work. The NanoSensors[4] cantilever tip is shown in Fig. 2.2 b). The primary consideration for choosing these tips is their high stiffness. Floppy cantilevers are inappropriate for this experiments since they easily snap onto the surface when a V_{pulse} is applied. In order to field evaporate a metal from the cantilever-tip or to

Table 3.1: Cantilever tip specifications

Tip manufacturer	k $[N/m]$ (nominal)	f_0 $[kHz]$ (nominal)	Tip height $[\mu m]$	Half cone angle	Tip radius $[nm]$
μMasch UltraSharp	40	170	15-20	15°	< 10
NanoSensors PointProbe	48	190	10 - 15	$< 10°$	< 7

have a probe that can sense electrostatic interactions it is necessary to metalize the tip. We use thermal evaporation to coat a Ti adhesion layer followed by a Au coating onto the cantilevers. These layers were deposited using an evaporator by Thermionics Lab. VE-90 system. Ultimate vacuum on the evaporation chamber is in the low 10^{-7} torr's range. A quartz crystal microbalance is used for measuring the rate and the final thickness of the evaporated materials. The cantilever chips, with the tips facing the evaporation sources, are placed on a sample holder without any cleaning processing as provided by the manufacturer. Au and Ti pellets with a purity of 99.9% (Angstrom Sciences) and 99.995% (Puratronic, Alfa Aesar) respectively where used. First the Ti adhesion layer is deposited at a rate of 0.4 Å/s to a total thickness of

[4]NanoSensors GmbH, http://www.nanosensors.com.

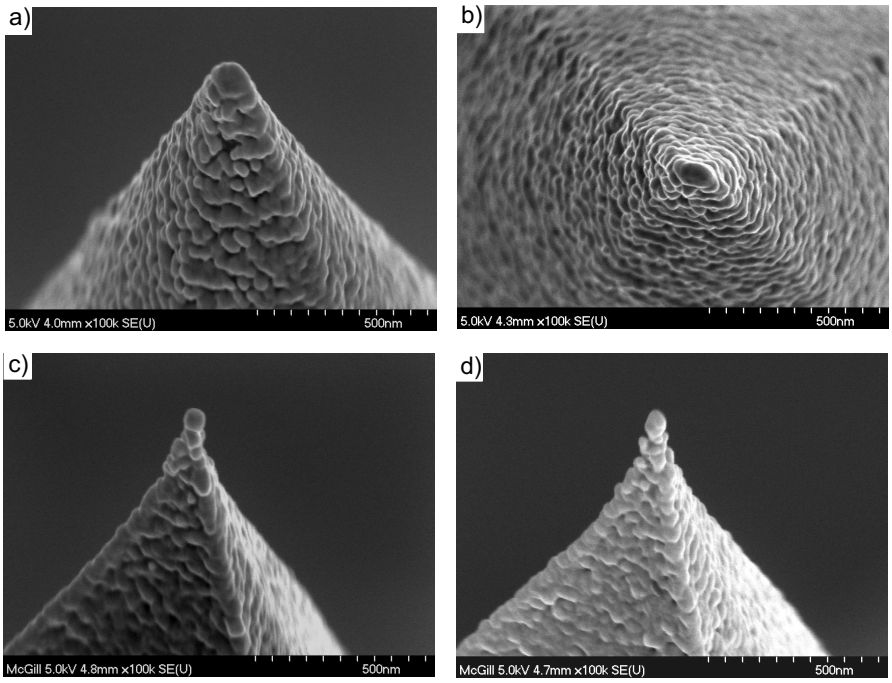

Figure 3.8: FE-SEM images of silicon cantilever tips with a 100 nm/10 nm Au/Ti evaporated coating: a), b) MikroMasch cantilever-tips, two different view angles of the same tip, a) 22◦ side view, b) top view. c), d) NanoSensors cantilever-tips, two different tips coated in the same batch, both images 22◦ side view. In all images the cantilever is on the right of each tip.

10 nm and it is immediately followed by a 100 nm thick layer of Au deposited at a rate of 1.4 Å/s. Pressure of the chamber during Ti evaporation is 2×10^{-7} torr and for the Au is 1×10^{-6} torr. The samples are rotated during the evaporation to ensure uniformity of the deposited film and to avoid shadowing effects. Evaporation rates and thicknesses were chosen taking into account the possible bending or deformation of the cantilever beam due to high temperatures or stress caused by the deposited film. The final temperature on the sample holder plate when the Au evaporation is completed is approximately 150° C, which did not cause any apparent change on the cantilevers. Cantilevers were only taken out of the chamber when the temperature inside it dropped to room temperature.

After processing, characterization of the coated cantilever tips was performed with an FE-SEM. Particular attention was given to the after-coating radii of the tips and the conformality of the Au film on the tip faces. In Fig. 3.8 we show SEM scans of

cantilever tips that have been coated with Au and Ti by using the method previously described. The specifications for these tips are shown on table 3.1. The coating at the tip apexes seems to form a continuous granular film with relatively large and not too closely packed grains. The diameter of the grains is approximately $25 - 50\ nm$. Tips radii at the apex is a few grains wide and it seems to correspond with the original pre-coating radius for those tips. For the MikroMasch cantilevers tips, like the ones show in Fig. 3.8 a), and b) the diameter is usually 80 to 150 nm. The NanoSensors ones, see Fig. 3.8 c), and d) were consistently sharper with diameters in the $50 - 75\ nm$ range. At the end of this chapter we will show how mechanical wear and electrical stress affects reliability of the coating.

3.2.3 Applied pulse and tip lifting bias

In section 2.2.2 we mention how central to FED the application of an electric field between tip and sample is, and how the polarity of this field selects the directionality of the mass transfer. At the same time the ability to control tip-sample separation with precision is essential for the precise definition of this electric field and to avoid tip contact to the sample. These two are central to the technique developed for the realization of this work and have important impact on the overall reliability of the FED deposition process.

To control the tip-sample separation we rely, as mentioned before, on the establishment of a long range monotonic electrostatic force by applying an external DC voltage difference V_{bias} between tip and sample. We use a HP E3631A DC power supply for biasing the tip with small positive or negative voltages.

For creating an electric field pulse for FED in the tip-sample gap we applied a voltage pulse of duration Δt and amplitude V_{pulse}. For this purpose we use a Interstate Function Generator F74 coupled to a Tektronix AM501 operational amplifier. The minimum and maximum Δt are 1 μs and 10 ms respectively. The pulse amplitude can be increased up to $\pm 45\ V$ with the op. amp. in place. In Fig. 3.9 we schematized the relations between V_{pulse} and V_{bias} to define the total voltage on the gap $\Delta V = V_{\text{tip}} - V_{\text{sample}}$ and the polarity of the tip. As can be noted in Fig. 3.7 we connect the

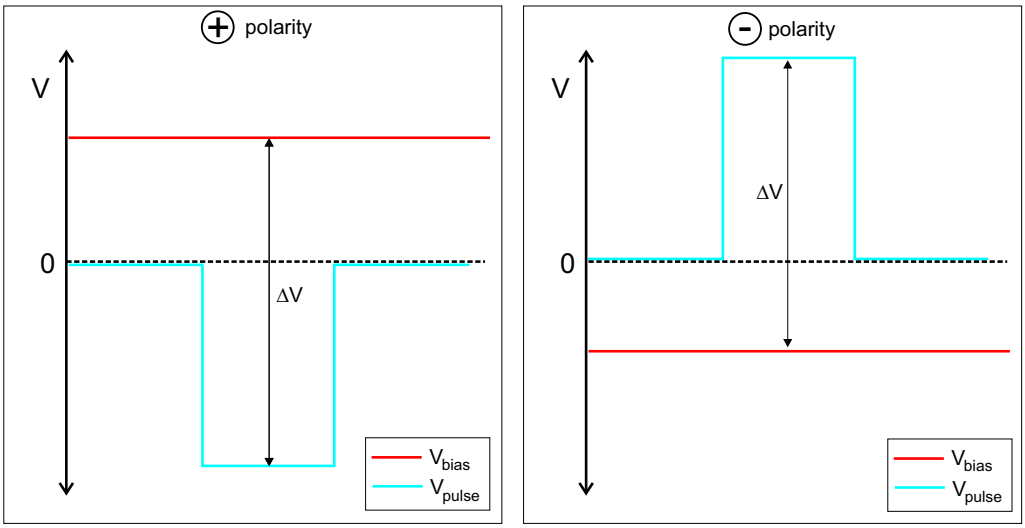

Figure 3.9: Tip polarity. V_{bias} and V_{pulse} are always applied to the tip and sample respectively.

V_{bias} always to the tip and the V_{pulse} always to the sample. Even though some other configurations are possible this one results in being the one with the lesser parasitic capacitance effects on our applied pulse. The shunt resistor is put in place for limiting the current flow in case of tip-sample contact. Due to the proximity of the tip and the sample, and tip sharpness the electric field is very intense. This creates a very large current density even for small biases. In the last section we will see the effects of high current densities on the metal coating of the tips.

3.2.4 Data acquisition

For defining and controlling the tip-sample separation, for measuring the dynamics of the cantilever in real-time, and applying the lifting bias and V_{pulse} a set of signals need to be monitored and recorded, for this purpose a dedicated data acquisition system was implemented. As provided by the manufacturer the controller and the extender module are 'black boxes': for access or interruption of signals between the microscope and the extender/controller we use a Signal Access Module$^{\text{TM}}$ (SAM). Extra signal inputs, like bias to the tip or to the piezo cap, were provided through jumpers pins located on one of the printed boards located on the microscope base. These jumpers are accessible from the bottom of the base. For data acquisition we

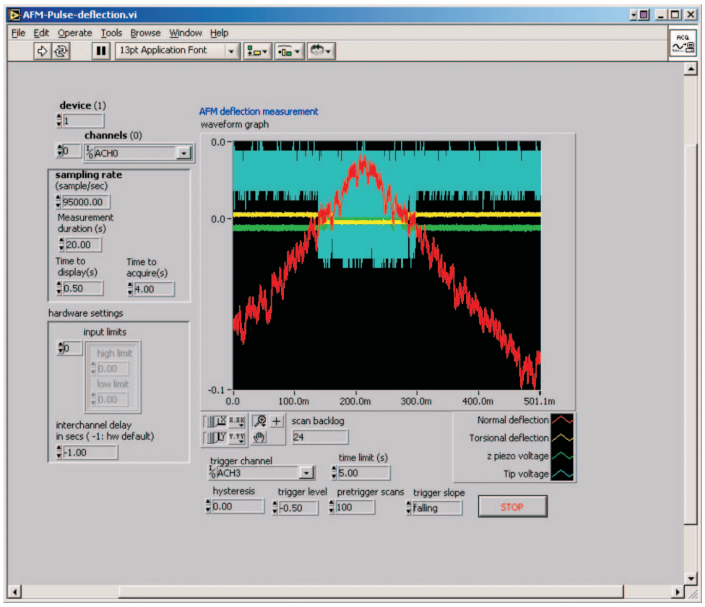

Figure 3.10: LabVIEW application interface for data acquisition.

complemented the SAM with a National Instruments DAQ PCI-6035E board and a BNC-2090 rack-mount analog breakout box. This DAQ has a 200 kHz sampling rate with a 16 bits resolution. Monitored signals included the photodiode RMS signal (In 0), the vertical deflection (Aux A), the Z-piezo voltage, and the applied voltage pulse V_{pulse} and V_{bias}. For measurement and control we developed a NI LabVIEW application which allows us to monitor the signals in real time. A screen shot of the front panel of this application is shown in Fig. 3.10. In it we control the sampling rate, the measurement duration time and how much of it will be acquired and recorded on a file. Data acquisition is triggered by the first pulse applied.

3.3 Deposition procedure

The developed procedure for dot deposition using a NC-AM-AFM has several steps and can be resumed as shown in Fig. 3.11. The procedure for depositing can be separated in the following four steps:

- First, we operate the microscope on intermittent contact IC mode to capture a topographic image of the surface and to select where the deposition will be

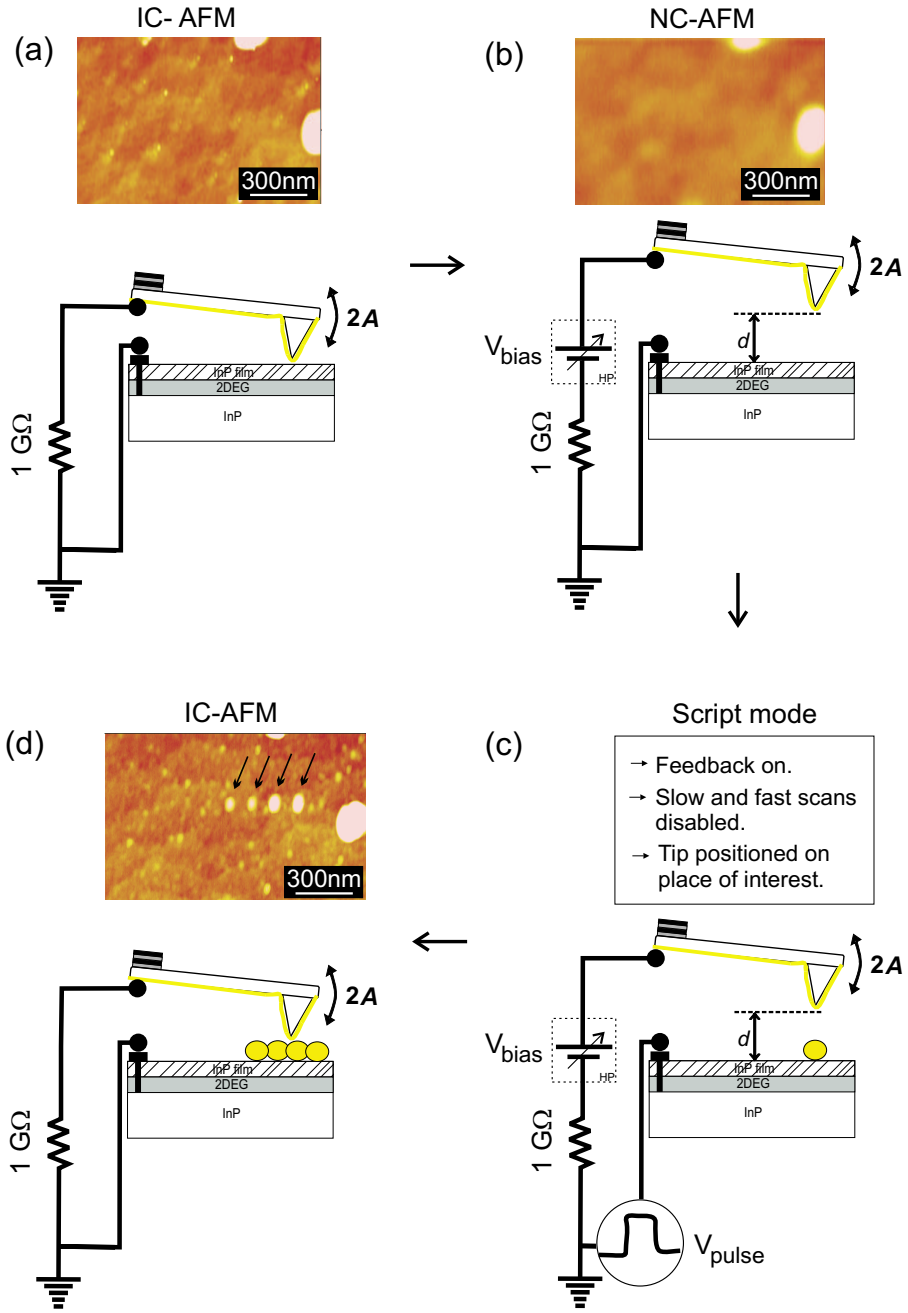

Figure 3.11: Gold Deposition using an AFM. a) Imaging the area of interest. b) V_{bias} is applied, tip-sample average separation increased to d. A non contact image is taken. c) Deposition script is running: tip translated to position of interest, V_{pulse} is applied. d) Imaging the same area after deposition, four pulses applied on C), four nanodots deposited.

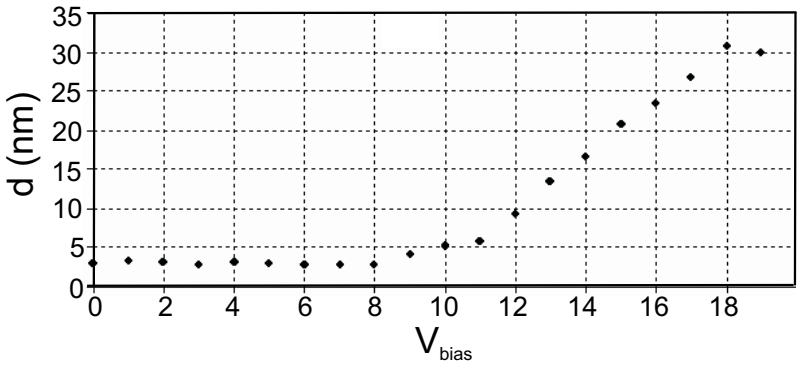

Figure 3.12: Experimental lift height vs. applied bias. Only after $V_{bias} \approx 8\ V$ the tip is in the non-contact regime. The experimental parameters are: $Ao = 7.5\ nm$, $u = 1.000$, and $a = 0.95$.

performed. Usually, a fairly flat region of the surface is chosen, see Fig. 3.11 a). At this stage, tip and sample are kept electrically grounded. Next, we generate an amplitude-distance curve: the (X, Y) scan is stopped and a triangular ramp is applied to the Z-piezo. This is done to set up new values for the free oscillation amplitude A_0 and the amplitude setpoint in preparation for changing to non-contact operating mode. The new oscillation amplitude is usually set to 6 nm p-p and the reduced amplitude a ($a = A/A_0$) is set to 0.95. In comparison, while in intermittent contact A_0 is approximately hundred of nanometers and the amplitude setpoint is set to approximately the 80% of this free value. This higher value for the intermittent contact mode is common since the tip has to probe short and long range interactions in one oscilation cycle. Also to make sure that the tip gets beyond the range of any adhesion or capillary forces.

- After fixing the oscillation amplitude, in order to lift the tip several V_{bias} are applied to the tip while force-distance curves are measured. For increasing values of V_{bias} the force-distance curves are shifted to the right, as depicted in Fig. 3.4. As the Z-piezo retracts which every applied V_{bias} we measure the amount of shift, the tip-lift height, between the force-distance curve with $V_{bias} = 0\ V$ and every shifted force-distance curve. In Fig. 3.12 we show a plot of the lift-height vs. V_{bias} As mention before, for small tip-lift heights, about 2 to 10 nm, the data points in the graph seems to follow a line. A linear fit is

usually performed to the data points and a calibration slope is obtained for this particular tip-sample combination. Then, when the tip-lift height calibration is done, one can set V_{bias} accordingly with the desired tip-lift height. This value change from tip to tip, and is usually between 1 to 6 V for $d = 6\ nm$. The tip-lift height is kept constant by the feedback loop of the microscope. The zero or origin of the tip sample-distance is the Z-piezo position where repulsive and attractive forces are the same and can be measured from the deflection vs. Z-piezo displacement curve as displayed by the NanoScope software.

Once the lift is set and we return to normal imaging conditions, a new image of the surface is taken, see Fig. 3.11 b). This new image lacks topographic details as the tip is now oscillating at a small amplitude and hovering off the surface at a distance d. This evidence that we are now operating in non-contact mode. Every particular value of V_{bias} will show a different contrast which is characteristic for every tip-lift height. The observation of the contrast at the chosen tip height is relevant as will be pointed out later on in this section.

- At this stage, see Fig. 3.11 c), we use the lithography module of the NanoScope software[5] to encode a script that contains instructions on where and how to move the tip on the sample. At this time too and before executing the script, we use an oscilloscope to shape the pulse: amplitude, duration, and polarity of V_{pulse} are set. Once encoded the script is compiled and executed. Initially, the tip is hovering in the middle of the scan area with the (X, Y) scan disable while the feedback is left on, so it keeps our preset tip-lift height. Then, a deposition area is selected and the tip is moved to an initial point with coordinates (x_0, y_0) that is located on that particular region. The speed of the tip is typically hundreds of nanometers per second. V_{pulse} is only applied when one of the analog outputs of the microscope is enabled through the script. This output is usually set to 5 V and it triggers the function generator that is used to shape the

[5]NanoScope software version 4.38r8.

pulse. During the application of the pulse the feedback loop is turn off[6]. After applying the first pulse we can either move the tip to another location with coordinates (x_1, y_1), relative to (x_0, y_0), and applied another pulse or do it on the same location. By using the script we can make the tip follow any desired trajectory and if pulses are applied along the way, at locations (x_n, y_n), we produce a specifically designed pattern on the selected region of the sample. In principle there are not limitations for the shape of the pattern. Data acquisition is routinely initiated just before the deposition script is executed, storage of the data only starts after pulses are being applied. When the execution of the script ends, the microscope returns to imaging in NC mode and the sample is grounded.

- At last, we can take an image while in NC mode or more commonly we ground the tip and scan the sample using IC mode to examine the topography of the newly deposited structures as can be see in Fig. 3.11 d).

After deposition of the structures the tip usually gets modified. This can be evidenced as a change of contrast while imaging in NC mode at the end of third step, which implies a modification of the tip-lift height. This way the second step, for setting up the new parameters for the same tip-lift height, is repeated as many times as needed before a new deposition experiment is performed. Changes in the quality of the topographic image while in IC mode are also noticeable. For example, in Fig 3.11 d) an improvement of the quality of the image, as compared to the one in Fig 3.11 a), due to self-sharpening of the tip.

Is important to mention that it is critical to set D larger than the free oscillation amplitude A_0 in order to avoid contact between tip and sample. A slight contact will cause an immediate local mechanical deformation of the gold coated tip owed to the strength of the interactions involved and may result in a heavily damaged tip apex, as can be appreciated in Fig. 3.13 a). If the contact happens while the

[6]Feedback is kept on just before and just after the pulse application. Because of this on/off states, we called this mode of operation intermittent feedback.

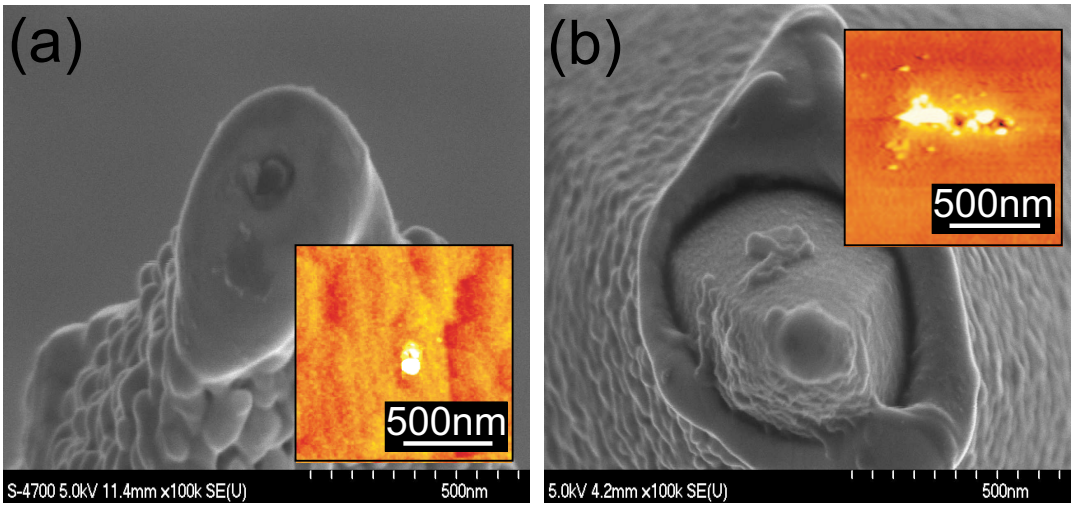

Figure 3.13: FE-SEM micrographs of heavily damaged tips after an accidental contact. a) Mechanical deformation contact. b) Contact while applying V_{pulse}. Inset: AFM scans of the resulting structures on the surface.

application of a voltage on the tip-sample gap it could lead to massive depositions on the sample surface that are irregularly shaped with several hundred nanometers in size laterally and several tens of nanometers in height, and/or total destruction of the coating of the tip which renders it unusable for further depositions. Sometimes local destruction of the surface of the sample is possible too, as revealed by Fig. 3.13 b). In this same figure, the coating appears to have melted away from the tip shank and apex. Nevertheless, the shunt resistor of 1 $G\Omega$, shown in Fig. 3.7, helps limiting this damages. One clear advantage of our deposition procedure is that prior to depositing we define the lift height and the oscillation amplitude avoiding these incidents at least for fairly flat regions of the sample.

4

From dots to wires

4.1 Monitoring of the tip's oscillation amplitude

To make sure that the lift is maintained and contact is avoided before, during, and after deposition we perform real-time monitoring of the dynamics of the cantilever and the Z-piezo displacements, as specified in section 3.2.4. In Fig. 4.1 we show the time resolved oscillation amplitude of the cantilever[1], the average deflection of the cantilever, and ΔV. As revealed by the graph, the oscillation amplitude of the cantilever is maintained constant at the prefixed value of $2A_0 = 6\ nm$ before and after the pulse application. During the pulse application the oscillation amplitude is reduced to a minimum of $1.1 \pm 0.1\ nm$. This reduction in the oscillation amplitude is expected since $A(\omega)$ as given by Eq. 2.7 has a dependence on the resonance frequency of the cantilever which is shifted by the change in interaction gradient when the voltage pulse is applied. Actually, Eq. 2.14 gives a direct relationship of the change in oscillation amplitude ΔA with the interaction gradient. As well, as shown in the graph, the pulse application causes a transitory difference in the average tip-sample separation, which corresponds to the average deflection curve. This deflection is towards the sample. However, the deflection signal unambiguously demonstrates that the tip and the substrate are not in contact.

A close look at the curves shown in Fig. 4.1 indicates that for the chosen average tip-sample distance D and free oscillation amplitude the minimum distance between

[1]Because of the Sampling Theorem only the envelope of this curve represents accurate information: our acquisition board samples at 200 kHz and the frequency of the oscillation is about 190 kHz.

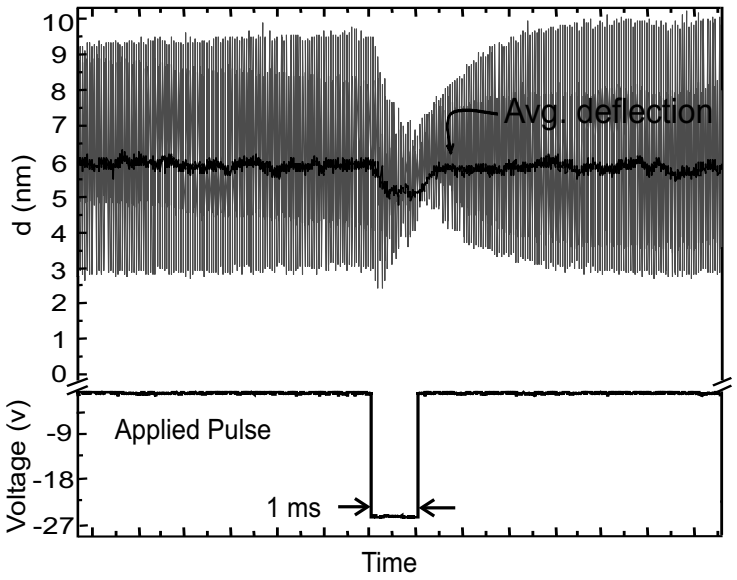

Figure 4.1: Time resolved tip's oscillation amplitude, average deflection and applied pulse in a single deposition event.

tip and sample d is always bigger than 3 nm since the small drop of the average tip-sample distance, about 0.6 ± 0.1 nm, is compensated for by the reduction of the oscillation amplitude. As a matter of interest, the fact that we regain our setup free oscillation amplitude A_0 immediately after the pulse completion indicates the absence of the formation of a liquid nanobridge, which could create a sort of electrochemical nanocell, between tip and sample [73], [31].

The electrostatic force on the cantilever caused by the pulse V_{pulse} can be calculated by measuring the small vertical shift on the average deflection curve in Fig. 4.1 a) and using $F_{elec} = k\Delta z$ the result for this particular case is 24 nN, which is in good agreement with a calculated force of 19 nN assuming a sphere-plane model, Eq. 3.1 and Eq. 3.13, with a tip radius of 60 nm measured by FE-SEM and $D = 6$ nm.

4.2 Dot dimensions characterization

To investigate the dot width and height we deposit many dots by controlling parameters like the applied pulse amplitude, duration, and polarity and the tip-sample distance. We fabricate dots that are contiguously separated by a determinate step

Table 4.1: Average FMHW width and average height for hundreds of dots fabricated with identical conditions, and with the same tip in four different deposition trials. $\Delta t = 1\ ms$, $\Delta V = 30\ V$.

$< width > [nm]$	$< height > [nm]$	Aspect Ratio [%]
24.6 ± 0.6	2.0 ± 0.1	8.1 ± 0.5
26.8 ± 0.5	1.7 ± 0.1	6.3 ± 0.4
26.6 ± 0.9	1.9 ± 0.1	7.1 ± 0.4
24.9 ± 0.6	1.9 ± 0.1	7.6 ± 0.5

size, a single pulse is applied at each step, and identical parameters are used. If the tip is moved in a linear trajectory while pulses are being applied, the result is a discontinuous dotted line that has tens of dots deposited in a very controlled manner. We fabricate many of these lines by changing or not one or more parameters at a time. We do this to obtain statistics of several individual deposition processes and evaluate how reliably we can control the dimensions of an individual deposition by setting the deposition parameters. In Fig. 4.2 we show AFM images of many lines deposited by changing either Δt or ΔV while several other parameters are kept fixed. In each image all lines were deposited with the same Au-coated tip. Section profiles[2] of selected lines are used to measure individual dots dimensions. We use the dot height, dot width, and aspect ratio, defined as the dot height divided by the dot width, for characterizing its size. Other times, instead of changing a particular parameter, we set all of them to fixed values for assessing dot fabrication reproducibility within several deposited lines. In Table 4.1 we show the average widths and heights, and the aspect ratio for each case. For calculating these averages we fabricated hundreds of dots in four independent deposition events and with the same tip. The error quoted is the standard error of the mean, defined as $\frac{\sigma_{N-1}}{\sqrt{N}}$. Is important to mention that eventually after many depositions the size of the dot becomes increasingly smaller for that same set of constant parameters. This is difficult to quantify and it changes from tip to tip. By the end of a deposition cycle fainter and fainter lines of dots are obtained. For high aspect ratio dots (20 to 40%) with an average width of 20 nm this may happen

[2]This Images and profiles were processed with the WSxM software [74].

after depositing about 350 dots. If the aspect ratio is below 10% the tip ususally last for thousands of dots.

4.2.1 Size dependence on the pulse duration Δt

Early STM and AFM deposition experiments typically involved the application of very short pulses, from few ns to tens of μs, and it was limited by the response time of the feedback loop of the system being used. Fujita *et al.* [36] reported an enhanced deposition probability for increasing pulse durations from 10 μs to 10 ms. Nevertheless, we find no clear reference in the literature to what role this parameter plays on the dot dimensions. For studying the influence of Δt we perform the deposition experiment described in section 4.2 with fix ΔV while changing Δt from 500 μs to 10 ms with the feedback loop always enabled during the deposition process, we found no influence on the dot dimensions by Δt.

For further understanding into how the pulse duration interacts with the feedback loop we plot in Fig. 4.3 the time resolved feedback response (z-piezo voltage) while applying a 1 ms pulse. It can be seen that few microseconds after the pulse leading edge the feedback circuit retracts the sample a few nanometers. This limits the effective deposition time and prevents further change of the dimensions of the dot even if longer and/or larger pulses are applied. For preventing the feedback loop to retract the sample (which increase the tip-sample separation) we performed a modification of the deposition script so it actually turns off the feedback momentarily for the duration of the pulse while the pulse is being applied. Just after pulse application the feedback is turned back on and the tip moved to the next location for deposition. The time resolved feedback response is now a 'flat line', even for pulses with a duration up to 10 ms which implies no activation of the feedback circuitry at any time.[3] In Fig. 4.2 a) we show several lines of 20 dots each which were deposited keeping ΔV constant at 30 V, changing the pulse duration between 1 ms and 10 ms, and intermittently disabling the feedback loop. Examining the corresponding section profiles of each fabricated line reveals an increased height with longer deposition periods. If we now measure

[3] 10 ms is the highest possible value for our pulse generator.

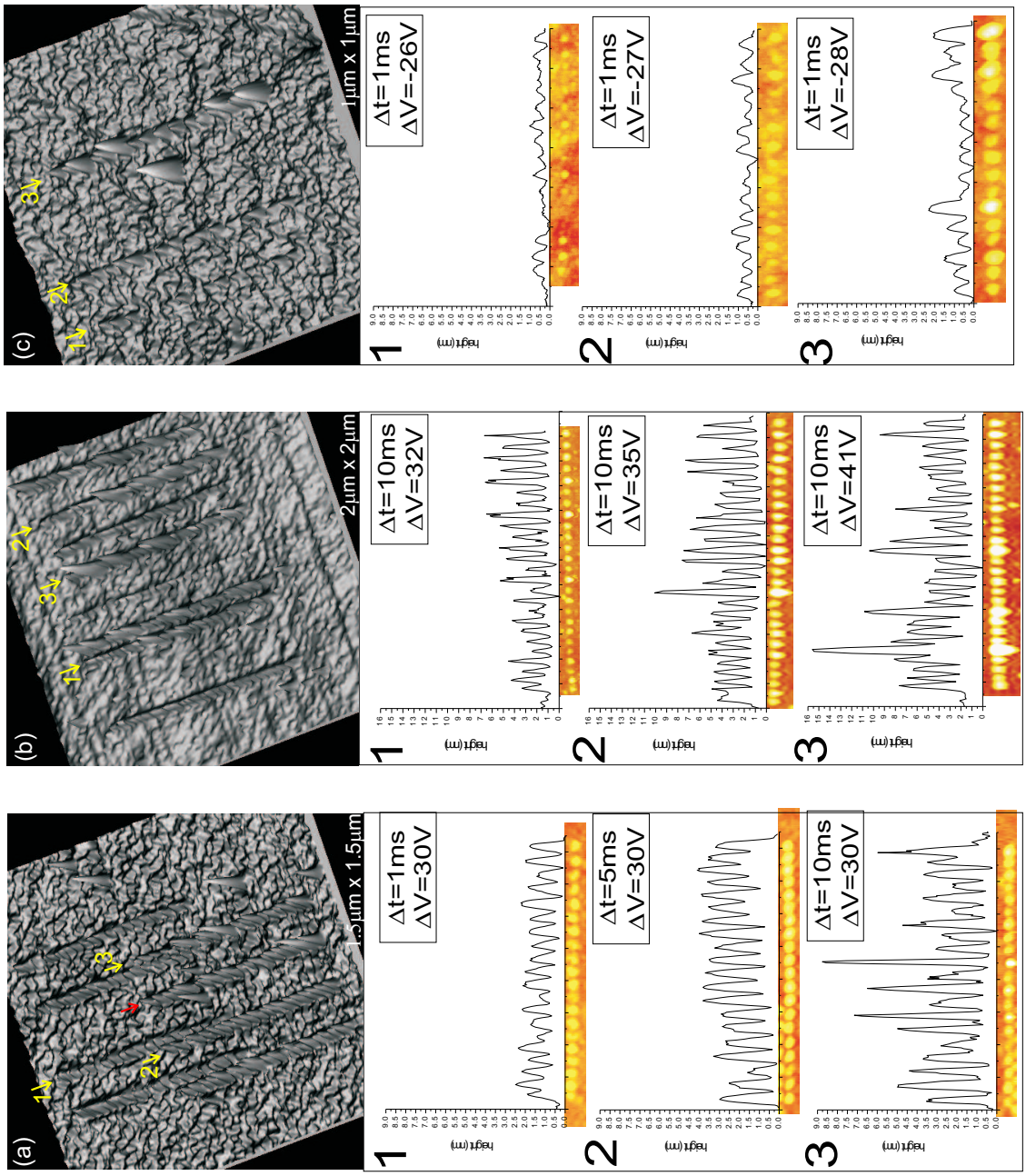

Figure 4.2: AFM images of a sequence of dots forming lines with corresponding section profiles of selected lines. (a) lines 1, 2, 3 are 20 dots deposited with fixed $\Delta V = 30\ V$, and with $\Delta t = 1\ ms$, 5 ms, and 10 ms respectively. (b) 27 dots lines deposited by keeping constant Δt at 10 ms, and $\Delta V = 32\ V$, 35 V, and 41 V, respectively. (c) 16 dots lines deposited with fixed $\Delta t = 1\ ms$, and $\Delta V = -26\ V$, $-27\ V$, and $-28\ V$. In (a), (b) with intermittent feedback, and in (c) the feedback is always engaged. Notice that the height scale is 16 nm on (b) 1, 2, and 3. For all the profiles the surface distance scale is 100 nm between major ticks of the horizontal axis which corresponds with the scale of 2D images. For all deposited lines $d = 6\ nm$, and $2A = 6\ nm$.

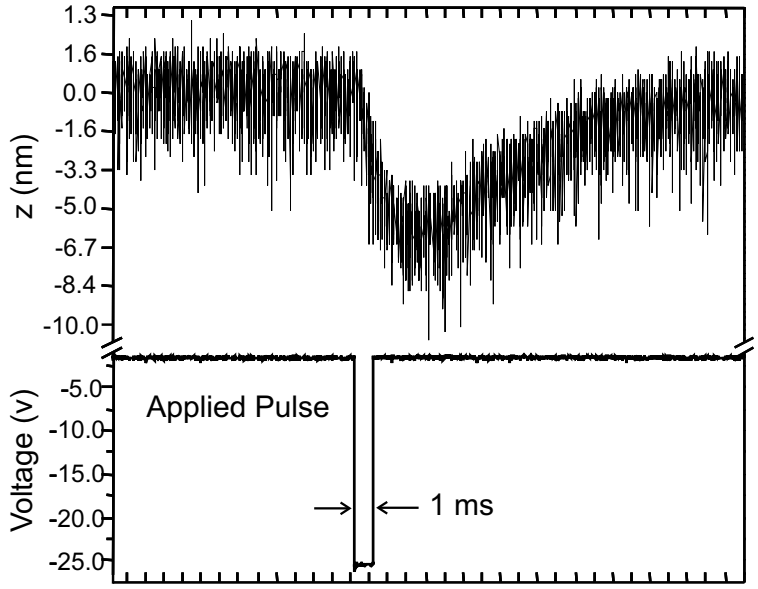

Figure 4.3: Time resolved feedback circuit response to the application of a pulse. Negative Z values corresponds to retraction of the sample.

the dots widths and heights from the corresponding section profiles and plot their averages against Δt, as shown in Fig. 4.4 a),it can be seen that the average height increases close to a 100% with increasing pulse duration. Nevertheless, Δt seems to play a small role on the modification of the dots average width. This causes an important modification of the aspect ratio of the dots, as can be appreciated from this figure. The highest aspect ratio that we were able to produce with this deposition technique is about 40%.[4]

4.2.2 Size dependence on the pulse amplitude ΔV

The effects of the pulse amplitude[5] on the dot dimensions are well documented and we observe similar trends to those reported on the literature [63], [67]. Figures 4.2 b) and c), lines 1 to 3 respectively, show an increase on both the width and height of the dot, as can be appreciated on the corresponding section profiles as well, when

[4]Precisely $A_R = (37 \pm 2)\%$, with similar deposition settings as the ones described in these sections.

[5]We indistinguishably refer to ΔV or V_{pulse} as the pulse amplitude but more strictly $\Delta V = V_{\text{bias}}$ - V_{pulse}, with V_{bias} a constant, section 3.2.3.

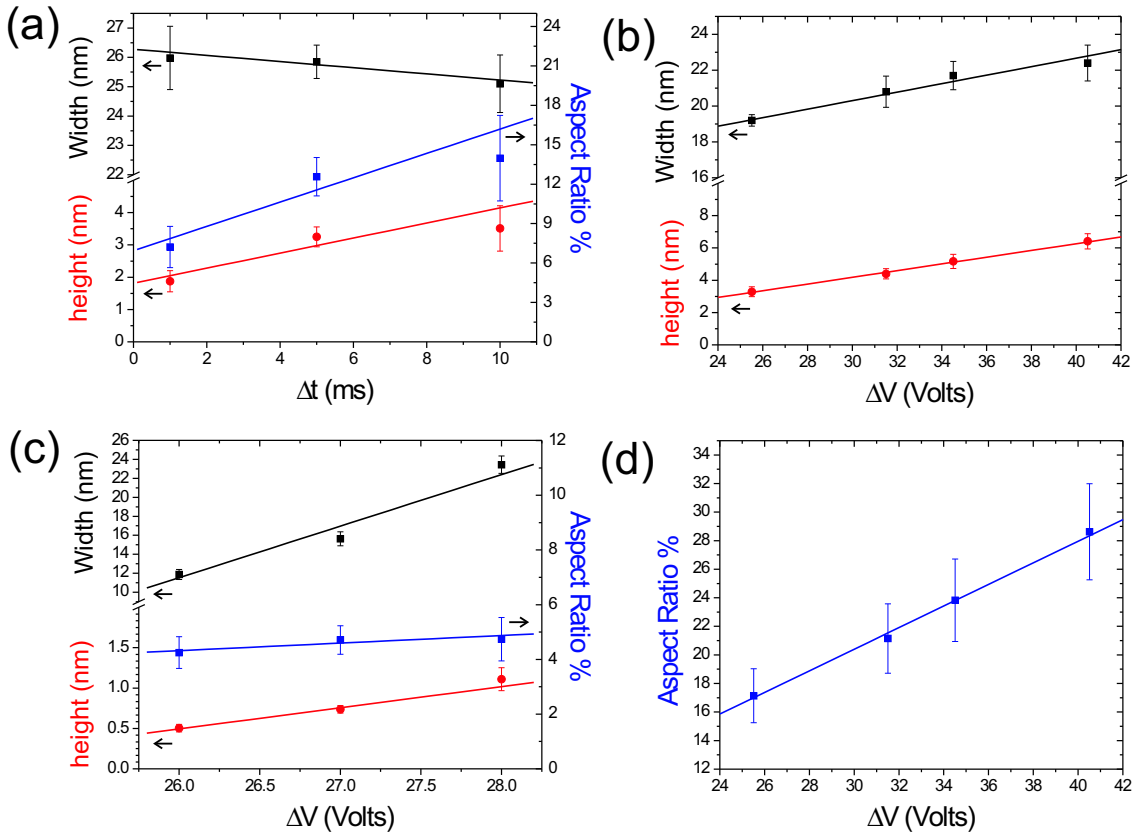

Figure 4.4: Modification of the dot width and height by (a) changing Δt, with $\Delta V = 30\ V$ or (b),(c) changing ΔV with $\Delta t = 10\ ms$ in (b), and $\Delta t = 1\ ms$ in (c). (d) Calculated aspect ratio of the data in (b). Feedback loop in (a),(b) intermittent implementation, in (c) always enabled. Each datum correspond to 20 deposition trials in (a), 27 trials in (b), and 16 trials in (c). The width is measured at the FWHM. Lines are best fit to the data.

the total voltage in the gap is increased and keeping Δt fixed and equal to 10 ms in b), and 1 ms in c). As shown in Figures 4.4 b) and c) the dots size, average width and height, increase when stepping up the total voltage in the gap ΔV, which is the main parameter determining the width of the dots. Again, the influence of the state of operation of the feedback loop affects the aspect ratio of the dots, through Δt, as can be appreciated in Figures 4.4 c) and d). In the former with the feedback always engaged, the aspect ratio seems constant around 5%, it doesn't change with increasing ΔV. However, in d) with the feedback momentarily off during the application the pulse, the aspect ratio shows an important increase with augmenting pulse amplitude. This confirms our previous result on the well-defined role that the Δt plays on the dot height and consequently in the capability of obtaining higher aspect ratios provided that we operate with an intermittent feedback.

It has to be mentioned that the dots will not keep smoothly augmenting their size if voltages well above the deposition threshold are applied, instead unshaped large mounds (few hundred of nanometers) are deposited and/or formation of pits can occur. So, it's important to apply small steps while the voltage is being increased to a value just beyond the threshold for deposition.

4.3 Deposition mechanism

4.3.1 There is a threshold

An arbitrary combination of applied ΔV and tip-sample distance d does not lead to deposition. In fact, we have found that there is a well defined deposition voltage threshold V_{th} which depends on d. This is in accordance with previous works either for STM or AFM. Its dependence on the tip-sample distance indicates that it is the applied electric field the parameter that controls the deposition process. For finding the threshold field, defined as $E_{th} = V_{th}/d$, we first set the distance and step the voltage, always applying a single pulse, from an initial small value until deposition happens. This first deposition is usually a large mound or big blob (typically with a diameter of 50-100 nm, and 25 to 50 nm high), and if we keep increasing the voltage

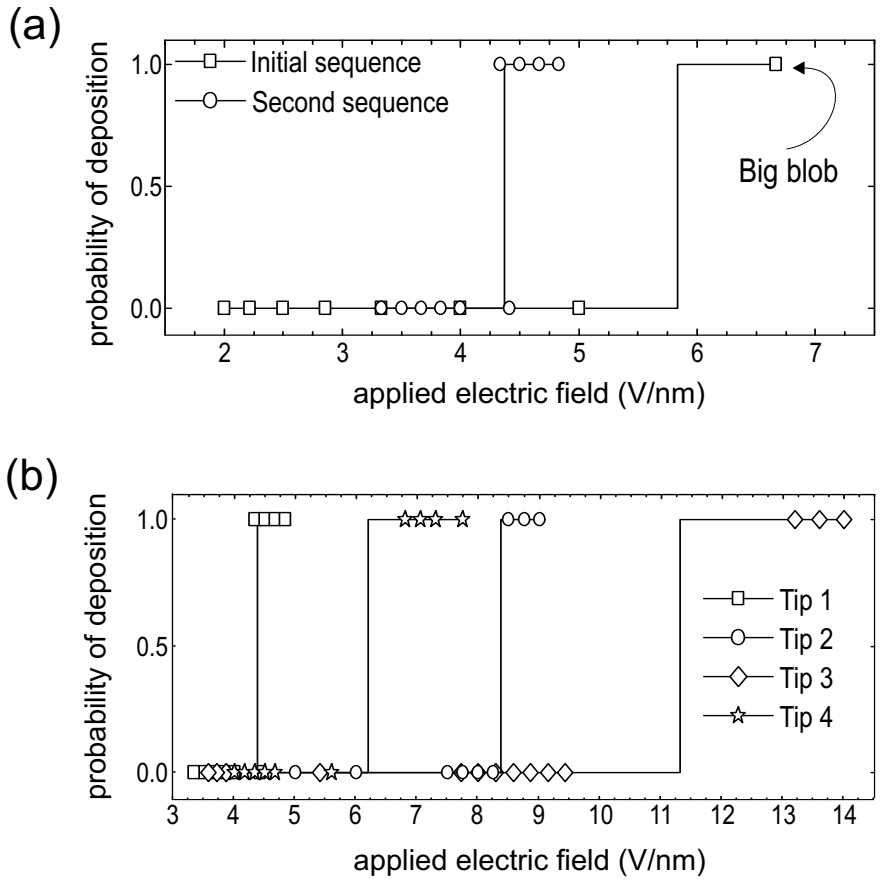

Figure 4.5: Probability of deposition while ramping the V_{pulse}, with a single pulse applied each time, and with fix d. (a) When a tip is first biased usually a big blob is deposited. Thereafter, the deposition threshold field is lowered. (b) Probability of deposition versus applied electric field for four different tips, after a sequence like in (a). Tip 2 & Tip 3 the polarity is positive, and in Tip 1 & Tip 4 the polarity is negative. All tips were Au-coated in the same evaporation batch. In both graphs each datum corresponds to 16 trials, and lines are a guide to the eye.

the deposits consist of rather large depositions. So, we must lower the voltage after this first deposition. We repeat the sequence until we deposit again and this value is what we define as the E_{th} for that tip, this is shown in Fig.4.5 a). Afterwards on we can reliably deposit dots as the ones shown on the previous section. We speculate that this is the result of removing tip contamination.

The lowering of the threshold after a big blob concurs with the previous observation of the improvement of the scanned image quality, which we attributed to the sharpening of the tip: just after the deposition of the big blob we usually get such improvement. With this first deposition the shape of the tip varies from dull to slender which influences the intensity of the electric field at the tip apex.

We have found as well, that even for tips from the same batch (when new, and then went through the same Au-coating evaporation batch) or nominally the same substrate samples[6] the value of E_{th} varies from tip to tip but within a tips usable life it keeps fixed. In Fig.4.5 b) we resume these observations. We have consistently found lower than expected threshold fields for both polarities, anywhere from 4 to 8 V/nm for Au^{2-}, and 8 to 12 V/nm for Au^{+}. In the next sections we will seek an explanation for this.

4.3.2 The rate equation

The existence of a threshold does not say anything about what deposition mechanism is at work, either field-evaporation or field-induced point contact. Both of them involve a thermal electromigration process that may allow a self-sharpening of the tip. Nevertheless, the fact that our tip never come into contact with the surface helps discard most traditional point contact approaches. On the other hand, methods that require the formation of a neck or nanobridge [65] in which the tip keeps oscillating, at a reduced amplitude, are more difficult to differentiate. However, a constant feature for FID and more generally Point Contact mechanisms is that the aspect ratio is limited and most dots have an average height from usually below 3nm. In this respect

[6] Actually, sample properties usually depends from where on the wafer they were cleaved, e. g. results are pretty consistent from pieces cut at the center.

Houel *et al.* [66] pointed out that they never succeeded in depositing higher-aspect ratio dots. A distinguished feature of field-evaporation processes is the transfer rate equation 2.24: $\kappa = \nu \exp(-\frac{Q_n}{k_b T})$. More importantly, the ability to grow higher-aspect ratio dots and its relation to the pulse duration provides a direct link to the field evaporation rate equation, since it determines the number of atoms in a deposited dot which can be calculated by $\kappa \times \Delta t$. This provides a point of departure from FID/Point Contact given the quite different role played by the pulse duration on a FED process.

For obtaining the field-evaporation rates typically involved in our fabrication process, we first calculate the number of gold atoms for dots like those fabricated in the previous section. The number of gold atoms in a dot of volume V is:

$$n_V^{Au} = V \times (\frac{\rho N_A}{m_a}) = V \times 59, \tag{4.1}$$

with V in nm^3, $\rho = 19.3 \times 10^{-21}\ gr/nm^3$, $m_a = 196.97$, and N_A is the Avogadro's number. For the volume of the dot we assume a cylindrical shape in which we use the dot average width measured at its FWHM and the dot average height. Now, the experimental deposition rate can be calculated as $\kappa = \frac{V \times 59}{\Delta t}$. We show in Fig. 4.6 b), and c) graphs of the experimental transfer rate versus the applied field for the tip with negative and positive polarity respectively. It is noticeable from these curves that the transfer rates are quite high. Accordingly to the rate equation 2.24 we can obtain higher-transfer rates by reducing Q_n and/or increasing T. Lowering the Q_n involves close tip-sample distances and high applied electric fields as can be deducted from Eq. 2.27. Using these two equations we can write the following parametric expression for the transfer rate as a function of d, E_a, and T:

$$\kappa^{Au^+} = \nu \times exp\frac{-8.71 + \frac{3.6}{r_0} + \frac{3.6}{d - r_0} + r_0 E_a^{Au^+}}{k_b T},\ and \tag{4.2}$$

$$\kappa^{Au^{2-}} = \nu \times exp\frac{-12.26 + \frac{14.4}{r_0} + \frac{14.4}{d - r_0} + 2 r_0 E_a^{Au^{2-}}}{k_b T}, \tag{4.3}$$

with d in Å, the electric field in V/Å, the tip temperature in K, $\nu = 10^{13}\ s^{-1}$, $\Lambda = 3.78\ eV$, $\phi = 4.3\ eV$, $r_0 = 2.88$ Å, $k_b = 8.617 \times 10^{-5}\ eV/K$, the ionization energies

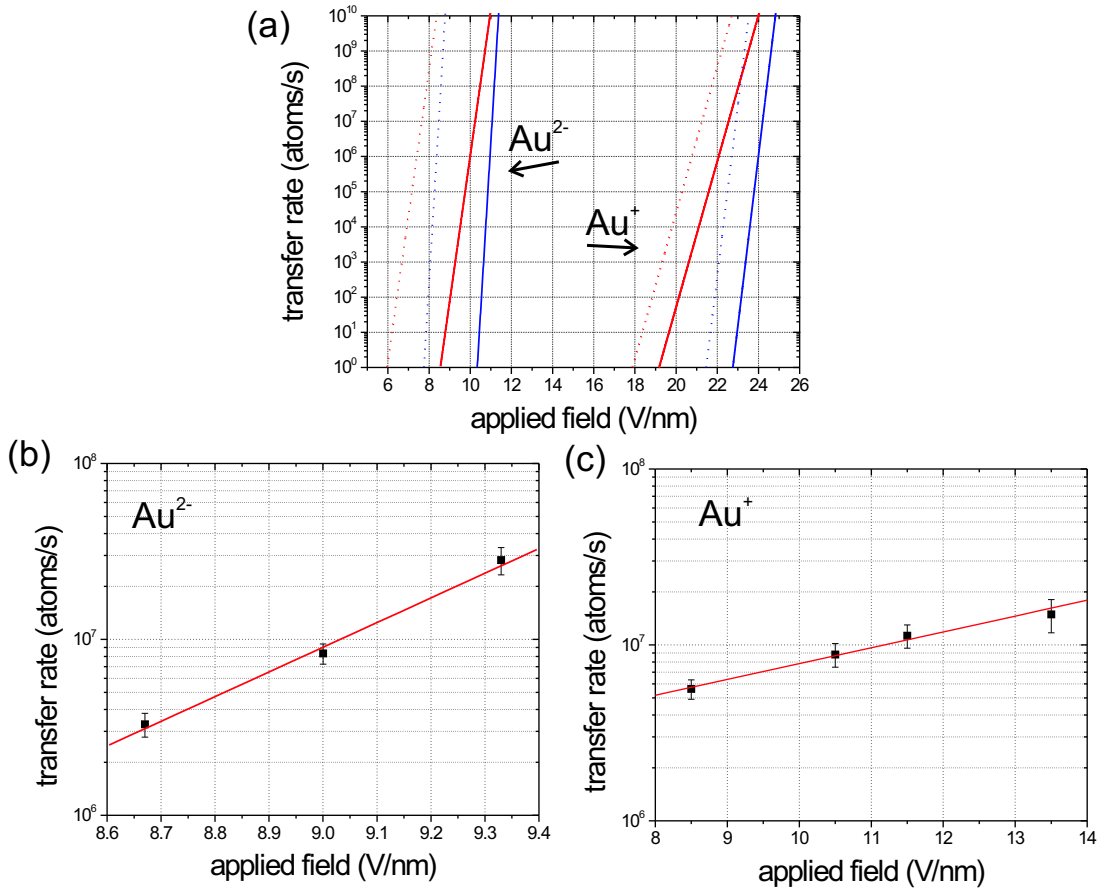

Figure 4.6: Graphs of the transfer rate vs. applied field for the ions Au^{2-} and Au^{+}. (a)Theoretical graphs calculated using equations 4.2 and 4.3. The blue lines correspond to $T = 300\ K$ and $d = 3\ nm$, in the red lines the temperature is changed to 700 K, and in the dotted lines the distance is changed to 1 nm. (b)Experimental graph for the cation Au^{2-}. (c)Experimental graph for the anion Au^{+}, the slope is smaller than in b). The experimental settings are those of the blue lines in a). The lines in b), and c) are a best fit to the data.

Table 4.2: Rate of change of the transfer rate $\times 10^6$ $atoms/s$ per 1 V/nm

	Au^{2-}	Au^{+}
Exp.	42 ± 3	1.9 ± 0.5
Theo. ($d = 1$ nm, $T = 700$ K)	113	74

are $I_1 = 10.56$ eV, $I_2 = 20.56$ eV, and the afinities $A_1 = 2.31$ eV, $A_2 = -2.19$ eV *mutatis mutandis*.

In Fig. 4.6 a) we plot the transfer rate as given by equations 4.2 and 4.3 against the applied field for the cation Au^{+} and the anion Au^{2-}, with $d = 3$ nm, 1 nm, and $T = 300$ K, 700 K. We choose these d and T values since they are compatible with conditions that can be reproduced in our experiments[7] It can be appreciated that for both polarities there is a lessening of the slope for the curves with augmenting T but higher transfer rates are possible at smaller values of the field. When tip and sample are closer the evaporation threshold is considerably lowered. This is especially true for the Au^{2-} curves, e. g. for the curve for Au^{2-} at 700 K and $d = 1$ nm the threshold field is lowered from about 10 V/nm to 6 V/nm. Now, for the Au^{+} with the same T and d the field is lowered from about 23 V/nm to 18 V/nm. This seems to point in the direction of reduced fields with high transfer rates that we obtain with our deposition process. Nevertheless, even for shorter distances or higher temperatures the rate of change of the transfer rate with the excess field[8] seems much slower for the experimental curves. As matter of fact, a calculation of the slope in Fig. 4.6 a), Au^{2-} with $T = 700$ K and $d = 1$ nm, and b) give us 113×10^6 $atoms/s$ per 1 V/nm, and 42×10^6 $atoms/s$ per 1 V/nm respectively. In table 4.2 we summarize these observations. From a comparison of these experimental results with the theoretical expectations we conclude that the deposition rate is operating in saturation mode.

Actually this slow rise of the transfer rate with excess field has been reported for a STM system and is attributed to an atom-supply limited effect [62]. This effect becomes even more evident when we graph the transfer rate versus the inverted pulse

[7] $T = 700$ K is the minimum temperature to initiate any electromigration process [75].

[8] The applied field above the threshold.

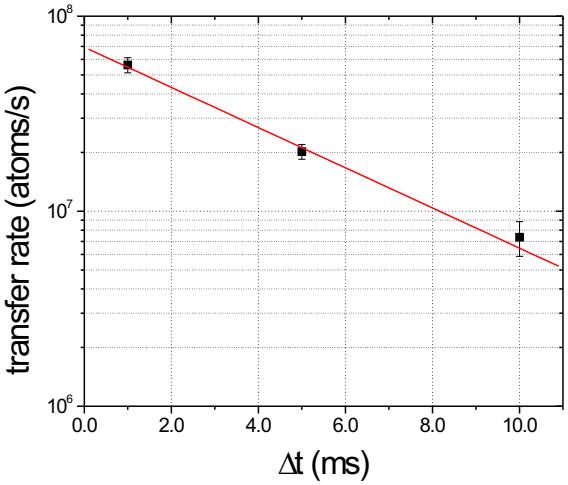

Figure 4.7: Transfer rate vs. inverted pulse length. We expected a horizontal line since the applied field is constant. Line is best fit to the data.

period at a fixed field of 10 V/nm, as can be seen in Fig. 4.7, where we expect an horizontal line if such effect were not affecting the field evaporation process.

4.3.3 The tip polarity

A closer examination of the curves in Fig. 4.6 a) shows that temperature is more effective in reducing the threshold field in the case of positive polarity than for negative, were the distance play that role. The lessening of the slope seems to be more affected too. Actually, for the Au^+ with $T = 700\ K$ and $d = 1\ nm$ we obtain $74 \times 10^6\ atoms/s$ per 1 V/nm as compared to $113 \times 10^6\ atoms/s$ per 1 V/nm for the negative case. This agrees with our experimental curves since we observe a slower rise of the transfer with temperature for the positive polarity than for the negative polarity as can be observed in Fig. 4.6 b), and c). In the former the slope is $42 \times 10^6\ atoms/s$ per 1 V/nm, and it is $2 \times 10^6\ atoms/s$ per 1 V/nm for the positive polarity.

We find too a different deposition threshold field for Au^+ and Au^{2-} for a given tip. In Fig. 4.8 we show a polarity experiment. We begin by depositing with adequate parameters for finding the evaporation threshold field for positive polarity. Two tries with $\Delta V = 19\ V$ and $\Delta V = 20\ V$ only deposited partially indicating that the threshold is close. Then, when a line is deposited for $\Delta V = 21\ V$, just over the

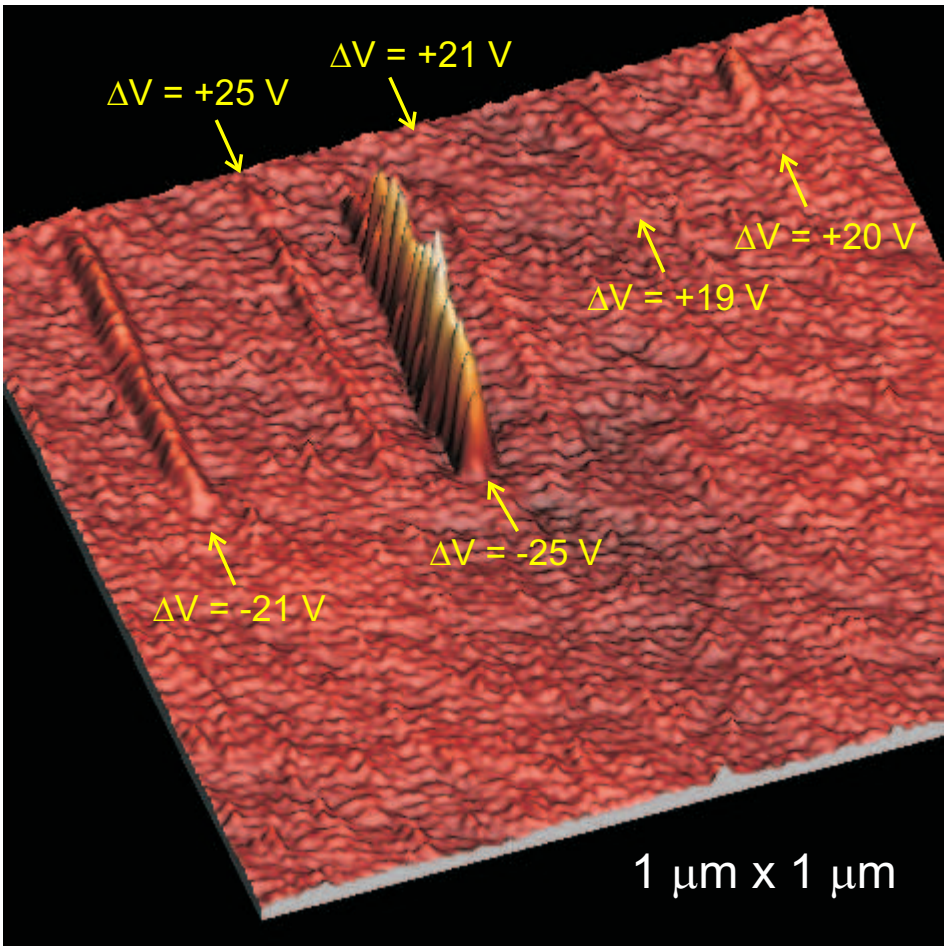

Figure 4.8: Dots deposition with identical parameters for positive and negative polarity applied to the tip. The pulse duration is fixed, $\Delta t = 2\ ms$. The maximum height for the $+25\ V$ line is 1.6 nm, or the $-25\ V$ is about 10 nm.

threshold, we revert the polarity to $\Delta V = -21\ V$ and deposit a line in which the dots have a much bigger volume, we do it again for $\Delta V = -25\ V$ and reverted to $\Delta V = 25\ V$. This time we grow even bigger dots the tallest being about 10 nm and 1.6 nm for the positive polarity one. Clearly the applied excess field acts in a very different way when the polarity is reversed as it is expected for FED.

4.4 Tip shape & electric field

In the previous chapter we addressed methods for how to account for the tip geometry and the overall capacitance of the system. We mention too that our experiment seems to be modeled more properly by the sphere-plane model since we get a linear D vs. V_{bias} in the range of tip-sample distances that we operate. A linear behavior allow us to calculate directly the electric field from the slope of that curve. Now, from our previous results we know that $E = V/d$ does not account properly for the electric field. We have not include any effect whatsoever related to the tip shape or the geometry of the system configuration in considerations for calculating the electric field.

As mentioned before, we usually get better image quality after a deposition event which we attributed to tip re-sharpening. This goes too with a change in contrast while imaging in NC-AFM mode. This implies a change in the electrostatic interaction which is related with the change on the capacitance of the system because of readjustments of the tip geometry after a deposition event. Actually, it produces a noticeable change on the tip shape as can be appreciated in Fig. 4.9. If this is the case, these changes on the tip shape should show on the D vs. V_{bias} curves as the geometry of the system is altered [71]. Nevertheless, for the distances at which we perform our experiments the relation is still linear after a deposition event. However, we have noticed that in the majority of the cases just after deposition the slope decrease. Sometimes during the many depositions events on the tip life this slope can increase too. An explanation for this behavior is the continuous changes that a tip suffers during many deposition cycles. It's important to consider too that the formation of a bump on the tip apex or a elongated tip does not withstand the mechanical

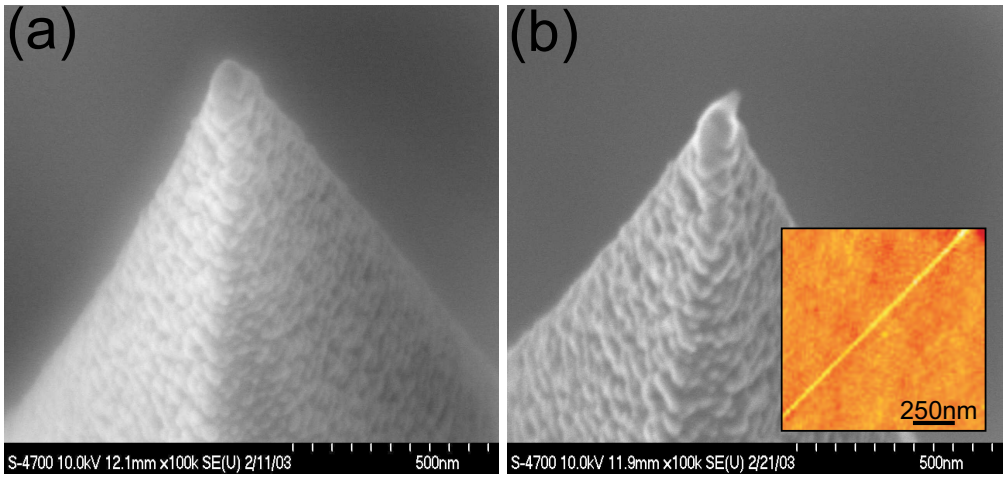

Figure 4.9: FE-SEM images of a selected tip. (a) The tip before deposition. (b) The same tip as in (a) after depositing the line shown in the inset. The tip have developed a sharp protrusion. The image in the inset is an AFM scan.

wear caused by the strength of the tapping forces and is damaged quite fast[9].

A simple way to take into consideration a protrusion like the one in Fig. 4.9 b) was introduced by Houel *et al.* [66]. They introduce a tip elongation effect due to the high electric field that modifies the tip-sample separation distance by:

$$d'(E) = d(E = 0) - \gamma \times E(d), \tag{4.4}$$

where $\gamma = 5.1 \times 10^{-2}\ nm^2/V$ is the 'elongation coefficient', which is a fitting parameter, and E is the applied electric field. They replace their tip-sample distances d by d' for calculating the enhanced field E'. For our typical experimental values of $d = 3\ nm$ for fields of 6 V/nm and 12 V/nm gives a field enhancement E'/E of 1.14 and 1.26 respectively. This enhancement falls short to explain our lower deposition fields.

A more elaborate approach that takes into account the tip shape and the geometry of the system configuration has been developed by Mesa and co-workers [76] using a image charge method. They use an approach first developed by Young *et al.* [77] while working with the topografiner. A practical way to define the electric field at the tip apex is $E = \frac{V}{k_t R}$, where R is the radius of curvature and k_t is a geometrical factor that depends on the tip shape and on the geometrical configuration of the system.

[9]The Young's modulus for gold is 78 GPa which is softer than silicon with 150 GPa.

They model the tip as a hyperboloid in front of a flat surface and obtain an analytical expression for the electric field at the tip apex [76]:

$$E_t = \left[\frac{1}{2\eta_0} ln\left(\frac{1+\eta_0}{1-\eta_0}\right)\right]^{-1} \frac{d+R}{dR} V_0, \tag{4.5}$$

where $\eta_0 = [d/(d+R)]^{1/2}$. Now from this expression we obtain the dependence of k_t with the tip-sample separation d. Notice that k_t is proportional to V_0; a plot of k_t vs. d/R allows to calculate the field strength and in principle the tip radius.

Mesa *et al.* used their image charge method for calculating plots of k_t vs. d/R. They found that for $d/R < 0.5$ all system configuration models, including the sphere-plane and truncated cone with a sphere, basically behave the same: for a given R the electric field does not depends on the overall shape of the tip. Their numerical results are well represented by k_t vs. d/R as obtained from Eq. 4.5. They find too that for $d \geq R$ the electric field depends critically on tip shape and the analytical representation differs importantly from their calculated fields.

To study the field enhancement they add a protrusion, a hemispherical bump of radius R_b, to the tip apex[10]. As revealed by Fig. 4.10, adapted from reference [76], k_b is much reduced when compare to k_t by the presence of the protrusion and hence an enhancement of the electric field at the tip apex. This enhancement only increases up to $d \approx R$. For far-field-emission, $d/R >> 1$, the enhancement is constant and close to $E_b/E_t \approx 3$ [78].

In our case the smaller tip radius is $R = 25\ nm$, and for a tip-sample average distance $D = 6\ nm$, the maximum d/R ratio is 0.24 which means that all the results for near-field-emission apply. If we choose a protrusion of $R_b/R = 0.05$ we calculate a maximum field enhancement of $E_b/E_t = 2.5$ for our experimental conditions. This enhancement amounts to our experimentally observed reduced fields for both polarities.

[10] In Fig. 3.3 of chapter 3 we label the radius of the protrusion as R_{mic}.

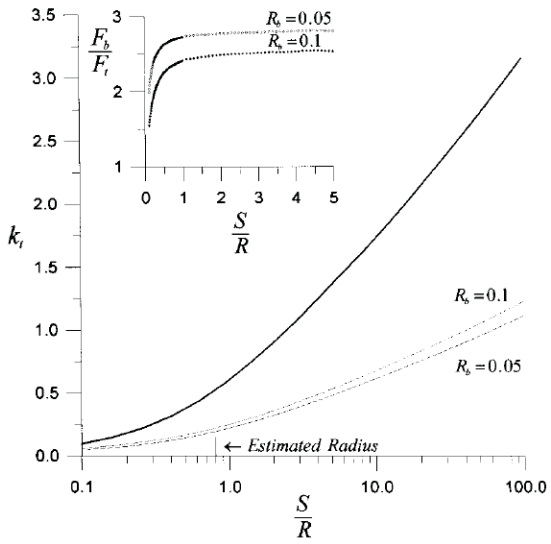

Figure 4.10: Geometric factor k_t vs. d/R for a hyperbolic tip, without a protrusion (solid line), and for hemispherical protrusions on the tip apex with ratios $R_b/R = 0.05$, and $R_b/R = 0.1$ (dotted lines). For all graphs the aperture angle $\theta = 10°$ The inset shows the field enhancement E_b/E_t for each protrusion.

4.5 Connected lines & lithography

We have devised two techniques to join or link together dots, by overlapping them, and grow a connected line or nanowire. One of them, a 'fast mode', involves moving the tip at high speed and depositing by using a high repetition rate of the voltage pulse: while the tip is being moved continuously at 250 nm/s we applied voltage pulses at a rate of 30 Hz, so a pulse is applied about every 8 nm. If we move the tip for about 4 s and make it follow trajectory of a vertical or horizontal line we can pattern a 5×5 grid like the one shown in Fig. 4.11, each line is about 6 μm with a total deposited length of 150 μm. The lines are formed by a succession of overlapping dots. These lines have a width of 64 nm, measured at the FWHM, and a height of about 2.5 nm. A detailed study of the line structure shows that it is composed of grains of about 22 nm in width at the FWHM, so every line is about 3 dots wide. Problems with this method include that is difficult to guarantee that the line is fully connected, actually in Fig. 4.11 b) we can identify several possibly unconnected regions. There is too that the aspect ratio of the line is limited. We have found that augmenting

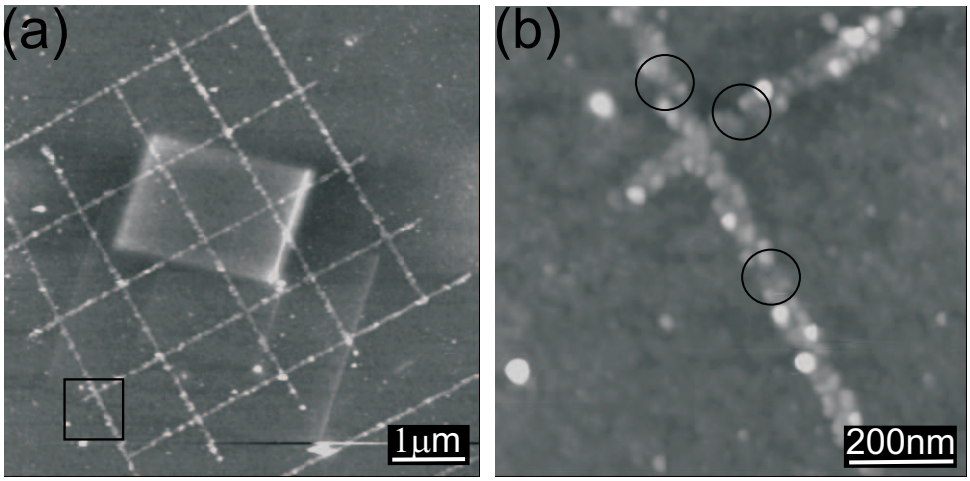

Figure 4.11: AFM images of direct lithographic patterning of Au lines. (a) 5×5 lines grid, each line have a width of 64 nm (about three grains) and a height of 2.5 nm. (b) Magnified image of the region of the black square shown in (a), suspected fracture zones are marked by circles. Several SEM spots are evident in (a).

the duty cycle tends to produce unreliable results since accidental destruction of the surface or the device happens often.

We also developed a 'slow mode' in which we first deposit dots by scanning the tip stepwise and applying a single pulse at each step, as done in previous sections, and then joining them together by an interdigitated deposition of dots so we fill gaps between existing, previously deposited, dots. In Fig. 4.12 we show a sequence of 'deposit over' experiments.

This technique is very versatile since it can be used to repair in situ damaged or unconnected wires or other structures. Advantages of this method are high aspect ratio and well connected lines. Nevertheless, the technique relies on the scanner ability to position the tip over the growing structure; some times piezo drift will cause a misalignment of an interdigitated deposition which may change electrical properties of the wire being made. Another disadvantage of this technique is that if several μm's of lines need to be fabricated it is a rather slow process[11]. Both fabrication techniques benefit from the highly-developed lithographic capabilities that SPM offers. As a demonstration of this we patterned the structures shown in Fig. 4.13.

[11]The duty cycle is about 1%; for the fast mode it is about 30%.

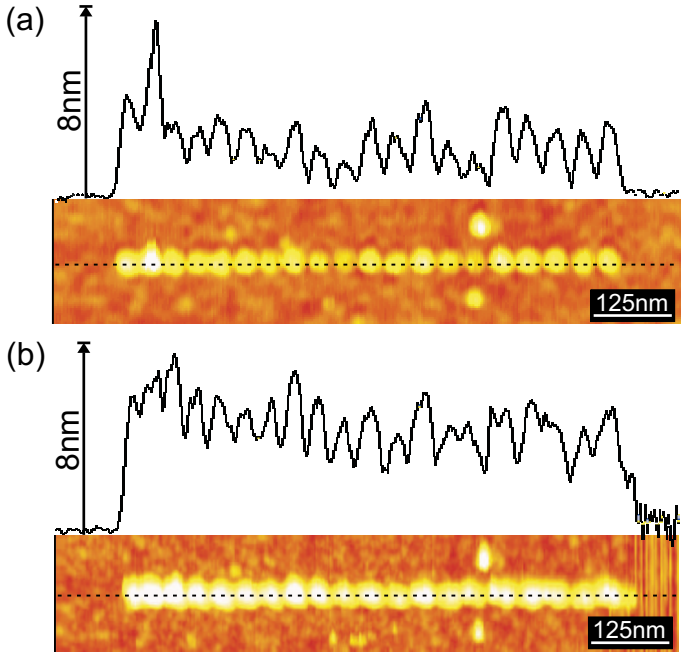

Figure 4.12: First and last stages of a deposit over experiment. (a) First a 750 nm line, formed by 20 dots of approximate width of 22 nm FWHM, was deposited from left to right. It can be appreciated in the section profile the gaps between consecutive dots. (b) After two interdigitated depositions, with the same conditions for deposition as in (a), the line has double its height and no gaps are present. Settings for the deposition: $\Delta V = 30$ V, $\Delta t = 10$ ms, and the tip is positive polarized.

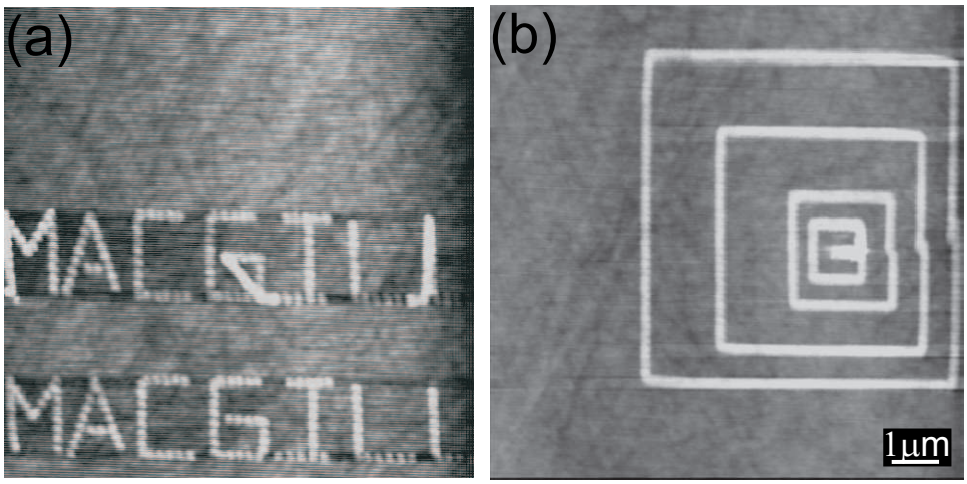

Figure 4.13: (a) Using the tip as a dot matrix printer, $1\mu m \times 1\mu m$ letters forming the word macgill. Initially an error was found on the letter g and then the deposition was repeated with the correct script. (b) 5 squares deposited in the same sequence from the inner to outer one. The imperfection seen at the right side of the square is due to hysteresis of the piezo scanner. Imperfect spell checking is also evident.

5

Electrical characterization

By the end of the last chapter we described two techniques to fabricate nanowires by overlapping gold dots. Because of the way they are grown these wires have quite different microstructures. The fast-mode wires are polygranular whereas the slow-mode ones present a bamboo-like structure [79], [80], [9], [81]. In Fig. 5.1 we show a schematic longitudinal cross section of these wires. As we will see, electrical conduction properties are affected by the microstructure. For electrical testing of nanowires we need to connect at least two electrodes, one at each end of the device. Then a simple experimental setup is used to establish a potential difference between the electrode terminals and measure the current flowing through the device. The applied voltage biases V and measured currents I are used to plot I-V curves that fully characterize the electron transport properties of the device.

5.1 Introduction: Electrical properties of small wires

5.1.1 Conduction properties

Electrical transport properties of macroscopic wires, in which electron transport is a diffusive process, are completely described by the Ohm's Law, the current I flowing in a wire is proportional to the potential drop V on the wire: $V = I \times R$, where R is the electrical resistance which, for a wire with cross-sectional area A and length l, is given by:

$$R = \rho \times \frac{l}{A}. \tag{5.1}$$

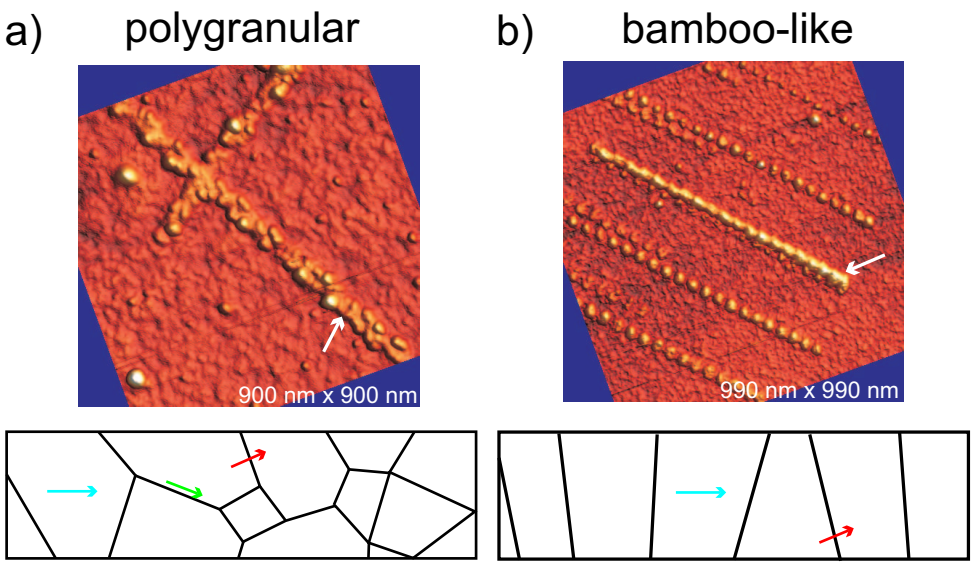

Figure 5.1: Schematic longitudinal section of the microstructure of fabricated wires. (a) Polygranular wire deposited using the 'fast mode'. Cross section area $3{\times}64\ nm^2$, about 3 grains wide. (b) Bamboo-like wire deposited using the 'slow mode' and several overlapping depositions. Cross section area $10 \times 22\ nm^2$, about one grain wide. Atomic diffusion modes: intergranular (blue arrow), along grain boundaries (green arrow), and transgranular (red arrow).

The resistivity ρ is intrinsic to the material of the wire and is mostly determined by the charge carrier density and the conduction electrons mean free path λ. The bulk value for gold at 300 K is $\rho_0 = 22\ \Omega\text{-}nm$.[1] As we shrink the size of the wire to dimensions comparable to λ, size effects become increasingly important and Ohm's Law fails to properly explain electron transport at small scales. When the dimensions of the conductor are comparable to the Fermi wavelength λ_F, the electron transport becomes ballistic. This transport regime is described by the Landauer-Büttiker (LB) formalism. In Table 5.1 we summarize different transport regimes which are appropriate for a characteristic scale for the dimensions of the wire and the corresponding theoretical framework used to describe them.

In the mesoscopic regime, between Ohm's Law and the LB formalism, for dimensional scales of the order of the mean free path and several times λ_F, electron transport in conductors is a less understood process. As a matter of fact, large deviations of the resistivity from the bulk value ρ_0 are observed in metallic polycrystalline

[1] The conventional way to expressed is $\rho_0 = 2.2\ \mu\Omega\text{-}cm$.

Table 5.1: Transport regimes vs. Size

Dimensional Scale	Transport Mechanism	Theoretical Framework
$10\ \mu m \rightarrow 100\ nm$	Diffusive	Ohm Law (Laplace Eq.)
$100\ nm \rightarrow 10\ nm$	Quasi-Ballistic	Non-equilibrium Boltzmann
$10\ nm \rightarrow 1\ nm$	Ballistic & Semiclassical	Sharvin
$1\ nm \rightarrow 0.1\ nm$	Ballistic & Quantum	Landauer-Büttiker

thin films and wires. Fuch, using Boltzmann transport equation, first derived an expression for the resistivity when only one dimension is confined [82]. In an extended thin film surface effects are important in the calculation of the resistivity because of surface scattering. Later, Sondheimer extended Fuch's theory by adding an extra dimensional confinement to include wires with square or circular cross sections [83]. The Fuchs-Sondheimer (FS) model introduces a specularity parameter p which is the fraction of electrons that are specularly reflected at the external surfaces, completely diffusive surface scattering implies that $p = 0$. Gold has been found to have a large value of specularity[2] $p = 0.5$ [81]. Their combined theory gives reasonable agreement with experiments for thin films and wires with a line width w of few micrometers. Nevertheless, their model does not account for experimental data with enhanced resistivity when $\frac{w}{\lambda} \approx 1$ and with experiments in which the thickness of the thin films is comparable to the mean grain size D_{50} of the films. For solving the first limitation, an approach using kinetic-theory arguments for calculating the resistivity by Chambers, is widely employed [81], [85]. The solution of the second limitation involves considering scattering on internal surfaces. For this purpose Mayadas and Shatzkes (MS) proposed a new theory by imposing a further restriction in the conduction electrons mean free path by the presence of additional scattering centers located at grain boundaries [86]. They introduced a new parameter, the reflection coefficient R, which is the fraction of electrons that are not scattered by the potential barrier at a grain boundary.

[2]Actually this is true for other noble metals and is presently a subject of great interest in the fabrication of spin valves [84].

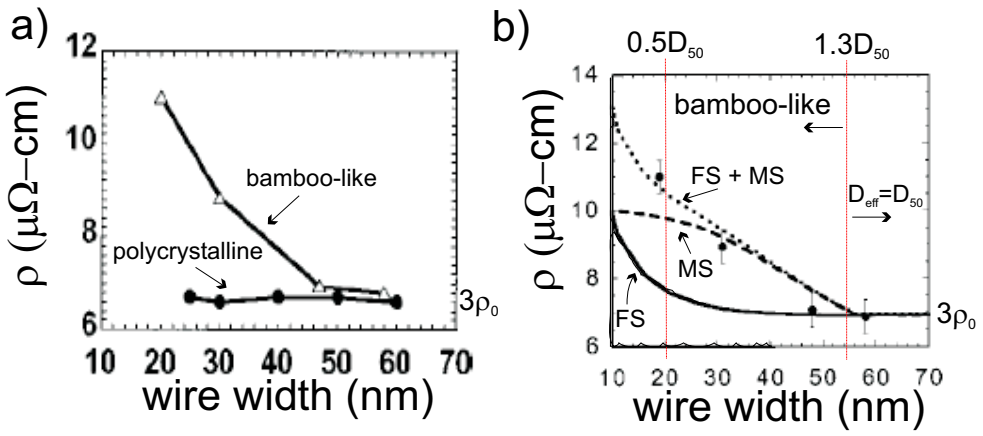

Figure 5.2: (a)Experimental resistivity for wires with different microstructures. The width of the grains are 60 nm, and 20 nm for the bamboo-like , and the polycrystalline wire respectively. (b) Modification of the MS theory by considering a log-normal distribution for the grain size. Adapted from [81].

The total effect due to scattering on external/internal surfaces on the resistivity can be calculated by combining both models using Matthiessen's rule[3]. This rule states that the total resistivity can be described by a single relaxation time τ [88]:

$$\frac{1}{\tau} = \frac{1}{\tau_{FS}} + \frac{1}{\tau_{MS}}, \tag{5.2}$$

or equivalently $\rho = \rho_{FS} + \rho_{MS}$. Strictly it can show that Mathiessen's rule holds as an inequality in which the total resistivity is bigger than or equal to the sum of the individual scattering effects [88]. Several experiments with metallic polycrystalline thin films and wires have been properly described using this method [86], [89], [81], [85]. Steinhögl *et al.* studied the combined effects of external/internal surface scattering and background scattering (temperature dependent) and successfully described experimental resistivity data for 40 to 800 nm wide Cu wires [85]. Nevertheless, most authors use Eq. 5.2 more as an estimation of the relative importance between surface scattering and grain boundary scattering (experiments typically done at ambient conditions) or between the FS term and background scattering (typically temperature dependent experiments).

[3]Landauer showed that Matthiessen's rule will not be satisfied simultaneously for reflection at potential walls (τ_{MS}) and background scattering (τ_{bg}) of the electron and phonons, and defects [87].

Durkan & Welland [81] while studying bamboo-like structured Au wires[4] with similar dimensions to the ones shown in Fig. 5.1, found an enhanced width-dependent resistivity data that was not possible to explain using the combined FS and MS terms. The data is shown in Fig. 5.2 a). They proposed to change the less realistic approach of the MS model which assumes a mean grain size D_{50} and a gaussian distribution, for a more natural log-normal distribution for the grain size. By doing this they found that the mean distance between grain boundaries, that is the 'effective' grain size D_{eff}, decreases with decreasing linewidth in the interval $0.5D_{50} < w < 1.3D_{50}$. When the width is about $1.5D_{50}$ then $D_{eff} = D_{50}$ and the wire has a polycrystalline structure like the one in Fig. 5.1 a). They reported values as high as 5 to $6 \times \rho_0$ when $0.5D_{50} < w < 1.3D_{50}$. In addition they found that a polygranular wire (few grains wide) has a resistivity of about $3\rho_0$ that does not depends on the width, provided that $w > 1.5D_{50}$. These results are summarized in Fig. 5.2 b). It is interesting that the FS term becomes the most important contributor to the total resistivity when the linewidth is smaller than $0.5D_{50}$.

Bietsch *et al.* [90], [91] reported that for gold wires formed by discrete grains two to three grains wide, the R vs. l curve consisted of continuous linear sections with 4 to 10 Ω steps at single grain boundaries (SGBs). The continuous sections were fitted with Eq. 5.1 with a slope of 133 Ω-nm or $6 \times \rho_0$. The resistance steps were matched to the Shervin resistance at the SGBs. Also, they found high values of the reflection coefficient $\mathtt{R} = 0.8$ at the SGBs in agreement with Durkan & Welland ($\mathtt{R} = 0.9$), for the wires described above, and their theoretical estimation of $\mathtt{R} = 0.85$. This high value of $\mathtt{R}$ is only observed in nanowires. For thin films it is much lower ($\mathtt{R} \approx 0.2$) since current paths can be established through less reflective grain boundaries and thus only reflecting an average.

Nevertheless, Calleja *et al.* [47], in the only report that involves Au wires fabricated with FED and an AFM, found resistivity values of 300 Ω-nm ($14 \times \rho_0$) for a

[4]Fabricated using e-beam lithography on a Si/SiO_2 substrate. Dimensions: 15 to 80 nm wide, 500 nm long, and 20 nm thick.

600 nm long wire, and 900 Ω-nm ($41 \times \rho_0$) for a 200 nm long wire. The wires were polygranular with an average grain size of 7 nm, 10 nm thick, and 40 nm wide. Such a high resistivity cannot be explained with the previous theoretical considerations which would have predicted a resistivity of about 66 Ω-nm ($3 \times \rho_0$) for wires of such dimensions & characteristics. Those wires were deposited with a positive polarity which excludes oxidation as a possible mechanism for these enhanced resistivity [46].

5.1.2 Failure mechanisms

As electrons flow in a conductor in the presence of an electric field, they transfer momentum to typical scattering centers, lattice atoms, impurities, *etc.*, excerpting a force, and heating up the wire. This make the atoms more mobile. Heating depends on the efficiency with which the wire dissipates to its surroundings the energy input from the current flow. This energy is related to the resistivity of the wire and is given by $j^2 \times \rho$, where j is the current density. The excerpted force can make the scatterers move out of their original sites, and because of lattice phonons, the process is enhanced with increasing temperature. Mass transport follows the electrons flow and since material is not replaced as fast as it leaves, current densities are much smaller on the electrodes connected to the wire terminals, and voids appear in the microstructure on the vicinity of the terminal at a lower potential. As mass movement progresses, voids merge, and set up a stress gradient that eventually causes the failure of the wire.

The process just described is called electromigration and is the most common process through which a conducting wire fails. It is a diffusive process in which there is a particular time to failure at a given temperature. Black [92] gave a phenomenological description by defining a mean failure time as:

$$MFT = \frac{C}{j^n} \exp \frac{E_a}{k_b T}, \tag{5.3}$$

where C is a constant which depends on the geometry and microstructure of the wire, E_a is the activation energy of the process, and the exponent of the current density j has been reported to be $n \approx 2$. For gold, the activation energy is $E_a = 0.9\ eV$.

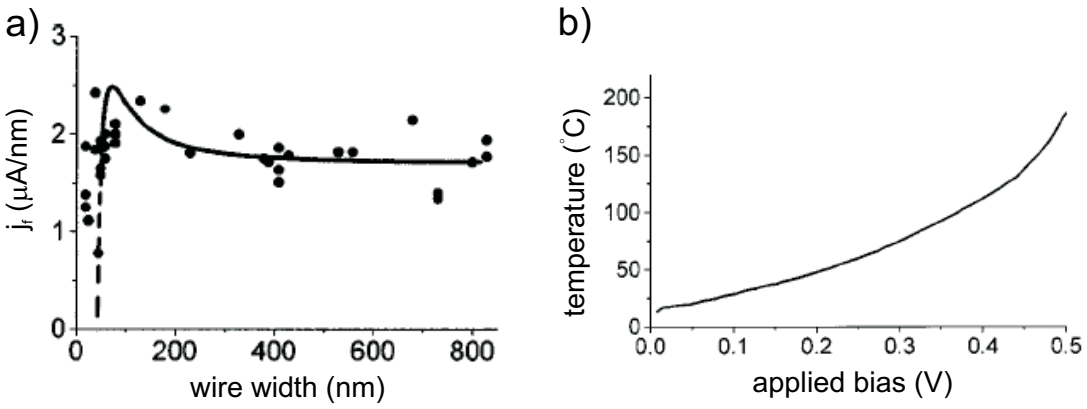

Figure 5.3: (a) Failure current density for gold nanowires. (b) Failure temperature for an electrically stressed nanowire. The nanowire fail at about 500 K. Adapted from [9].

Instead of measuring the MFT, Durkan *et al.* introduced two figure of merit concepts for the study of failure properties of nanowires with cross sections of a few hundred square nanometers [9], [75]. They defined the failure current, current immediately prior to failure, and the failure temperature, temperature at the failure current. Their findings are summarized in Fig. 5.3. For nanowires fabricated on Si/SiO_2 substrate with an oxide layer of 77 nm, 20 nm thick, 1000 nm long, and widths ranging from 20 to 60 nm, the failure current density j_f ranges from 1 to 2 $\mu A/nm^2$, as can be appreciated from Fig. 5.3 a). The bulk value of the failure current density for gold is 0.01 $\mu A/nm^2$. They noted that these values can be higher for thin oxide layers, and practically did not change for oxide layers thicker than 20 nm. They also modeled the temperature distribution on the wire which predicts that for widths smaller than 60 nm the temperature is higher at the middle of the wire and actually the failure points were also located at this position. For wider wires, the failure point moves toward the terminal at a lower potential. As revealed by Fig. 5.3 b), the failure temperature for such widths is around 500 K. For similar sized wires Lambert *et al.* [11] with experiments done in vacuum, measured a failure temperature close to 400 K. For the same wires mentioned in the previous section, Calleja *et al.* [47] measured current densities of 0.5 $\mu A/nm^2$,and 0.01 $\mu A/nm^2$, safe from the expected failure current of 8 $\mu A/nm^2$ (for a 4.3 nm grown oxide layer).

Table 5.2: Calculated transport & failure properties of fabricated wires

Structure	ρ_{wire} [Ω-nm]	j_f [$\mu A/nm^2$]	A [nm^2]	l [nm]	V_f [mV]	I_f [μA]
polygranular	66	2	3×60	1000	132	36
bamboo-like	132	1.2	10×20	750	120	24

Sanchez *et al.* [79], [80] reported that MTF's are much better on bamboo-like wires. By annealing the wire, which changes the microstructure, the MTF increased from 6.3 h to 286 h. Differently from polygranular wires, where fractures tend to appear along grain boundaries, bamboo-like wires presented fractures usually close to the SGB but not at the boundary.

For the wires fabricated for this project, as we will examine in section 5.3, a thinner InP buffer layer does not imply better dissipation and thus a higher MTF since the wires are in direct contact with an InP layer. Safe operational voltages and currents have to be below the failure values. Approximating the failure density current with values from Fig. 5.3 a), and resistivity values from Fig. 5.2 a), the failure voltage drop on the wires V_f can be calculated using Ohm's law and equation 5.1:

$$V_f = j_f \times \rho_{wire} \times l. \tag{5.4}$$

The expected values of transport and failure properties for wires with structure and dimensional scales like the ones in Fig. 5.1 are summarized in Table 5.2.

5.2 Experimental setup & methods

5.2.1 Micro-electrodes fabrication procedure & sample preparation

In order to connect the nanowires to an external circuit for I-V characterization measurements we have designed & fabricated[5] μ-electrodes patterns on the InP/InGaAs/InP substrates. Over the years several designs were developed and finally only two of them were used to grow nanowires and perform measurements. In this section we will describe work done with what we call design II, which has been developed more recently.

[5] As for the heterostructure substrates, these micro-electrode patterns are fabricated by Jean Lapointe and Alicia Kam of the Nanofabrication Group at the NRC-Institute for Microstructural Sciences.

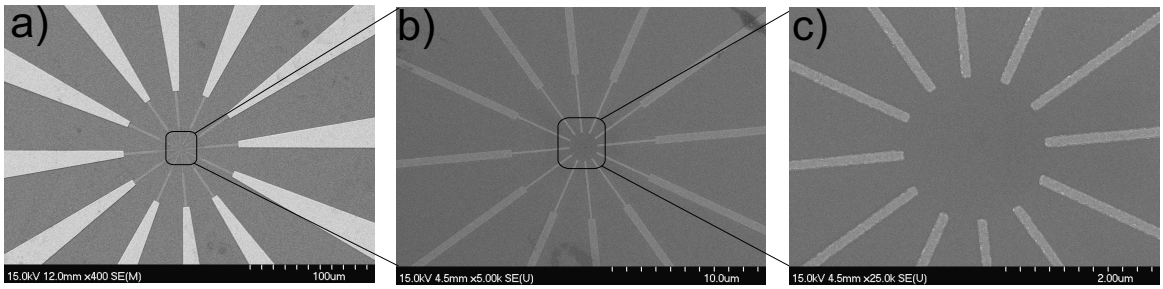

Figure 5.4: FE-SEM scans at different magnifications of patterned Au μ-electrodes with design II. In (a) both optical (bright features) and e-beam lithographic (dark features) steps are noticeable. (c) Device fabrication area.

Design I presented many problems and it will be discussed later in section 5.3. The main difference between them is the geometry and distribution of μ-electrodes and connection pads.

The patterns are fabricated on the heterostructure substrates surface by standard photolithographic techniques, e-beam lithography, and lift-off techniques. For the larger structures, the macroscopic Au electrodes and connection pads, first a mask is created by coating, baking, exposing, and developing photoresist (Shipley 1813). This is followed by a metal deposition and lift-off. The metallic layer consist of a 20 nm thick Ti adhesion layer and 150 nm thick Au film. Finally, the smaller features, the μ-electrodes, are fabricated by exposing e-beam resist (PMMA) with an electron beam. After developing the exposed areas, a metal deposition of a 10 nm thick adhesion layer of Ti and a 15 nm thin layer of Au is performed (design II) or 2nm/18nm thick Ti and Au respectively for design I. The last step is lift-off of unexposed areas.

FE-SEM scan images of μ-electrodes pattern design II is shown in Fig. 5.4. In a), the brighter structures correspond with thicker metal layers, and in b), c) the e-beam fabricated structures appear darker. In this design the μ-electrodes terminal leads form a circle with a diameter of 2 μm. There are a total of 12 terminal leads and they are distributed in four groups of three electrodes each. The angle between the electrodes is then 30°. The minimum distance between contiguous μ-electrodes is about 345 nm, as can be appreciated in Fig. 5.4 c). At the other end of the terminal leads, the wider part of the macro-electrodes form the other connection terminal:

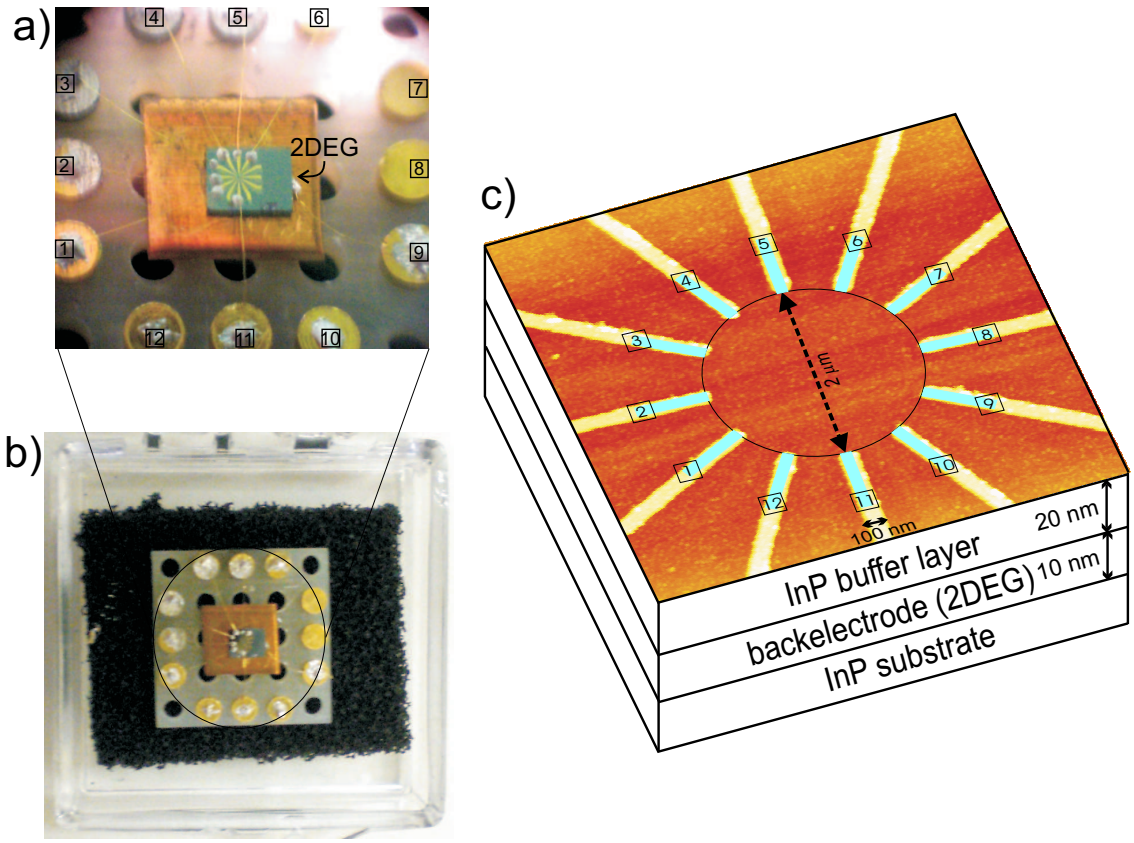

Figure 5.5: (a), (b) Optical images of a patterned InP substrate mounted on a chip carrier with 12 pin connectors. (c) An AFM scan of the center of the pattern. The μ-electrodes terminal leads are 100 nm wide, 3500 nm long, and 25 nm tall. The circle inscribed by the μ-electrodes has a diameter of 2 μm.

25×25 μm^2 contact square pads. The pitch between pads is 25 μm.

The preparation of the sample involves the following steps:

- **Mounting**. In a small, 1 to 2 centimeters, piece of wafer 15 to 20 electrode patterns are fabricated per batch. Then, they are cleaved into pieces of dimensions 3×4 mm^2 which only contain one pattern. The substrate is cleaved leaving an extra space to the left of the pattern as shown in Fig. 5.5 a). The individual pieces are then mounted in a chip carrier of 12 pins, as can be appreciated in Fig. 5.5 a), and b). The substrate is glued with silver paint onto a Cu slab, which gives the right height to the substrate on the carrier, slightly above the carrier pins. Since the μ-electrodes have to go into the AFM for nanowire fabrication,

this is an important consideration in order to avoid mechanical interference or electrical contact with the cantilever or the body of the microscope. The Cu slab also serves as a heat sink while bonding wires. The pattern has to be carefully centered in the middle of the carrier before is attached to it. Movements of the microscope head translational stage are restricted by the dimensions of the carrier and carrier holder on top of the microscope piezo scanner, so there is not much room for centering the sample using the microscope stage. The carrier is plugged into a matching carrier holder on top of the microscope piezo. The carrier holder is connected to a switch box with 12 individual BNC connectors, one for each pin. A properly gauged, insulated Cu wire has to be used in order to not couple vibrations to the microscope.

- **Wiring**. The extra space of substrate to the left of the pattern serves to allow enough space for the connection to the 2DEG, as can be seen in Fig. 5.5 a). The backelectrode is the first connection to be made on the substrate. Some In is melted with a low temperature solder, then the tip is put in contact with the border of the substrate and an In contact is formed at this location. A 25 μm diameter gold wire is first connected to pin 9, then the other terminal of the wire is attached to the In contact previously formed on the substrate.

  Several methods were attempted to wire the pads on the substrate to the pins in the carrier. The ideal wire bonding methods are the widely used wedge, and ball bonding. We tried both. Many experiments were performed to find good physical parameters of force, ultrasonic energy, heat, and time. Nevertheless, adhesion problems of the films to the substrate prevented us to successfully attach wires to the pads. Adhesion problems were partially solved by depositing thicker Ti/Au layers. Still, even successfully bonded wires were not proper contacts since the InP buffer layer was not strong enough to withstand the wiring process and mechanical damage shortcircuited the μ-electrode pad with the backelectrode.

  The same results were obtained when using the low temperature solder and In

on the pad. In this case there were no adhesion problems but the bonded wire was always shortcircuited to the 2DEG. We suspect that the surface diffusion of In may have been the cause.

The best found solution was to use the low temperature solder and In on the pins for first attaching one end of a gold wire, then by carefully positioning the other end of the wire on the contact pads, and applying silver epoxy. The dimensions of the epoxy drop must not be much bigger that the pad to avoid shortcircuiting neighboring pads. For this purpose we developed a tool by melting, bending, and pulling apart a micropipette that ended in a sharp angled tip. With this tool it is possible to deposit epoxy drops with a diameter of about 25 μm. The silver epoxy was cured at a temperature of 80°C for 3 hours. The sample shown in Fig. 5.5 was wire bonded using this method.

Wires are not connected to the pads to the left of the pattern because the cantilever tip approaches the substrate from this direction. This would not be a problem if the contacts are made with a wire bonder, otherwise it is very difficult to control the height of the epoxy mounds on top of the wire on the pad.

The higher position of the pads relative to the pins allows the wires to be connected at an angle. There is always some tension on the wire so that the wire does not curve up and touch the cantilever or the microscope body.

- **Handling precautions**. Transportation of the sample is always done in a closed plastic sample container with the carrier pinned to a conductive foam to keep all the electrodes and 2DEG at the same potential, as shown in Fig. 5.5 b). This is important to avoid ESD damaging of the sample. All the wire bonding activities are done with the sample in the plastic container, and always working grounded.

Once the sample is mounted and bonded, it is ready to be used for in situ device fabrication and I-V characterization. Our measurement setup allows these procedures

Table 5.3: Calculated transport & failure properties of μ-electrodes terminal leads

Geometry	ρ_{wire} [Ω-nm]	j_f [$\frac{\mu A}{nm^2}$]	A [nm^2]	l [nm]	V_f [mV]	I_f [mA]
design I	66	2	20×100	3000-7500	400-1000	4
design II	66	2	25×100	3500	500	5

to be done simultaneously.

5.2.2 Measurement setup

Once the sample is mounted, all wired μ-electrodes and the 2DEG can be accessed through a switch box that has 12 individual Input/Output BNC connectors that are wired to the carrier holder pins. Each BNC connector on the SW box can be left floating, grounded, or connected to an arbitrary voltage bias. All the BNCs can be shortcircuited which is important when connecting the carrier to the holder and keeping the 2DEG and electrodes at the same potential. Other important considerations when using the switch board are:

- When plugging/unplugging the carrier from the holder always ground all pins at the same potential on the switch board.
- Never switch on/off the equipment connected to the BNCs input/output on the SW board as the spikes will certainly destroy the sample! Always float or ground the μ-electrode connection before plugging or switching equipment.

When doing gap characterization measurements for the μ-electrodes terminal leads, safe values (bellow I_f and V_f) of V, and I had to be used. Is important to consider too the breakdown voltage of the buffer layer. In table 5.3 we show calculation of failure properties for terminal leads. Is important to remember that the voltage drop is along the length of the terminal lead and consequently not the total applied voltage, which is usually higher.

In Fig.5.6 a) we show a schematic diagram with the typical connections needed for DC I-V characterization experiments. A Keithley 2400 source-meter is used to bias the circuit and then measure the current flowing through it. The source-meter

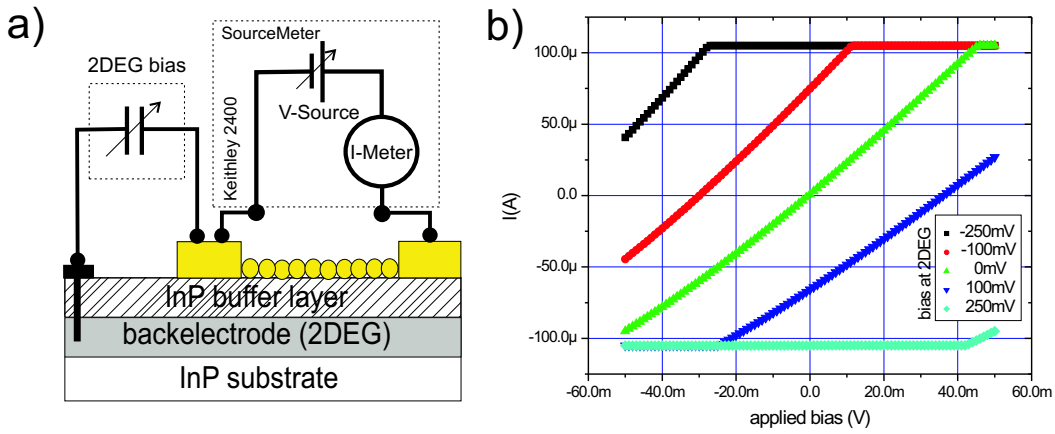

Figure 5.6: (a) Measurement circuit for I-V characterization. (b) Typical I-V curves between contiguous μ-electrodes. Flat regions of the I-V curves are an instrumental saturation effect due to limited current output by the source-meter.

is connected to a GPIB computer data acquisition card. We use a LabView interface designed for controlling the measurements and take data. With it we set the voltage range values, the size of the voltages steps of the ramp, and the rate at which the voltages are set and the current is measured. With this program we are able to plot I-V curves in real time. For biasing the backelectrode an independent power supply is used.

In Fig.5.6 b) we show typical obtained I-V data for two contiguous μ-electrodes without a device, the I-V curve may be linear or slightly non-linear. Typical resistance values for close μ-electrodes is a few hundred ohms with no bias at the backelectrode. The resistance between a μ-electrode and backelectrode is in most cases about 1 to 2 $K\Omega$. This low resistance reflects that the InP buffer layers autodope, most likely with Si, during fabrication due to contamination in the fabrication chamber. These measurements are always performed for the characterization of the 'gap' just before the fabrication of any device.

5.2.3 Device fabrication & characterization

The techniques for fabricating connected wires were described in section 4.5. Now, how to bridge the terminal leads and form a working device? We first deposited a dotted line on the region of interest, in this case between μ-electrodes 12 & 1. The dots were deposited with the tip following a trajectory from the top of μ-electrode 12 to the substrate and close to μ-electrode 1, the deposition was stopped just before reaching it ($< 10\ nm$ gap). Usually, depositing from the substrate to the μ-electrode yielded unreliable results with frequent destruction of the terminal. This first step is shown in Fig. 5.7 a). The line is formed by 18 dots and expands the approximated distance to bridge the u-electrodes $l = 420\ nm$. The deposition parameters are: $\Delta V = \oplus 35\ V$, $\Delta t = 1\ ms$, and the tip-sample distance is fixed at 6 nm. The dots are about 4 nm tall and 17 nm wide. We call this first deposited line NW1,and is shown in Fig. 5.7 a). Parallel to this dotted line a second one, NW2, is fabricated by overlapping two depositions with $\Delta V = \oplus 39\ V$, this wire can be appreciated in Fig. 5.7 b). The line is shorter and is not connected to μ-electrode 1 (a gap of about 15 nm). An I-V curve is taken at this moment and is shown in Fig. 5.7 c). As revealed by the graph, the I-V curve is strictly linear after the dotted lines depositions were performed.

Now for bridging the gap with a continuous (connected) line a sequence of three overlapping depositions was performed on NW1 with $\Delta V = \oplus 39\ V$, $\Delta V = \oplus 41\ V$, $\Delta V = \oplus 43\ V$, and keeping all other parameters fixed. The depositions were always performed by moving the tip from μ-electrode 12 to 1 (and trying to avoid μ-electrode 1). At this stage NW1 appears connected as can be appreciated from Fig. 5.7 b) and the dimensions have changed now to a width of 27 nm and a height that ranges from 8 nm to about 4 nm. The highest section is close to μ-electrode 12, and the lowest is in the proximity to μ-electrode 1. In addition, the nanowire seems to have a good contact to μ-electrode 12 and there is at least one dot from the last deposition, connected to the side of NW1 which overlap with μ-electrode 1, as measured by line profiles.

As a matter of fact, after the last deposition on NW1 the I-V curve changed to the one shown in Fig. 5.7 d) and it is slightly non-linear. We can calculate the resistance of the nanowire at this stage by modeling it as a parallel resistors circuit whose elements are the resistance of the device R_{NW1}, the resistance of the gap R_{gap} before deposition, and the combined value R_{eq}:

$$\frac{1}{R_{eq}} = \frac{1}{R_{gap}} + \frac{1}{R_{NW1}}, \tag{5.5}$$

with $R_{gap} = 554\ \Omega$, and $R_{eq} = 460\ \Omega$, solving for R_{NW1}, the resistance of the nanowire is about (2700±30) Ω. The same measurement was performed by biasing the backelectrode at 250 mV. In this case the resistance between the electrodes before bridging is $R_{gap} = 836\ \Omega$ and after is 630 Ω which gives a resistance for the nanowire of about $(2500 \pm 12)\ \Omega$.

An estimation for the resistivity of the nanowire can be calculated by using equation 5.1 and solving for the resistivity:

$$\rho_{NW1} = R_{NW1} \times \frac{A}{l}. \tag{5.6}$$

The cross section of the wire is not uniform through its length but the height can be approximated to 5 nm so the cross section is $A \approx 5 \times 27\ nm^2$. With $l = 420\ nm$, and $R_{NW1} = 2500\ \Omega$, the value of the resistivity for the fabricated nanowire is $\rho_{NW1} \approx (803 \pm 30)\ \Omega\text{-}nm$ or $\rho_{NW1} \approx 37 \times \rho_0$, which is an intermediate value to those reported by Calleja's, *et al.* as mentioned earlier. They report too that the I-V for their longer nanowire has a slight non-linear behavior on the negative part of the curve [47]. As we discussed in the introduction, such a high resistivity is not expected especially if positive polarity is used. We measured current densities for NW1 j_{NW1} up to 0.74 $\mu A/nm^2$.

In the case of NW1 the contact to μ-electrode 1 is expected to be highly resistive with only one conduction channel, and most likely formed by a SGB with a high reflection coefficient. This may explain the high total resistance of the wire and the non linear I-V showing a tunnel behavior.

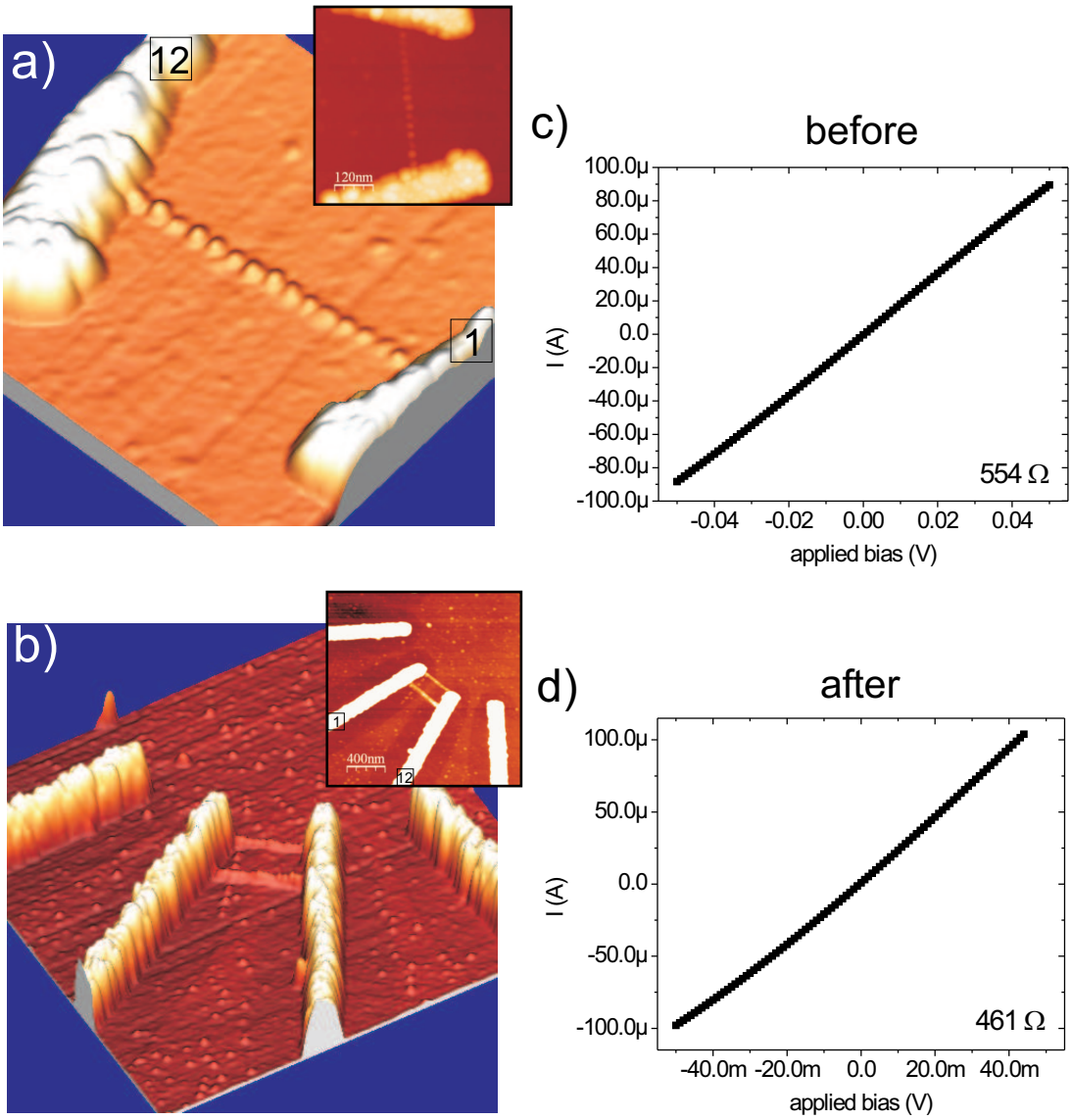

Figure 5.7: Bridging μ-electrodes 12 & 1, and I-V characterization. (a), (b) 3D representation of AFM scans. The insets are the corresponding surface images (a) A dotted line is deposited from μ-electrode 12. (b) After several depositions the line appears to be continuous and bridging the gap. A second not connected line is deposited at the terminals end. (c), (d) I-V curves before and after the nanowire bridge the μ-electrodes. The 20nm InP/10nm InGaAs /InP sample is used.

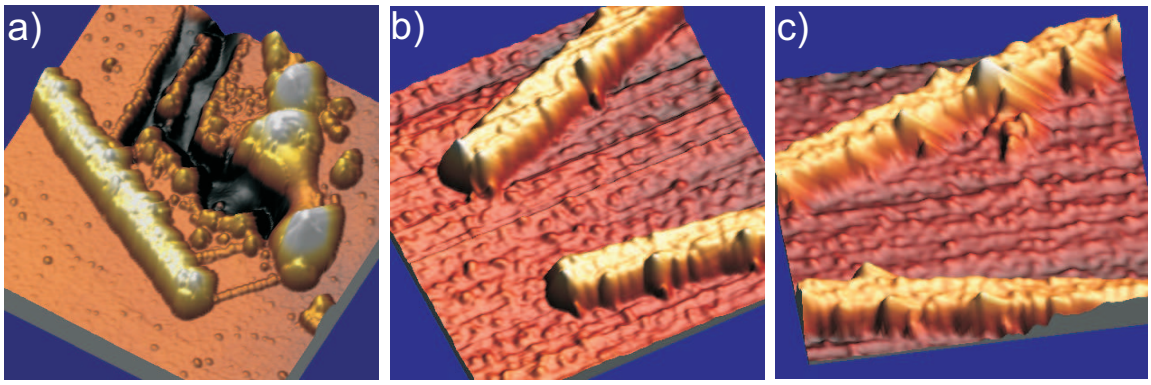

Figure 5.8: 3D rendering of AFM scans of tip & μ-electrodes interactions. (a) Destruction of μ-electrode 1 by accidental contact with the pulsed tip. (b), (c) Moving the tip with positive polarity on the proximity of the edges of two μ-electrodes. (b) Before (no bias has been applied to the tip), (c) After, mass movement along the edge of the μ-electrodes.

An attempt to improve the contact between NW1 and μ-electrode 1 by performing an overlapping deposition from the electrode to the nanowire resulted in the destruction of the device. This is shown Fig. 5.8 a), it seems that we must have touched the μ-electrode with the pulsed tip: it destroyed the electrode and NW1, the InP layer appears severely damaged with grooves of 20 nm deep. As we will see in the next sections this is a very common problem.

5.2.4 Overcoming edge problems

In most of our FED deposition experiments the tip is positive polarized for avoiding possible oxidation of the surface. As it turn out, this choice introduces new challenges in terms of possible structural damages made on the μ-electrodes. The problem arises in the fact that in the FED process the direction of the mass transfer will always be favored for negative ions (lower deposition threshold), and since the μ-electrodes have many sharp cusps, especially at the edges, which can have smaller or similar to the dimensions of the tip apex, a reversed process can be initiated: transfer will happen from the μ-electrode to the tip given that the electric field intensity is a least half to the one on the tip[6]. In Fig. 5.8 b), and c) we show such an event by applying

[6]As mention in section 2.2.2 the threshold field is 23.8 V/nm, 12.5 V/nm, and 11.3 V/nm for Au^{+}, Au^{-}, and Au^{2-}, respectively. Notice that the average field V/d is constant.

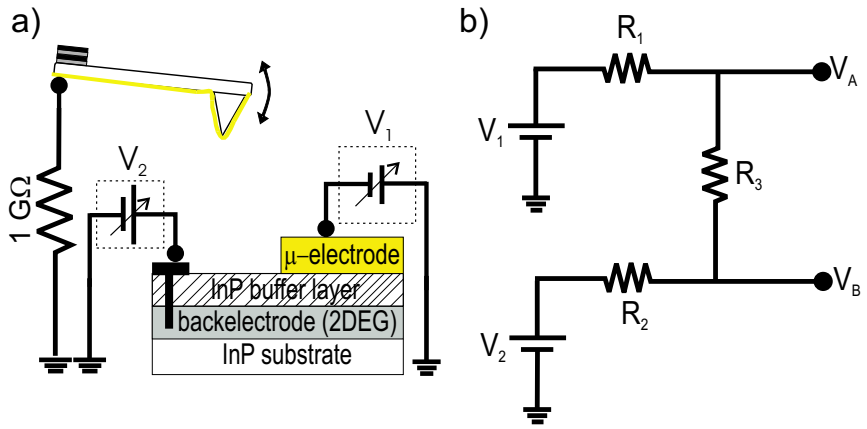

Figure 5.9: (a) Schematic diagram of the setup for the differential contrast enhancement technique. (b) Corresponding equivalent circuit diagram. R_1 and R_2 are the contact resistance at the μ-electrode and 2DEG, respectively. R_3 is the resistance of the buffer layer.

a positive bias to the tip and scanning on the μ-electrodes. Mass movement along the edges is quite notorious. This occurrence is actually quite common in these μ-electrodes as it will be studied with some more detail in the next section. By using negative polarity this situation may be avoided. Nevertheless, problems like the one in Fig. 5.8 a) still need a solution. No matter what polarity is used the tip interaction is always stronger at the edges.

To overcome edge problems, regardless of the polarity employed, we have developed a differential contrast enhancement technique for compensating electric field differences between the metallic and semiconductor surfaces. In Fig. 5.9 a) we show a schematic of the setup employed for implementing this technique in which two power supplies are used to apply biases V_1 and V_2 to the μ-electrode and the backelectrode, respectively. Since a lift voltage is used to control the tip-sample distance, setting the μ-electrode and the backelectrode at different potentials, makes the tip interact with different force gradients, equation 3.1, on the μ-electrode, proportional to $(V_2 - V_1)^2$, and on the semiconductor, proportional to V_2^2. With the right combination of V_1 & V_2 a μ-electrode can be screened electrostatically by reducing its apparent height. In an EFM scan image the μ-electrode seems to 'disappear' and all the scan area appears flat, with no contrast to the tip.

In Fig. 5.10 we show several section profiles of a μ-electrode in a sample which is subjected to differential bias. The experiment is performed on the 500 nm wide section of a sample with design I, described in the next section, in which the device fabrication region has been completely destroyed by ESD. Increasing V_1, with the backelectrode grounded, will rise the μ-electrode to 30 nm and 43 nm for 7.5 V , and 9.5 V respectively, as can be appreciated in Fig. 5.10 a), and b). If we apply different biases to both electrodes we are able to diminish the apparent height of the μ-electrode to 17 nm with no bias applied on the μ-electrode and $V_2 = 10\ V$, and to 12 nm for $V_1 = 7.5\ V$ and $V_2 = 10\ V$. This is shown in Fig. 5.10 d), and e). The height of the μ-electrode is about 22 nm as shown in Fig. 5.10 c).

In fact, the success of this technique on our samples is only partial due to leaky electrodes (InP buffer layer always conductive). To explain this, we make use of the equivalent circuit diagram show in Fig. 5.9 b). The expressions for the voltage at the μ-electrode V_a and the voltage on the backelectrode V_b are

$$V_a = \frac{(R_2 + R_3)V_1 + R_1 V_2}{R_1 + R_2 + R_3}, \tag{5.7}$$

$$V_b = \frac{R_2 V_1 + (R_1 + R_3)V_2}{R_1 + R_2 + R_3}, \tag{5.8}$$

where R_1 is the contact resistance at the μ-electrode, R_2 is the contact resistance at the backelectrode, and R_3 is the resistance between the μ-electrode and the backelectrode. This last quantity gives an idea on how leaky the μ-electrodes are[7]. Usually R_1, few Ω, and R_2 few tens of Ω are much smaller than R_3, which is typically a few hundred Ω. Then, equations 5.7 and 5.8 can be simplified to

$$V_a = V_1 + \frac{R_1}{R_3} V_2, \tag{5.9}$$

$$V_b = \frac{R_2}{R_3} V_1 + V_2. \tag{5.10}$$

These equations show that for a leaky buffer layer (the 20 nm InP film) it is not possible to control independently the μ-electrode and the backelectrode. The experiment

[7]The gate efficiency capacitance ratio ($\alpha = C_{Gate}/C_{total}$) is a more suitable quantity to describe this.

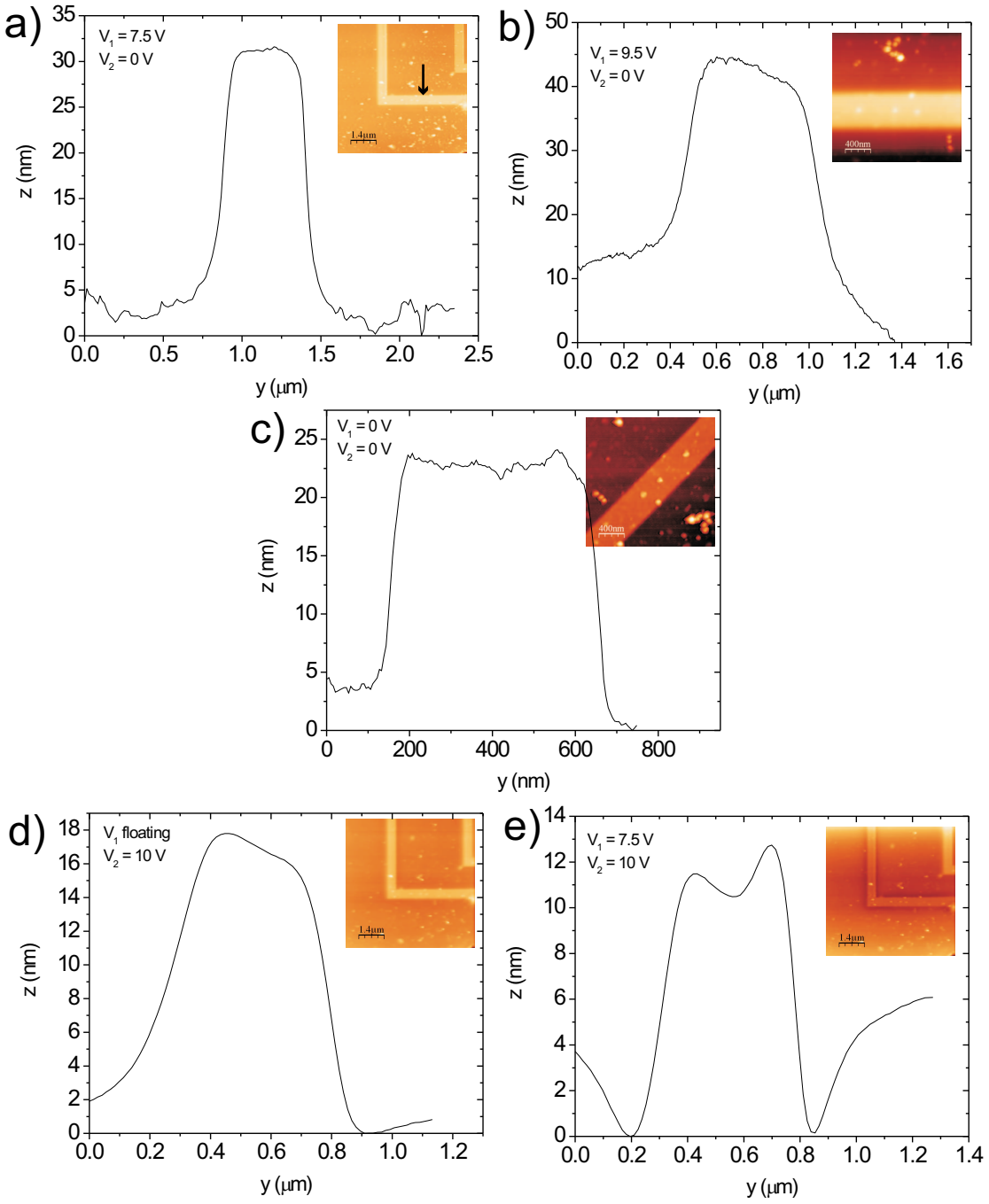

Figure 5.10: Rising and hiding a μ-electrode. (a)-(e) Section profiles while biasing the μ-electrode and the backelectrode. The μ-electrode is raised up to 43 nm at b), and hidden up to 12 nm at e). The topographical scan is shown at c). The arrow in a) shows the location at where all the section profiles were taken. Insets are the corresponding AFM scan.

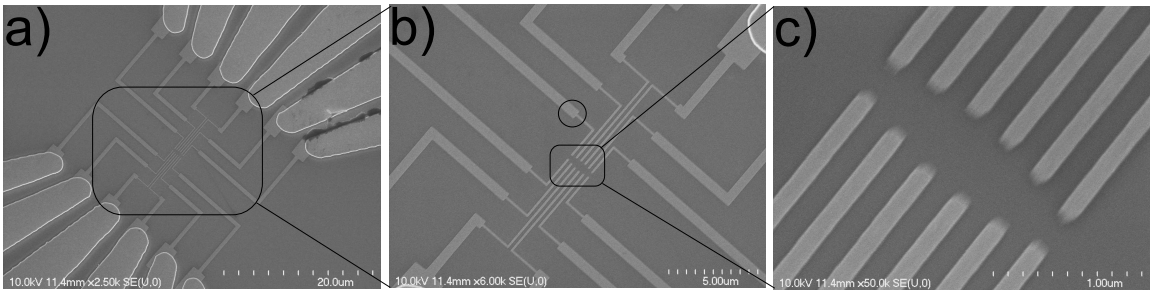

Figure 5.11: FE-SEM scans of μ-electrodes patterns with design I at different magnification scales. (a) Photolithographic and e-beam lithography steps (b) The section at which μ-electrodes width change from 500 nm to 100 nm is marked with a circle. All 12 μ-electrodes have these sections. (c) Device fabrication area. The terminal leads are 100 nm wide. The very end of each μ-electrode has a shallow angle, for facilitating FE deposition. This design allows the possibility of four probe measurements.

in Fig. 5.10 was implemented in a sample with a quite high R_3 (about 5 $k\Omega$), actually the highest of all the samples measured. For typical samples, applying V_1 affects also the immediate area surrounding the μ-electrode limiting the hiding or rising of it. In the worst cases, applying V_1 has the same effect as only biasing the backelectrode. Increasing the thickness of the buffer layer did not help solve this problem. Actually, the problem persisted up to buffers with an InP film thickness of 65 nm. R_3 was only incremented to about 1 $k\Omega$. This is due to Si background contamination while growing the heterostructure. A solution to this is to perform the experiment at low-temperature and thus augmenting the resistance of the buffer layer to tens of $k\Omega$'s.

5.3 Model for the failure mechanism of μ-electrodes leads

As mentioned before μ-electrodes patterns with design I were not as stable as samples with design II. The fabrication method is exactly the same, as is the substrate where they are grown. The geometry of design I is show in Fig. 5.11 a), b), and c). The μ-electrodes terminal ends in Fig. 5.11 c) have a width of 100 nm, which is the distance between contiguous μ-electrodes too. Distance between opposing terminals ranges from 100 nm to 300 nm. Both samples, design I & II, are quite susceptible to electrostatic discharge ESD. Actually, even with the handling precautions mentioned

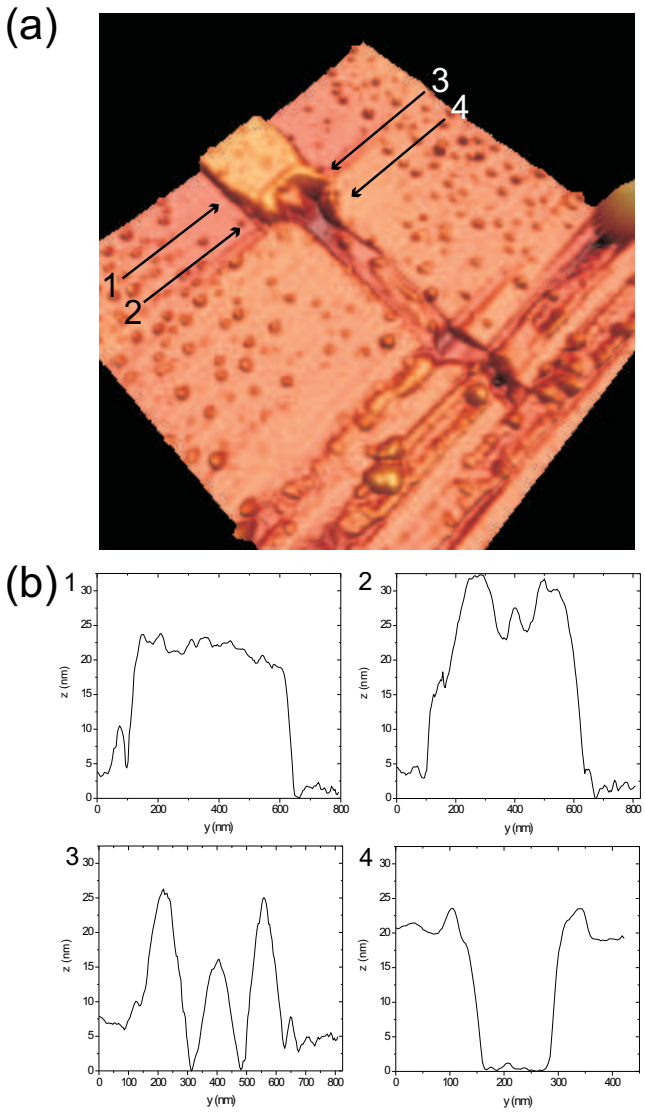

Figure 5.12: (a) AFM image of an ESD blown wire. (b) Section profiles of the contact and μ-electrode interface on (a). 1- Far from the transversal interface the dimensions are as usual. 2- Just before the interface the height has increased considerably. 3- Severe damage of the interface. 4- Catastrophic failure of the μ-electrode, there is a 20nm deep trench.

in section 5.2.1, most of the time design I suffered catastrophic failure in which all the μ-electrodes terminal leads were destroyed leaving behind 20 nm deep trenches, as can be appreciated in Fig. 5.12 a). The resulting geometrical shape of the damage at the interface where the width of the μ-electrode lead shrinks from 500 nm to 100 nm, pointed with arrows in Fig. 5.12 a) and marked with a circle in Fig. 5.11 b), is very regular and had the same characteristics in all cases. The 500 nm wide wire suffers no changes, except at the interface, and it acts as a 'contact' to the smaller 100 nm wide terminal lead which we will often call 'wire', and is the one that usually gets

Table 5.4: Thermal and electrical properties of relevant semiconductors & insulators

Material	κ_{300} $[\frac{W}{mK}]$	Breakdown field $[\frac{V}{nm}]$	Melting point $[K]$
Si	148	0.03	1685
InP	68	0.05	1333
$In_{0.53}Ga_{0.47}As$	6.25	0.005	-
SiO_2	1.38	≈ 1	≈ 1900

destroyed. The choice of names is justified since the cross section area is much bigger, which implies that it can handle larger current densities, and judging from Fig. 5.12 a), it also serves as a heatsink to the smaller 100 nm wire. Nevertheless, in most electrical characterization studies, like the conduction experiments done by Durkan *et al.* previously mentioned, the device is connected to two surface terminals that act as heat sinks at each end. The devices are fabricated on an insulator surface which is typically an oxide like SiO_2 or Al_2O_3 grown on a doped semiconductor substrate (usually n or p doped Si) which is the gate electrode. This is an important difference to our samples since the μ-electrodes and the backelectrode are actually weakly connected through the 20 nm InP buffer layer.

In table 5.4 we show some important differences between some thermal and electrical properties for the materials commonly employed in most studies, and for the ones used for the fabrication of our samples. As matter of fact, it can be seen that the μ-electrodes, in either design, and the nanowire dissipate through the buffer layer. A thicker buffer layer must thus improve heat dissipation, as a thinner oxide will do for wires on Si substrates.

The regularity of the patterns on the damaged interfaces and surfaces prompted us to study the mechanisms by which this wire is destroyed and how the 20 nm deep trenches are formed. The information will be important for understanding how the wires get modified and/or destroyed when a biased SPM tip is in the proximity of the μ-electrode edges. In this section we will model failure mechanisms of a one terminal conductor.

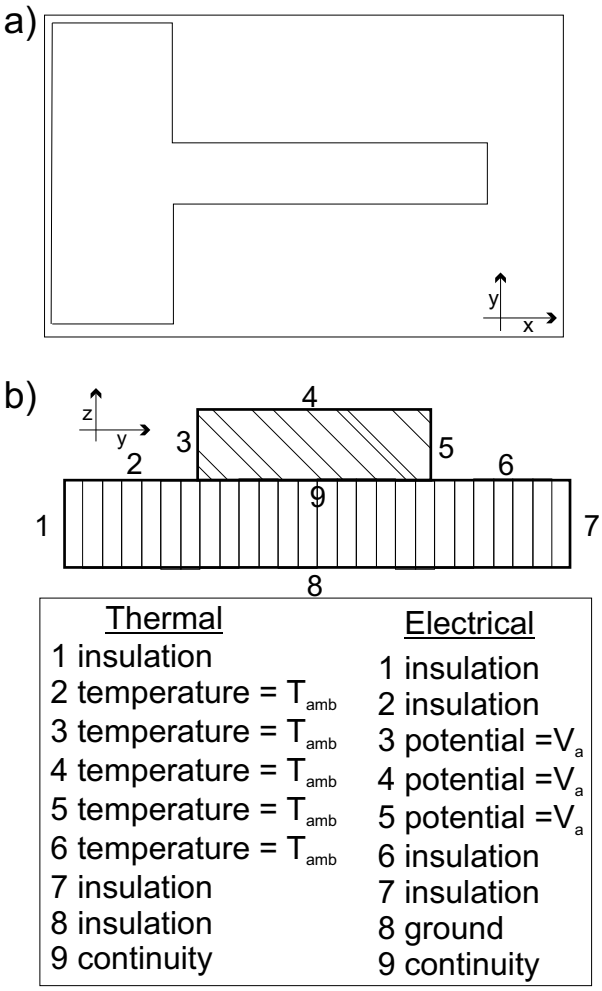

Figure 5.13: Schematic of a one terminal electrode geometry. (a) Top view, (b) Boundary conditions used on the model.

We use FEMLAB[8] to model thermal & electrical properties in a one terminal current carrying wire connected to a one semi-infinite heatsink contact on top of a semiconductor. We define a geometry and impose initial boundary conditions in all possible interfaces. In Fig. 5.13 a), and b), we show a schematic diagram of the geometry and the thermal and electric boundary conditions. We have assumed no convective losses to the surroundings, and have not take into account that properties like the resistivity and the thermal conductivity change with temperature. For the geometry and boundary conditions defined in Fig. 5.13 we solve Poisson's equation for the potential V and the steady state excess temperature T:

[8]Software package that uses finite element. It is developed by COMSOL.

- On the metal,

$$\nabla(\sigma\nabla V) = 0, \tag{5.11}$$

$$\nabla(\kappa_{300}\nabla T) = Q, \tag{5.12}$$

where $Q = j^2\rho$, σ and κ_{300} are the conductivity and the thermal conductivity, respectively.

- On the semiconductor,

$$\nabla[(\sigma + \frac{\epsilon_0\epsilon_r}{t})\nabla V] = 0, \tag{5.13}$$

$$\nabla(\kappa_{300}^{sub}\nabla T) = Q, \tag{5.14}$$

where ϵ_r, κ_{300}^{sub} and t are the permitivity, the thermal conductivity and thickness of the semiconductor, respectively.

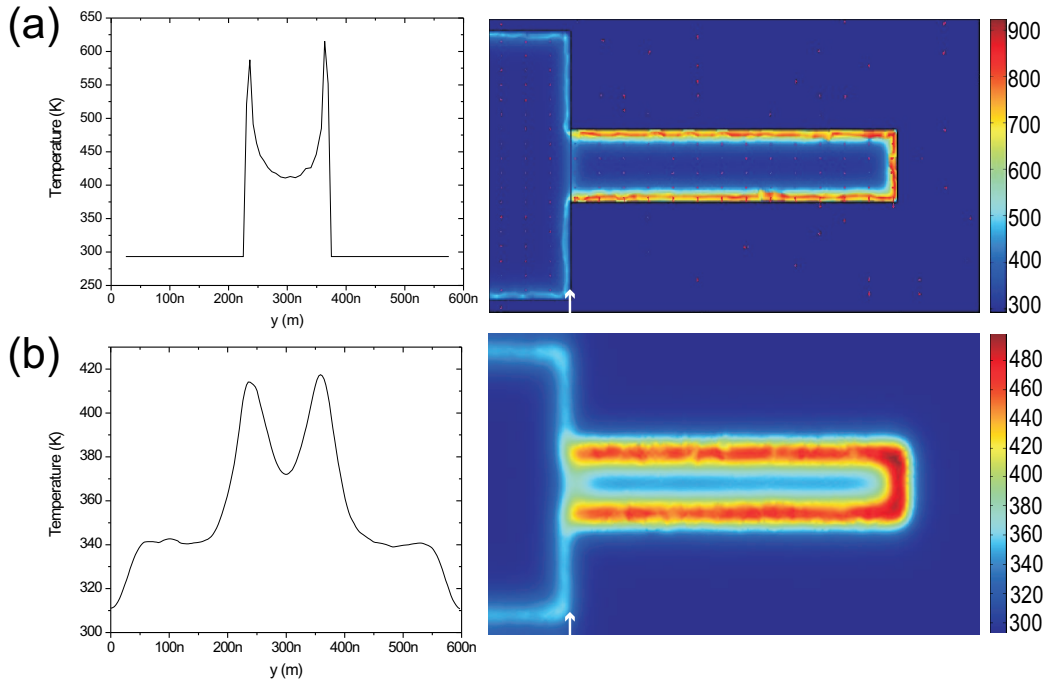

Figure 5.14: Modeled temperature profile and distribution for $V_a = 1\,V$. (a) At the interface between the metallic electrode and the semiconductor. (b) At the interface between the semiconductor and the backelectrode. The color bars at the right of the graph are the temperature in K. The profiles are taken at the interface indicated by the white arrows.

Results of the simulation are shown in Fig. 5.14. As shown in the graph, the temperature is higher at the sides of the wire, and it is remarkable the degree of agreement between the final shape of the contact-wire interface in Fig. 5.12 a) and the temperature distribution in Fig. 5.14 b). Actually, the temperature profiles are nearly inverted to the corresponding topographical ones at the same interface. This suggests that material at the sides of the wire moves more than that in the center. Durkan *et al.* made similar observations, they noticed higher mobility and enlargement of the grains on the borders outside of the nanowires [9]. In Fig. 5.15 we report the

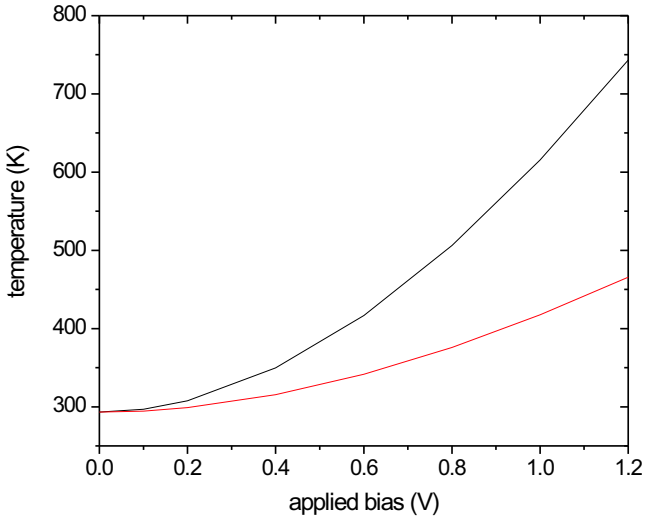

Figure 5.15: Calculated temperature dependence on applied bias at the contact-wire interface. The black line: temperature at the metal and semiconductor interface. Red line: temperature at the interface between semiconductor and the backelectrode. The voltage is applied to the μ-electrode and the backelectrode is grounded.

maximum temperature at the contact-wire interface for different applied voltages at the wire. The curves shape concurs with the one on Fig. 5.3 b) which is reported by Durkan *et al.* [9], [75]. This failure process is consistent with thermal-assisted electromigration in the one terminal wire.

Is not clear what process leads to the establishment of the necessary electric field that so efficiently and routinely destroyed samples and created nanotrenches. Given the similarities between design I and a RFID antenna, we speculate that it acts like an RF antenna. For design II only the geometrical configuration and length of the terminal μ-electrodes was changed, and the resulting design is very stable when

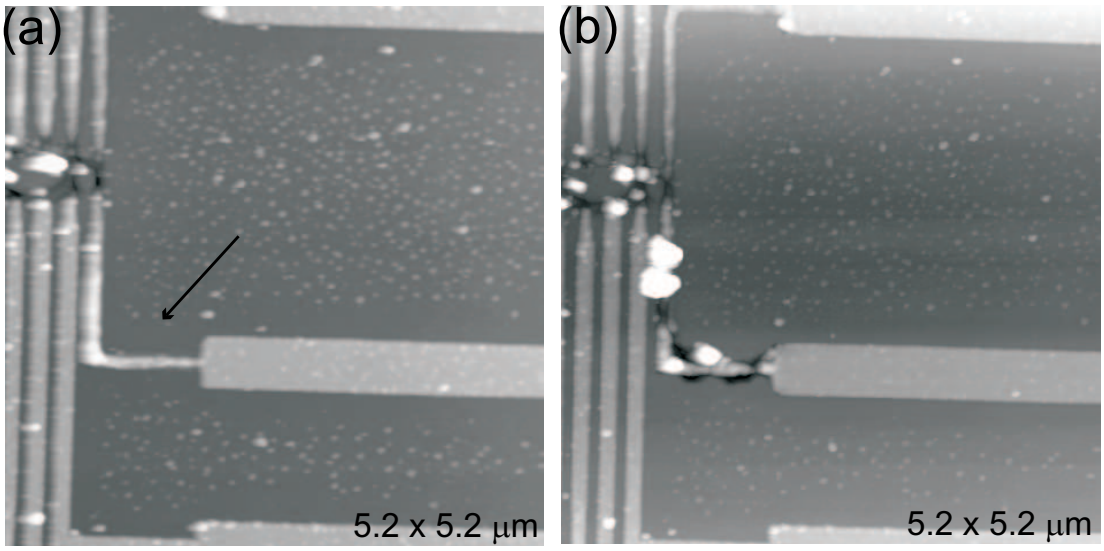

Figure 5.16: AFM images of a controlled destruction of a μ-electrode. (a) Initial scan. The wire already have bee damaged by ESD, is thinner and taller than a regular one. (b) The wire has been considerably thinned and seems broken close to the contacting electrode. The semiconductor surface is very damaged.

properly handled.

To measure under real conditions we deliberately applied a potential difference between the wire and backelectrode to cause a controlled failure. The results are shown in Fig. 5.16 a), and b). The bias was increased in steps of 200 mV from 100 mV to 1.5 V. At that voltage, the FEMLAB model predicts a temperature around 1100 K at the contact-wire on the semiconductor surface, about 200 K below the InP melting point.

6

Conclusions & Outlook

An AFM operated in a non-contact mode proved an effective choice for growing nanoscale sized dots and wires. The technique developed for deposition provide for a robust and precise control of the tip sample-distance by relying on the use of an electrostatical force, which is a monotonic function of the distance, for operating the feedback loop. Dot dimensions, width, height, and aspect ratio are controlled by the amplitude and duration of the applied pulse. The size of the dot seems to be regulated by the magnitude of the applied pulse, while the pulse duration seems to affect mostly the height of the dot. By decoupling the pulse duration from the feedback loop we observe an important improvement on the aspect ratio from about 10% to 40%. In terms of reproducibility, associated with the standard deviations of the dot sizes, our lowest is 8% of the mean which is an improvement when compared to the lowest reported value of 10% [66].

We have established clear evidence that the deposition mechanism is Field Evaporation (FED). We have found that there is a threshold for deposition which is distinctive to the tip polarity, as predicted by the theoretical analysis. We obtain high deposition rates, of the same order of magnitude of calculated values, but increased deposition times show falling rates which is evidence of the presence of a saturation mechanism in the field evaporation process.

Electrostatically our tip-sample configuration geometry agrees to simple modeling. The best approach to our system is given by the sphere-plane geometry. A macroscopic radius R_{mac} is considered when calculating the strength of the capacitive coupling when characterizing the tip lift height with the amount of applied

bias. When tip and sample are at closer distances and for calculating the value of the electric field at the tip apex, a protrusion with microscopic radius R_{mic} is then appropriate.

By using different lithographic modes we have been able to fabricate nanowires with two types of morphologies. We expect different electronic transport properties & failure mechanisms for them. A bamboo-like nanowire was fabricated between two electrode terminals, and an I-V characterization measurement was performed. The electrical resistivity of the nanowire is 803 $\Omega\ nm$, a value 37 times higher than that of the bulk value for gold at ambient conditions. The value is, nonetheless, similar to those obtained in the literature for similar gold sized nanowires.

This deposition technique can be implemented for 'grain engineering' to fabricate wires with a very specific grain structure to allow the study of single grain boundaries with simple configurations. The changes in electrical resistivity can be studied *in situ* while the structure is being fabricated.

With the idea of hiding the electrode edges from the tip while in non-contact operation, we developed a differential contrast enhancement technique that allows for electrostatically screening raised electrodes on a surface. In order to be effective the electrodes need to be deposited on an insulating buffer layer. We are able to apparently rise and partially hide the leads but the results are limited since the InP buffer layers on our substrates are slightly conductive.

Unequivocally, raised electrodes leads pose a challenge to this deposition technique. One of the difficulties is that deposition settings are different when the tip is over a conductive surface that when is at an insulating one. More importantly are the electrode edge effects and roughness of the surface and sidewalls. The electric field is more intense along the edges, and high roughness at the surface & sidewalls translate to cusps and small grains. The interaction with a sharp tip is strong enough to produce mass transfer along the terminal. Under these conditions, there is the possibility too of reversed FED since our tip is positive polarized and the threshold is lower for the negative polarity field emission. Failure by breaking or blowing up is common.

Actually, only small potential drops are needed along these electrodes leads in order to cause failure. Even the presence of a biased tip can cause important modifications at the edges. Nevertheless, this can be used to our advantage for helping bridging the terminal leads and forming or repairing the contacts from the terminals to the device instead of trying to FED deposit from the wire to the device and vice versa[1]. Field emission (FE)-induced fabrication has already been demonstrated by Park *et al.* [93]. In their experiments an NC-AFM in which the tip is been coated with W_2C is used to grow gold nanostructures on a gold thin film substrate. This can be implemented with our setup by following these steps:

- FED deposit a nanowire in a region contiguous to two (or more) terminal leads ensuring that there is a separation of about 10 nm between them and the leads. We are then able to reliably deposit nanowires by keeping this clearance.
- Change the tip used on the FED deposition to one with a strong conductive coating (like W_2C).
- Locate the nanowire on the device fabrication area and perform FE induced modifications on the edge of the electrodes leads and bridge the 10 nm void at each end of the nanowire.

We predict that fabricating devices in this fashion will lead to much more reproducible results.

Another recommendation for future implementations and perhaps the best solution is to use buried electrodes. It seems a very operative way to attack this problem and it has been successfully used as a testbed for measuring single molecules electrical properties [94], [10]. This will definitely eliminate the difficulties that appear when using raised electrode leads.

Most of the mass transfer on a one terminal electrode lead happens on the sidewalls and close to the interface of the terminal as shown by our simulations. The diminished

[1]this procedure will have difficulty succeeding if a gold coated tip is employed owed to reversed FED as mentioned earlier.

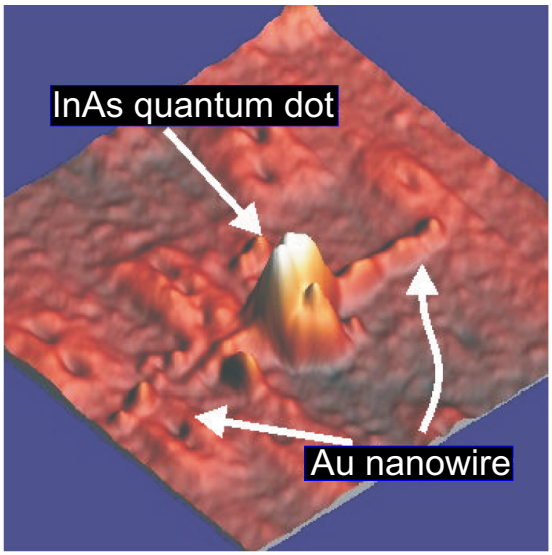

Figure 6.1: Deposition of a nanowire over a InAs quantum dot.

lateral size of the wire only speeds the process that ultimately cause a failure of the lead. An important observation is that sidewalls need to be considered as their size is comparable to the surface of the wire and their roughness may contribute importantly to the electric conduction properties.

Finally, the intended use of this technique in future applications is to fabricate nanoleads to characterize interesting nanostructures. An operative procedure for doing this is:

- Imaging: Topography, localization of nanostructures,
- Fabrication of nanoleads in the vicinity of a nanostructure to a micro-lead, and
- Electrical characterization of fabricated structured + device.

A great advantage of this setup is the capability of simultaneous fabrication and electrical characterization. As a first step in this direction we show in Fig.6.1 a InAs quantum dot over which we have deposited a nanowire.

Bibliography

[1] T.A. Fulton and G.J. Dolan. Observation of single-electron charging effects in small tunneling junctions. *Phys. Rev. Lett.*, 59:109, 1987.

[2] M.A. Reed, J.N. Randall, R.J. Aggarwal, R.J. Matyi, T.M. Moore, and A.E. Wetsel. Observation of discrete electronic states in a zero-dimensional semiconductor nanostructure. *Phys. Rev. Lett.*, 60:535, 1988.

[3] Sander J. Tans, Michel H. Devoret, Hongjie Dai, Andreas Thess, Richard E. Smalle, L.J. Geerligs, and Cees Dekker. Individual single-wall carbon nanotubes as quantum wires. *Nature*, 386:474, 1997.

[4] Hongkun Park, Jiwoong Park, Andrew K.L. Lim, Erik H. Anderson, A. Paul Alivisatos, and Paul L. McEuen. Nanomechanical oscillations in a single-C_{60} transistor. *Nature*, 407:57, 2000.

[5] M.A. Reed, C. Zhou, C.J. Muller, T.P. Burgin, and J.M. Tour. Conductance of a molecular junction. *Science*, 278:252, 1997.

[6] D.L. Klein, P.L. McEuen, J.E. Bowen-Katari, and A.P. Alivisatos. An approach to electrical studies of single nanocrystals. *Appl. Phys. Lett.*, 68:2574, 1996.

[7] K. Liu, Ph. Avouris, J. Bucchignano, R. Martel, S. Sun, and J. Michl. Simple fabrication scheme for sub-10 nm electrode gaps using eletron-beam lithography. *Appl. Phys. Lett.*, 80:865, 2002.

[8] A.F. Morpurgo, C.M. Marcus, and D.B. Robinson. Controlled fabrication of metallic electrodes with atomic separation. *Appl. Phys. Lett.*, 74:2084, 1999.

[9] C. Durkan, M.A. Schneider, and M.E. Welland. Analysis of failure mechanisms in electrically stressed au nanowires. *J. Appl. Phys.*, 86:1280, 1999.

[10] H. Park, A.K.L. Lim, A.P. Alivisatos, J. Park, and P.L. McEuen. Fabrication of metallic electrodes with nanometer separation by electromigration. *Appl. Phys. Lett.*, 75:301, 1999.

[11] M.F. Lambert, M.F. Goffman, J.P. Bourgoin, and P. Hesto. Fabrication and characterization of sub-3 nm gaps for single-cluster and single-molecule experiments. *Nanotechnology*, 14:772, 2003.

[12] C. Schönenberger, H. van Houten, H.C. Donkersloot, A.M.T. van der Putten, and L.G.J. Fokkink. Single-electron tunneling up to room temperature. *Physica Scripta*, T45:289, 1992.

[13] C. Joachim, J.K. Gimzewski, and A. Aviram. Electronics using hybrid-molecular and mono-molecular devices. *Nature*, 408:541, 2000.

[14] Ronald P. Andres, Jeffery D. Bielefeld, Jason I. Henderson, David B. Janes, Venkat R. Kolagunta, Clifford P. Kubiak, William J. Mahoney, and Richard G. Osifchin. Self-assembly of a two-dimensional superlattice of molecularly linked metal clusters. *Science*, 273:1690, 1996.

[15] Z.C. Dong, T.Yakabe, D. Fujita, T. Ohgi, D. Rogers, and H. Nejoh. Metal Atomic Chains on the Si(100) Surface. *Jpn. J. Appl. Phys. Part 1*, 37:807, 1998.

[16] C.J. Kiely, J. Fink, M. Brust, D. Bethell, and D.J. Schiffrin. Spontaneous ordering of bimodal ensembles of nanoscopic gold clusters. *Nature*, 396:444, 1998.

[17] Mei Li, Heimo Schnablegger, and Stephen Mann. Coupled synthesis and self-assembly of nanoparticles to give structures with controlled organization. *Nature*, 402:393, 1999.

[18] Tue Hassenkam, Kasper Moth-Poulsen, Nicolai Stuhr-Hansen, Kasper Nørgaard, M.S. Kabir, and Thomas Bjørnholm. Self-assembly and conductive properties of molecularly linked gold nanowires. *Nano Lett.*, 4:19, 2004.

[19] J. Lefebvre, P.J. Poole, J. Fraser, G.C. Aers, D. Chithrani, and R.L. Williams. Self-assembled InAs quantum dots on InP nano-templates. *J. Crys. Growth*, 234:391, 2001.

[20] P.J. Poole, J. McCaffrey, R.L. Williams, J. Lefebvre, and D. Chithrani. Chemical beam epitaxy growth of self-assembled InAs/InP quantum dots. *J. Vac. Sci. Technol. B*, 19:1467, 2001.

[21] R. Stomp, Y. Miyahara, S. Schaer, Q. Sun H. Guo, P. Grütter, S. Studenikin, P. Poole, and A. Sachrajda. Detection of Single-Electron Charging in an Individual InAs Quantum Dot by Noncontact Atomic-Force Microscopy. *Phys. Rev. Lett.*, 94:056802, 2005.

[22] G.Burkard, D. Loss, and D.P. DiVincenzo. Coupled quantum dots as quantum gates. *Phys. Rev. B*, 59:2070, 1999.

[23] G. Binning, H. Rohrer, C. Gerber, and E. Weibel. Surface studies by scanning tunneling microscopy. *Phys. Rev. Lett.*, 49:57, 1982.

[24] G. Binning, C.F. Quate, and C. Gerber. Atomic force microscopy. *Phys. Rev. Lett.*, 56:930, 1986.

[25] U. Staufer, R. Wiesendanger, L.M. Eng, L. Rosenthaler, H.R. Hidber, H.J. Güntherodt, and N. García. Surface modification in the nanometer range by the scanning tunneling microscope. *J. Vac. Sci. Technol. A*, 6:537, 1988.

[26] S.C. Minne, G. Yaralioglu, S.R. Manalis, J.D. Adams, J. Zesch, A. Atalar, and C.F. Quate. Automated parallel high-speed atomic force microscopy. *Appl. Phys. Lett.*, 72:2340, 1998.

[27] Information for this graph gathered in a conference by Colm Durkan.

[28] H.C. Day, D.R. Allee, R. George, and V.A. Burrows. Nanometer scale patterning of a monolayer Langmuir- Blodgett film with a scanning tunneling microscope in air. *Appl. Phys. Lett.*, 62:1629, 1993.

[29] J.A. Dagata, J. Schneir, H.H. Harary, C.J. Evans, M.T. Postek, and J. Bennett. Modification of hydrogen-passivated silicon by a scanning tunneling microscope operating in air. *Appl. Phys. Lett.*, 56:2001, 1990.

[30] H.J. Mamin, P.H. Guethner, and D. Rugar. Atomic Emision from a Gold Scanning-Tunneling-Microspe Tip. *Phys. Rev. Lett.*, 65:2418, 1990.

[31] Ricardo García, Montserrat Calleja, and Francesc Pérez-Murano. Local oxidation of silicon surfaces by dynamic force microscopy: Nanofabrication and water bridge formation. *Appl. Phys. Lett.*, 72:2295, 1998.

[32] Marta Tello and Ricardo García. Nano-oxidation of silicon surfaces: Comparison of noncontact and contact atomic-force microscopy methods. *Appl. Phys. Lett.*, 79:424, 2001.

[33] Tien T. Tsong. Effects of an electric field in atomic manipulations. *Phys. Rev. B*, 44:13703, 1991.

[34] N. M. Miskovsky and Tien T. Tsong. Field evaporation of gold in single- and double-electrode systems. *Phys. Rev. B*, 46:2640, 1992.

[35] J.I. Pascual, J. Méndez, J. Gómez-Herrero, A.M. Baró, N. García, and Vu Thien Binh. Quantum Contact in Gold Nanostructures by Scanning Tunneling Microscopy. *Phys. Rev. Lett.*, 71:1852, 1993.

[36] Daisuke Fujita, Qidu Jiang, and Hitoshi Nejoh. Fabrication of gold nanostructures on a vecinal Si(111) 7x7 surface using ultrahigh vacuum tunneling microscope and a gold-coated tungsten tip. *J. Vac. Sci. Technol. B*, 14:3413, 1996.

[37] T.C. Chang, C.S. Chang, H.N. Lin, and Tien T. Tsong. Creation of nanostructures on gold surfaces in nonconducting liquid. *Appl. Phys. Lett.*, 67:903, 1995.

[38] E.S. Snow and P.M. Campbell. AFM Fabrication of Sub-10-Nanometer Metal-Oxide Devices with in Situ Control of Electrical Properties. *Science*, 270:5242, 1995.

[39] K. Matsumoto, M. Ishii, K. Segawa, Y. Oka, B.J. Vartanian, and J.S. Harris. Room temperature operation of a single electron transistor made by the scanning tunneling microscope nanooxidation process for the TiOx/Ti system. *Appl. Phys. Lett.*, 68:34, 1996.

[40] Sumio Hosaka, Hajime Koyanagi, and Atsushi Kikukawa. Nanometer Recording on Graphite and Si Substrate Using an Atomic Force Microscope in Air. *Jpn. J. Appl. Phys.*, 32:**L**464, 1993.

[41] Sumio Hosaka and Hajime Koyanagi. Field evaporation of metal atoms onto insulator/conducting substrate using atomic force microscope. *Jpn. J. Appl. Phys.*, 33:**L**1358, 1994.

[42] E.S. Snow and P.M. Campbell. Fabrication of Si nanostructures with an atomic force microscope. *Appl. Phys. Lett.*, 64:1932, 1994.

[43] Dawen Wang, Liming Tsau, and K. L. Wang. Nanometer-structure writing on Si(100) surfaces using a non-contact-mode atomic force microscope. *Appl. Phys. Lett.*, 65:1415, 1994.

[44] John A. Dagata. Device fabrication by scanned probe oxidation. *Science*, 270:1625, 1995.

[45] J.A. Dagata, T. Inoue, J. Itoh, K. Matsumoto, and H. Yokoyama. Role of space charge in scanned probe oxidation. *J. Appl. Phys.*, 84:6891, 1998.

[46] U. Ramsperger, T. Uchihashi, and H. Nejoh. Fabrication and lateral electronic transport measurements of gold nanowires. *Appl. Phys. Lett.*, 78:85, 2001.

[47] M. Calleja, M. Tello, J. Anguita, F. García, and R. García. Fabrication of gold nanowires on insulating substrates by field-induced mass transport. *Appl. Phys. Lett.*, 79:2471, 2001.

[48] Ricardo García and Rubén Pérez. Dynamic atomic force microscopy methods. *Surface Science Reports*, 47:1997, 2002.

[49] Franz J. Giessibl. Advances in atomic force microscopy. *Rev. Mod. Phys.*, 75:949, 2003.

[50] Ernst Meyer, Hans Josef Hug, and Roland Bennewitz. *Scanning Probe Microscopy, The Lab on a Tip*. Springer-Verlag, Berlin Heidelberg New York, 2003.

[51] S. Morita, R. Wiesendanger, and E. Meyer (Eds.). *Noncontact Atomic Force Microscopy*. Springer-Verlag, Berlin Heidelberg New York, 2002.

[52] C.J. Chen. *Introduction to Scanning Tunneling Microscopy*. Oxford University Press, New York, 1993.

[53] C.A. Putman, K.O. van der Werlf, B.G. de Grooth, N.F. van Hulst, J. Greve, and P.K. Hansma. A new imaging mode in atomic force microscopy based on the error signal. *Proc. Soc. Photo-Opt. Instrum. Eng.*, 1639:198, 1992.

[54] A.P. French. *Vibrations and Waves*. W.W. Norton & Co., New York, 1971.

[55] Raphaëlle Dianoux. *Injection et détection de charges dans des nanostructures semiconductrices par Microscopie à Force Atomique*. PhD thesis, Université Joseph Fourier - Grenoble 1, 2004.

[56] J.P. Aimé, R. Boisgard, L. Nony, and G. Couturier. Nonlinear Dynamic Behavior of an Oscillating Tip-Microlever System and Contrast at the Atomic Scale. *Phys. Rev. Lett.*, 82:3388, 1999.

[57] L. Nony, R. Boisgard, and J.P. Aimé. Nonlinear dynamical properties of an oscillating tip-cantilever system in the tapping mode. *J. Chem. Phys.*, 111:1615, 1999.

[58] In-Whan Lyo and Phaedon Avouris. Field-Induced Nanometer- to Atomic-Scale Manipulation of Silicon Surfaces with the STM. *Science*, 253:173, 1991.

[59] Joseph A. Stroscio and D. M. Eigler. Atomic and molecular manipulation with the scanning tunneling microscope. *Science*, 254:1319, 1991.

[60] T.T. Tsong. *Atom-Probe Field Ion Microscopy.* Cambridge University Press, Cambridge, 1990.

[61] H.J. Mamin and D. Rugar. Comment on 'Quantum Contact in Gold Nanostructures by Scanning Tunneling Microscopy'. *Phys. Rev. Lett.*, 72:1128, 1994.

[62] C.S. Chang, W.B. Su, and Tien T. Tsong. Field Evaporation between a Gold Tip and a Gold Surface in the Scanning Tunneling Microscope Configuration. *Phys. Rev. Lett.*, 72:574, 1994.

[63] Hajime Koyanagi, Sumio Hosaka, Ryo Imura, and Masataka Shirai. Field evaporation of gold atoms onto a silicon dioxide film by using an atomic force microscope. *Appl. Phys. Lett.*, 67:2609, 1995.

[64] C.X. Guo and D. J. Thomson. Material transfer between metallic tips and surface in the STM. *Ultramicroscopy*, 42-44:1452, 1992.

[65] D.H. Huang, T. Nakayama, and M. Aono. Platinum nanodot formation by atomic point contact with a scanning tunneling platinum tip. *Appl. Phys. Lett.*, 73:3360, 1998.

[66] A. Houel, D. Tonneau, N. Bonnail, H. Dallaporta, and V. I. Safarov. Direct patterning of nanostructures by field-induced deposition from a scanning tunneling microscope tip. *J. Vac. Sci. Technol. B*, 20:2337, 2002.

[67] D. Fujita and T. Kumakura. Reproducible fabrication of metallic silver nanostructures on a Si(111)-(7x7) surface by tip-material transfer of a scanning tunneling microscope. *Appl. Phys. Lett.*, 82:2329, 2003.

[68] R. Dianoux, F. Martins, F. Marchi, C. Alandi, F. Comin, and J. Chevrier. Detection of electrostatic forces with an atomic force microscope: Analytical and experimental dynamic force curves in the nonlinear regime. *Phys. Rev. B*, 68:045403, 2003.

[69] Emile Durand. *Électrostatique, Vol. II.* Masson et Cie, Paris, 1966.

[70] S. Hudlet, M. Saint Jean, C. Guthmann, and J. Berger. Evaluation of the capacitive force between an atomic force microscopy tip and a metallic surface. *Eur. Phys. J. B*, 2:5, 1998.

[71] L. Olsson, N. Lin, V. Yakimov, and R. Erlandsson. A method for *in situ* characterization of tip shape in ac-mode atomic force microscopy using electrostatic interaction. *J. Appl. Phys.*, 84:4060, 1998.

[72] H.W. Hao, A.M. Baró, and J.J. Sáenz. Electrostatic and contact forces in force microscopy. *J. Vac. Sci. Technol. B*, 9:1323, 1991.

[73] Ricardo García, Montserrat Calleja, and Heinrich Rohrer. Patterning of silicon surfaces with noncontact atomic force microscopy: Field-induced formation of nanometer-size water bridges. *J. Appl. Phys.*, 86:1898, 1999.

[74] I. Horcas, R. Fernández, J.M. Gómez-Rodríguez, J. Colchero, J. Gómez-Herrero, and A.M. Baró. WSXM: A software for scanning probe microscopy and a tool for nanotechnology. *Rev. Sci. Instrum*, 78:013705, 2007.

[75] C. Durkan and M.E. Welland. Analysis of failure mechanisms in electrically stressed gold nanowires. *Ultramicroscopy*, 82:125, 2000.

[76] G. Mesa, E. Dobado-Fuentes, and J.J. Sáenz. Image charge method for electrostatic calculations in field-emission diodes. *J. Appl. Phys.*, 79:39, 1996.

[77] R. Young, J. Ward, and F. Scire. The Topografiner: An Instrument for Measuring Surface Microtopography. *Rev. Sci. Instrum*, 43:999, 1972.

[78] D. J. Rose. On the magnification and resolution of the field emission electron microscope. *J. Appl. Phys.*, 27:215, 1956.

[79] John E. Sanchez Jr, Oliver Kraft, and Eduard Arzt. Electromigration induced transgranular slit failures in near bamboo Al and Al-2% Cu thin-film interconnects. *Appl. Phys. Lett.*, 61:3121, 1992.

[80] John E. Sanchez Jr, L. T. McKnelly, and J. W. Morris Jr. Slit morphology of electromigration induced open circuit failures in fine line conductors. *J. Appl. Phys.*, 72:3201, 1992.

[81] C. Durkan and M.E. Welland. Size effects in the electrical resistivity of polycrystalline nanowires. *Phys. Rev. B*, 61:14215, 2000.

[82] K. Fuchs. The conductivity of thin metallic films according to the electron theory of metals. *Proc. Cambridge Philos. Soc.*, 34:100, 1938.

[83] E.H. Sondheime. The mean free path of electrons in metals. *Adv. Phys.*, 1:1, 1952.

[84] W.F. Egelhoff Jr, P.J. Chen, C.J. Powell, D. Parks, G. Serpa, R.D. McMichael, D. Martien, and A.E. Berkowitz. Specular electron scattering in metallic thin films. *J. Vac. Sci. Technol. B*, 17:1702, 1999.

[85] Werner Steinhögl, Günther Schindler, Gernot Steinlesberger, and Manfred Engelhardt. Size-dependent resistivity of metallic wires in the mesoscopic range. *Phys. Rev. B*, 66:075414–1, 2002.

[86] A.F. Mayadas and M. Shatzkes. Electrical-resistivity model for polycrystalline films: the case of arbitrary reflection at external surfaces. *Phys. Rev. B*, 1:1382, 1970.

[87] R. Landauer. Spatial variation of currents and fields due to localized scatterers in metallic conduction. *IBM J. Res. Dev.*, 1:223, 1957.

[88] Neil W. Ashcroft and N. David Mermin. *Solid State Physics*. Saunders College, New York, 1976.

[89] J.W.C. de Vries. Resistivity of thin au films as a funtion of grain diameter and temperature. *J. Phys. F: Met. Phys.*, 17:1945, 1987.

[90] Alexander Bietsch, M. Alexander Schneider, M.E. Welland, and Bruno Michel. Electrical testing of gold nanostructures by conducting atomic force microscopy. *J. Vac. Sci. Technol. B*, 18:1160, 2000.

[91] Alexander Bietsch and Bruno Michel. Size and grain-boundary effects of a gold nanowire measured by conducting atomic force microscopy. *Appl. Phys. Lett.*, 80:3346, 2002.

[92] J.R. Black. Electromigration failure modes in aluminum metallization for semiconductors devices. *Proceedings of the IEEE*, 57:1587, 1969.

[93] Kang-Ho Park, Jeongyong Kim nad Jeong Sook Ha, and Ki-Bong Song. Field emission induced fabrication of nanostructures on Au thin films using a noncontact mode atomic force microscope. *J. Vac. Sci. Technol. B*, 21:1357, 2003.

[94] Jiwoong Park. *Electron Transport in Single Molecule Transistors*. PhD thesis, University of California, Berkeley, 2003.